UNIVERSITÉ DE GRENOBLE

THÈSE

Pour obtenir le grade de

DOCTEUR DE L'UNIVERSITÉ DE GRENOBLE

Spécialité : **Matériaux, Mécanique, Génie Civil, Electrochimie**

Arrêté ministériel : 7 août 2006

Présentée par

Guilherme MACHADO

Thèse dirigée par **Denis FAVIER** et
Co-encadrée par **Grégory CHAGNON**

préparée au sein du **Laboratoire Sols, Solides, Structures, Risques 3SR**
dans **l'École Doctorale Ingénierie – Matériaux, Mécanique, Environnement, Energétique, Procédés, Production**

Contribution à l'étude de l'anisotropie induite par l'effet Mullins dans les élastomères silicone chargés

A contribution to the study of induced anisotropy by Mullins effect in silicone rubber

Thèse soutenue publiquement le 12 Mai 2011, devant le jury composé de :

Didier BOUVARD
Professeur, Institut Polytechnique de Grenoble

Frédéric BOYER
Professeur, Ecole des Mines de Nantes

Grégory CHAGNON
Maître de Conférences, Université Joseph Fourier, Grenoble

Denis FAVIER
Professeur, Université Joseph Fourier, Grenoble

Pierre GILORMINI
Directeur de recherche, Arts et Métiers ParisTech

Michel GREDIAC
Professeur, Université Blaise Pascal, Clermont-Ferrand (Rapporteur)

Erwan VERRON
Professeur, Ecole Centrale de Nantes (Rapporteur)

To my dear parents.

Abstract/Résumé

The present work studies the experimental characterization and modeling of the anisotropy induced by Mullins effect, i.e., the loss of stiffness in the first loading cycles, often observed in rubber-like materials. After a description of the mechanical characteristics of the particular silicone material used in our study, experimental tests are developed to create original and complex loading histories. First, successions of conventional uniaxial tensile tests are performed with changing directions of loading. Second, the state of heterogeneous stress and strain obtained in circular membrane swelling tests was completely characterized by means of kinematic field measurements made by the 3D image correlation method, and the loadings are then biaxial tension followed by uniaxial traction. The key parameters for modeling the Mullins effect were able to be identified, including its isotropic and anisotropic parts. A model was thus developed based on the double-network theory taking into account the experimentally motivated criteria. A suitable version with simple implementation in a finite element computer code was finally developed to allow the calculation of a structural part.

Le présent travail étudie la caractérisation expérimentale et la modélisation de l'anisotropie induite par effet Mullins, i.e., la perte de raideur après les premiers cycles de chargement, très souvent observée dans les matériaux de type élastomère. Après une description des caractéristiques mécaniques du matériau silicone utilisé dans notre étude, des essais expérimentaux originaux sont développés pour créer des historiques de chargement complexes. D'une part, des successions d'essais de traction uniaxiale classiques sont réalisées, avec changement de directions de chargement. D'autre part, des états hétérogènes de contrainte et déformation obtenus lors d'essais de gonflement de membrane circulaire ont été complètement caractérisés grâce à des mesures de champs cinématiques réalisées par la méthode de corrélations d'images 3D ; les chargements effectués sont alors de type traction biaxiale-traction simple. Les paramètres clés pour la modélisation de l'effet Mullins ont ainsi pu être mis en évidence, avec notamment ses parts isotrope et anisotrope. Un modèle a ainsi été développé à partir d'une théorie de double réseau prenant en compte des critères expérimentalement motivés. Une version adaptée à une implantation simple dans un code de calculs éléments finis est finalement développée pour la réalisation de calculs de structures.

Acknowledgements

It is a pleasure to thank the many people who made this thesis possible. It is difficult to overstate my gratitude to my Ph.D. supervisors, Denis Favier and Gregory Chagnon. With their enthusiasm, their inspiration, and their great efforts to explain things clearly and simply, they guided me through the academic challenges and supported me in every aspect of my research and professional endeavors. Throughout my thesis-writing period, they provided encouragement, sound advice, good company, and lots of good ideas.

I would like to express my gratitude to the other thesis committee members, Prof. Pierre Gilormini, Prof. Michel Grediac, Prof. Erwan Verron and Prof. Didier Bouvard, for taking the time to read this thesis and for offering many valuable suggestions and criticisms. A special thanks to Prof. Frederic Boyer, head of the project ANR-RAAMO. It is because of the ANR-RAAMO financial support and flexibility that I have been able to work on such interesting and stimulating project, and I greatly appreciate it.

I am indebted to my many laboratory colleagues for providing a stimulating and fun environment in which to learn and grow. There are many others outside the 3SR-Lab community who contributed to my success. I am deeply indebted to Prof. Marcelo Krajnc Alves, who was my advisor in University of Santa Catarina in Brazil during my master degree. He stimulated me to pursue science abroad. I had great experience of working with him and learning professional ways of managing a large research project.

I wish to thank my entire extended family for providing a loving environment for me. Especially my brothers, Netooo and Maria Tereza were particularly supportive. Last but not least, my partner Ana Cecilia made me a happy person and gave me the extra strength, motivation and love necessary to get things done. Finally, I would like to give my special thanks to my parents Teresa Muriano Machado and Lupércio Machado Filho for their unconditional love and for always believing in me. Since I was young, they encouraged me to excel and achieve all the goals that I set for myself.

Contents

List of Symbols and Abbreviations

Except where indicated, latin indices represent the values 1, 2, 3 and, the Greek ones the values 1, 2.

Latin Symbol	Description
$\mathbf{a}$	material direction vector
$\mathbf{b}$	surface curvature tensor
$\mathbf{B}$	left Cauchy-Green strain tensor
$\mathbf{C}$	right Cauchy-Green strain tensor
$\mathbb{C}$	tangent modulus
d	continuum damage parameter
D	Gâteaux derivative
$\mathbf{D}$	rate of deformation tensor
$(\mathbf{e}_1, \mathbf{e}_2, \mathbf{e}_3)$	orthonormal basis in deformed configuration
$\mathbf{e}$	Euler-Almansi strain tensor
$(\mathbf{E}_1, \mathbf{E}_2, \mathbf{E}_3)$	orthonormal basis in reference configuration
$\mathbf{E}$	Green-Lagrange strain tensor
$\mathbb{E}^3$	three-dimensional Euclidean space
$\mathcal{F}$	stress softening evolution function
$\mathbf{F}$	deformation gradient
$\mathbf{g}$	surface metric tensor
$\mathbf{G}_i$ and $\mathbf{g}_i$	covariant basis
$\mathcal{H}$	mean curvature
I_1, I_2, I_3, I_4	strain invariants
$\mathbf{I}$	identity tensor
$\mathbb{I}$	symmetric fourth order tensor
J	volume ratio
$\mathcal{K}$	Gaussian-curvature
p	pressure
p	Lagrange multiplier (Chapter 5)
$\mathbf{P}$	first Piola-Kirchhoff stress tensor

Latin Symbol	Description
$\mathbf{q}$	body force per unit deformed volume
$\mathbf{S}, \mathbf{s}$	surface vector in the reference and deformed configuration
$\mathbb{S}$	supersymmetric fourth order tensor
t	time
$\mathbf{t}$	boundary traction per unit deformed volume
$\mathbf{u}$	displacement field
$\mathcal{U}$	volumetric strain-energy density
$\mathcal{W}$	strain-energy density
$\mathcal{W}_0$	strain-energy density of a virgin material
$\mathcal{W}_{2^{nd}}$	strain-energy density of a second load
$\bar{\mathcal{W}}$	isochoric strain-energy density
$\mathbf{W}$	spin tensor
X^i and x^i	Cartesian coordinates
$\mathbf{X}$,$\mathbf{x}$	position vector in the reference and deformed configuration

Greek Symbol	Description
α	angle between first and second loads
δ	uniaxial directional stress ratio
η	energy loss by Mullins effect according to the loading angle
$\boldsymbol{\varepsilon}$	Piola strain tensor
κ_n	principal curvatures
λ	stretch
μ	strain biaxiality ratio
ψ	strain energy ratio
φ	deformation function
Π	functional
$\boldsymbol{\sigma}$	Cauchy stress tensor
τ	Kirchhoff stress tensor
Θ^α	in-plane curvilinear coordinates

Abbreviation	Description
3D-DIC	three-dimensional digital image correlation
ANR	Agence Nationale de la Recherche
DIC	digital image correlation
FEA	finite element analysis
RAAMO	robot anguille autonome en milieu opaque

Abbreviation	Description
SDIC	stereo digital image correlation
UMAT	Abaqus user material routine

List of Figures

List of Tables

Preface

The eel-like robot motivation

This thesis work, is part of a multidisciplinary research project *Robot Anguille Autonome en Milieu Opaque* (RAAMO ANR) where the purpose is to study, design, build, and control an eel-like robot able to swim in three dimensions. As has been noted in the biorobotics community, eel-like robots are a promising perspective for improving the efficiency and maneuverability of modern-day underwater vehicles (Boyer *et al.*, 2006a, 2008). The interest lies in the anguilliform locomotion of an amphibious mobile robot that can traverse uneven terrain or confined spaces like tunnels or pipes using serpentine motions and three-dimensional dynamic aquatic environments using eel-like motions. See Sfakiotakis *et al.* (1999) for a review of fish swimming modes. The authors compared from anguilliform, through subcarangiform and carangiform to thunniform swimming movements.

The RAAMO technology can be directly applied to the exploration, monitoring and surveillance of highly constrained and inaccessible environments such as nuclear reactor cores, underground toxic waste tanks, and deep-sea exploration as well as to the human intestine and circulatory system on a microscopic scale. Still pursuing a biomimetic paradigm, RAAMO will mimic an electric sense that gives it a degree of sensory autonomy adapted to its biomimetic mode of locomotion. This electric sense is used for navigation and communication by several families of fishes whose activity is principally nocturnal and whose natural habitat is the turbid or particle-charged waters.

Swimming capacity of fishes is far superior in many ways to what has been developed by nautical science and technology. They use their streamlined bodies to exploit fluid-mechanical principles. The extraordinary efficiency of the fish as a swimming device is partly due, it now seems, to an evolved capacity to couple its swimming behaviors to the pools of external kinetic energy found as swirls, eddies, and vortices in its watery environment. The fish and surrounding vortices together constitute an unified and remarkably efficient swimming machine. In this way, they can achieve extraordinary propulsion efficiencies, acceleration and maneuverability not possible by the best naval architectures (Triantafyllou and Triantafyllou, 1995; Chablat, 2008). More particularly, as far as underwater maneuverability is concerned, the high number of internal degrees of freedom of anguilliform fish make these animals hyper-redundant locomotors capable of moving with

Figure 1: The European eel. Picture by Zienert, S. in www.fishbase.org.

great agility in constrained environments (Boyer *et al.*, 2010). For example, in Fig. 1, the European eel (*Anguilla anguilla*) counts 110 to 120 vertebras.

Research into robotic technology that can move dynamically in three-dimensions led to the development of hyper-redundant manipulators, i.e., redundant manipulators where the relative degree of redundancy is either a very large number (from the number of relatively identical rigid links) or infinite (the case of a relatively homogeneous flexible physical structure). Fig. 2 illustrates this concept. The hyper-redundant manipulators are classified into two groups. Tensors (manipulators with a fixed body length) mimic the morphology and function of snakes, elephant trunks or tentacles. Extensors (manipulators with elastic bodies or elastic sections between rigid links that can be stretched and contracted to change the overall body length) mimic more elastic animal bodies like invertebrates, such as slugs and worms. Robotic manipulators with high or infinite number of degrees of freedom can operate in highly constrained environments and articulate a larger range of motions than other systems because they have greater adaptability and versatility in their shapes.

From the mechanical design point of view the RAAMO eel-robot is composed of 12 vertebras, with 3 degrees of freedom each one, connected through a rotation free joints resulting in a set of parallels kinematic architectures, as shown in Fig.3. The good performance of RAAMO underwater biomimetic vehicle are due to the high redundancy of their internal kinematics with respect to the six-dimensional task consisted in moving their head.

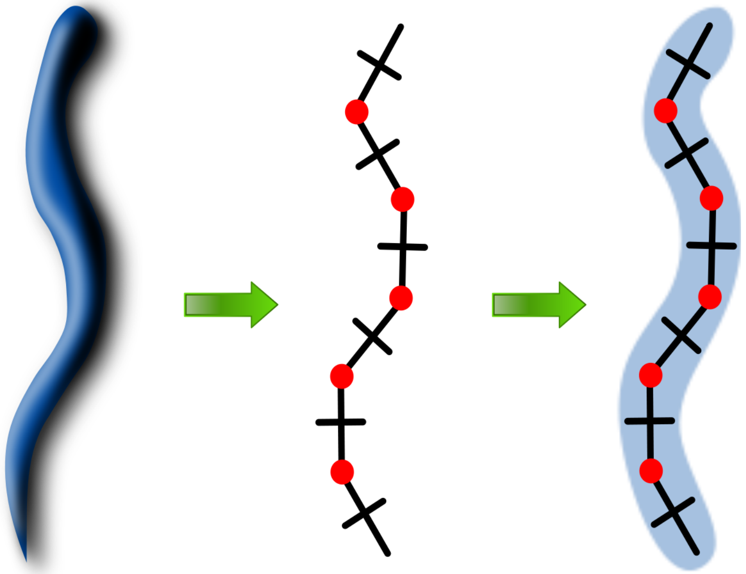

Figure 2: The eel as a redundant tensor manipulator and the body decomposition.

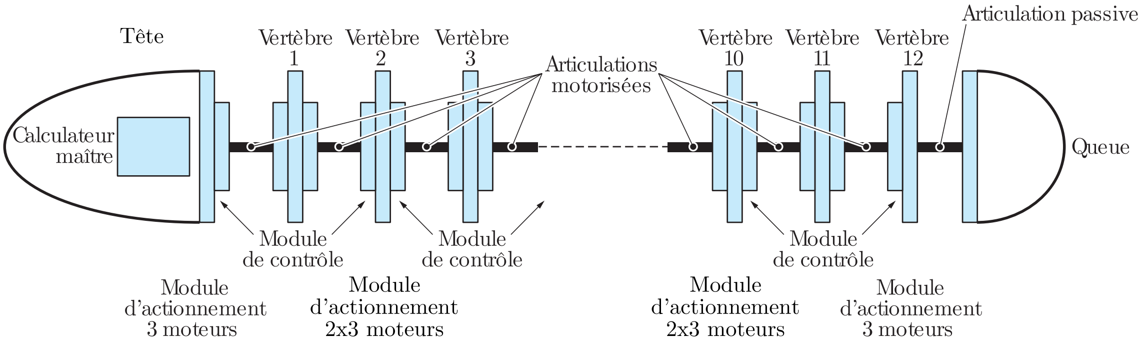

Figure 3: The eel robot assembly, extract from Boyer *et al.* (2006b).

The eel robot skin problematic

The objective of this work in the global RAAMO project is to give to the prototype a highly performance artificial skin that is especially designed to cover the prototype skeleton. This flexible organ plays at the same time the role of the animal muscles and skin. Moreover, it must be designed in order to guarantee the continuity of the robot contact with the fluid preserving the actuators energy resources.

In all projects of bio-mimetic submarine currently in progress or even accomplished, the solutions to the problem of artificial skin are similar of RAAMO interim solution used for testing the first submerged movements of the prototype. Thus, to our knowledge there is no literature specifically devoted to this problem in terms of material engineering and structural analysis. The most mature research on this subject are undoubtedly those conducted by the Massachusetts Institute of Technology (MIT)-Towing Tank Group, in particular on their Robot-Pike (Triantafyllou *et al.*, 2010) and Robot-Tuna (Mellott, 2009) projects.

To solve the problem of the skin, the MIT team developed a specific coil spring adapted to bending in the plane of propulsion. The light structure is made of a fiber glass based material coated by a stretchy membrane fabric. Because of the porosity of the membrane fabric, the robot has a hull wet. As pointed by Briand (2004) this solution, like those adopted previously, is dedicated to a robot with carangiform shape where the actuators are centered in the body of the robot, whereas RAAMO power must be distributed along the body and the place of actuators are restricted by the limitation of lateral space. An additional difficulty is induced by the eel architecture that requires a best power consumption optimization where skin deformation process must preserve the resources necessary for swimming. Moreover, contrary to all existing carangiforms robots, the RAAMO prototype can deform in three dimensions (two bendings and one torsion) as consequence of the movements of pitch, roll and yaw, presented in Fig. 4.

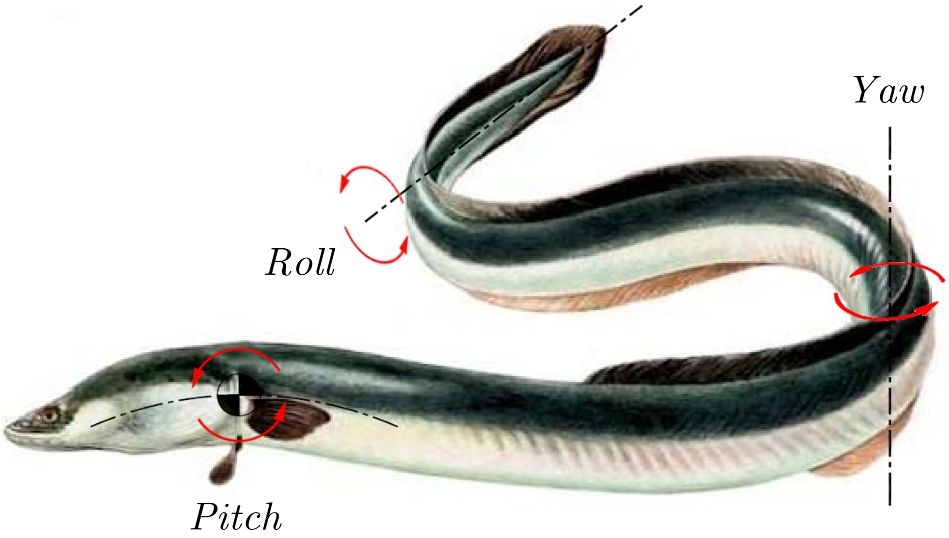

Figure 4: The eel body movements and the axis definitions.

Fig. 5 presents the geometry of a section between to vertebras with their main dimensions. For these dimensions, Briand (2004) and Boyer *et al.* (2006b) showed how the curvature radius evolves for the yaw movement and results are presented in Fig. 6. Note, for a critical case, a radius of 0.2 m is expected when the yaw angle is 30 °. In this case, the external curvature increases over 24% whereas the internal curvature decreases in 28%. The skin material must be elastically deformable in this range at a low level of strain energy. Finally, it is possible to summarize the skin main specifications:

- Provide a drag-surface since swimming involves the transfer of momentum from the fish to the surrounding water (and vice versa);
- Ensure the continuity of the body curvature as the modeling approach used in RAAMO is based on the geometrically exact continuous beam theory;

- Provide a smooth interface with the fluid without any resistance to the movement;
- Water resistent characteristic to protect the motors and other internal components from water;
- Respect the deformation power limit, estimated at 0.4 W, for each vertebra.
- Skin material must be elastically deformable on the order of 25% at a strain rate $2\,\mathrm{s}^{-1}$ approximately.
- Minimizes the internal volume variation on the order of 5%.

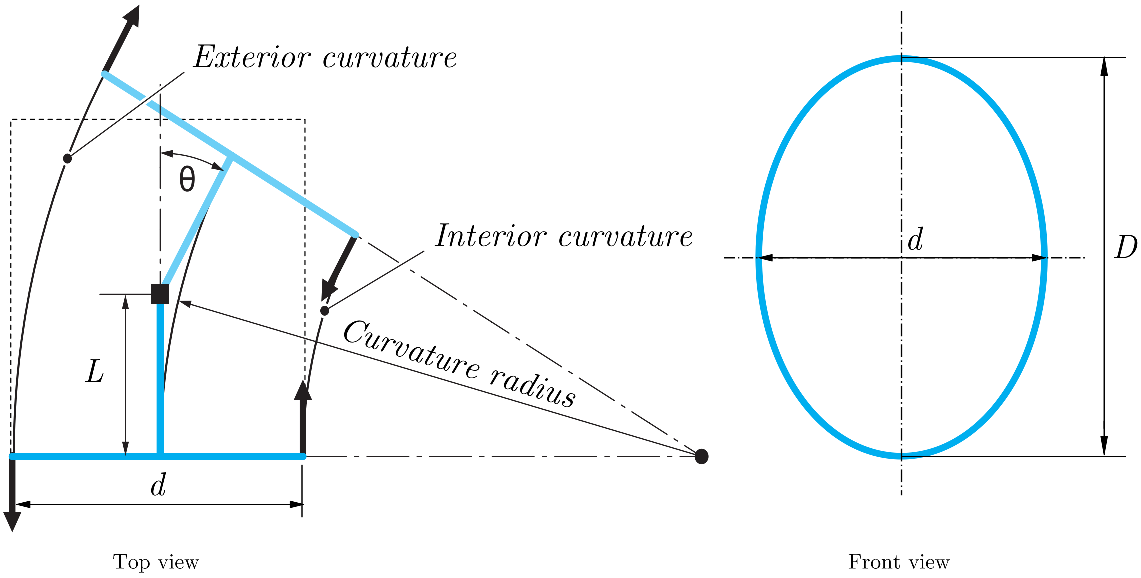

Figure 5: Intervertebral kinetics schema. With $L = 75\,\mathrm{mm}$, $D = 160\,\mathrm{mm}$, $d = 110\,\mathrm{mm}$ and $\theta_{max} = 30\,°$.

Material choice

Rubber-like materials are able to largely deform to ensure the skin problem constraints evolved in the last section. The choice of a filled silicone rubber, the RTV3428, was made to design the eel-robot skin since this type of material exhibits a suitable set of mechanical properties and especially the facility to manufacturing the skin in the laboratory environment. The final skin will be an assembly of a rigid skeleton and the silicone rubber. The rigid skeleton is necessary to minimizes volume variations due the hydrostatic pressure, seeing that the silicone rubber can be easily deformed.

RTV3428 final material is obtained from two liquid component and this class of silicone elastomer cures at room temperature by a polyaddition reaction. This type of reaction will lead to easy processing and curing. The curing process starts once the two components are mixed, at a ratio that depends on the operating temperature, i.e., the reaction can be accelerated by heat.

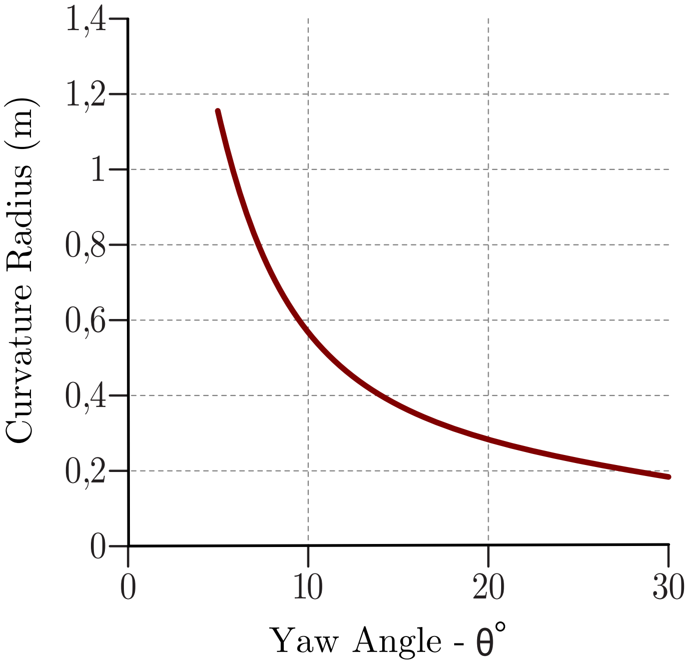

Figure 6: The curvature radius and the yaw angle relation.

This type of material is frequently employed in the production of flexible molds to be kept for long periods or where particularly accurate reproduction is required (ceramics, figurines, modelmakers, etc.) and in the production of thermal expansion formers for composite materials (the aeronautic industry, boat-building, etc.). The final piece inherently does not adhere to most materials and presents a high tear strength, compared to conventional RTV with low linear shrinkage when crosslinked at ordinary temperature. Table 4 summarizes the main mechanical characteristics of RTV3428 silicone rubber. Silicone rubber exhibits a list of attractive characteristics, but a complete experimental study aimed at analyzing and modelling the mechanical behavior of such materials is quite scarce.

Table 4: RTV3428 properties measured after curing 24 h at 23 °C. Values were extracted from the manufacturer's data sheet.

Mechanical Property	**RTV3428**
Hardness Shore A *On a 6 mm thick specimen, approx.*	28
Tensile strength at break *(Approx.)*	7.5 MPa
Elongation at break *(Approx.)*	600%
Tear strength *(Approx.)*	20 KN/m
Linear shrinkage *(7 days after curing at* 23 °C*)*	0.1%

Global aim

In order to design, modeling and optimize the RAAMO eel-robot skin, it is important to perfectly know the silicone rubber mechanical behavior. Like many filled rubber-like materials, as well as soft biological tissues and other biomaterials, filled silicone rubber exhibits highly non-linear mechanical behavior. This non-linearity is commonly characterized by large strain levels, a non-linear stress-strain response, hysteresis and strain rate dependence. Under cyclic loading conditions, the stress-softening (also called Mullins effect) behavior is observed and it is preponderant compared to other nonlinear phenomena. It is then important to characterize the stress softening to evaluate the skin swimming behavior as well the assembly operations with the robot body.

General Introduction

The word *rubber* originally comes from the natural product of the tree *Hevea Braziliensis*. The sap-like extracted from this northern Brazilian tree, often simply called *rubber tree*, is the primary source of natural rubber. Recent years have seen the development of a very large number of synthetic rubbers having a wide variety of chemical constitutions. To further improve the stiffness and the strength and among other properties of rubber, a variety of additive fillers is also employed. Thus, the term rubber gains a broader meaning which is employed to describe a class of materials, or simply called *rubber–like* materials. In this work attention is focused on the study of a particle reinforced silicone rubber.

Rubber-like materials exhibit a highly nonlinear stress-strain behavior characterized by hyperelastic deformability and incompressibility or near-incompressibility. However, all real materials are compressible to a certain degree even if the bulk modulus of the rubber-like materials is several orders of magnitude larger than the shear modulus. Moreover, some filled rubbers after loading and subsequent unloading, in general, do not return to their initial state corresponding to the natural stress-free configuration. A residual strain or permanent deformation appears. In addition, the mechanical behavior of rubber-like materials can be time-dependent and characteristics times are given by relaxation and creep experiments.

Finally, when a rubber specimen is subjected to cyclic loading, a stress softening, also called Mullins effect, is observed. This phenomenon is characterized by an important loss of stiffness during the first few cycles. Different definitions exist for the Mullins effect. In this work, Mullins effect is considered as the stress softening observed between first and second loads. Many researchers are studying this effect by means of experimental tests. Moreover, different phenomenological-based models or molecular-based models are also developed. Phenomenological models are used to describe the Mullins effect based purely on experimental observations and molecular-based models are used to explain the effect by the macroscopical nature of the rubber molecular structure. However, experimental data show that the Mullins effect is of a strongly anisotropic nature and it may not be neglected.

This PhD thesis, composed by five chapters, is a compilation thesis containing four articles exactly as they were published or submitted. The contents presented in the papers have also been analyzed in relation to the literature. Rather than describing this iterative process in detail in a dedicated chapter, it will be presented in the different parts of the thesis work.

In Chapter 1, the silicone rubber samples manufacture procedure and the experimental protocol to obtain the experimental results that illustrate the stress softening are presented. Cyclic uniaxial tension, planar tension and biaxial tension test are detailed. Experimental curves are analyzed in order to discuss which criteria are most adequate to describe the Mullins effect in an isotropic approach. The used criteria by the most representative isotropic models of the literature are compared and limitations are highlighted.

In order to enlarge the experimental data base, a detailed analysis of the bulge test is proposed in Chapter 2. Thanks to the use of three-dimensional digital image correlation measurements, the displacements and strain fields are determined for each point in the sample surface. This feature permits to comprise, in the same test, all loading cases between the planar and equibiaxial tensions. Furthermore, a method is proposed to calculate from these experimental data the membrane curvature tensor at each surface point of the bulge specimen to obtain the stress field without any constitutive equation assumption. Finally, the theoretical and experimental development are validated on experimental data from an unfilled silicone rubber perfectly hyperelastic, i.e., without Mullins effect.

Chapter 3 is concerned with the experimental characterization of anisotropy induced by the Mullins effect in a particle-reinforced silicone rubber. Due to the fact that experimental data concerning the influence of type and direction of initial loading on the subsequent stress-softening are quite scarce, a set of experimental tests were carried out on a filled silicone rubber. Uniaxial tensile test and biaxial bulge test were used to precondition the samples inducing some primary stress-softening. In both cases, subsequent uniaxial tensile tests are conducted on preconditioned specimens. These specific tests form a new important experimental data, and it permits to find an evidence for more complex memory behavior of the material. An analysis of these tests is proposed to evaluate which criteria should or should not be used for modelling Mullins effect induced anisotropy.

Based on the previous results, in Chapter 4, a new network model for finite elasticity of rubber-like materials is proposed taking into account the induced anisotropy phenomena. The model structure is built by superposing a classical hyperelastic model and a stress-softening part based on the double network theory. The core of the proposed model is the definition of a new measure of strain energy, introduced by a tensor that represents the repartition of the elongational energy in space. A new form of constitutive equation is finally proposed by comparing the energy in different directions in space. The modeling results are compared with all experimental data produced during the thesis work and the ability of the model to capture the stress softening phenomenon is underlined.

In order to use the proposed model in the analysis of engineering structures, the implementation into a finite element code is needed. Details of numerical implementation are explained in Chapter 5. First, a brief review of some essential aspects of continuum mechanics and basic kinematic relations for the description of large strain analysis are presented. Then, the initial boundary-value problem is presented as well the variational principle using two variables since displacements and pressure-field are separately interpolated due to the incompressible behavior. To simplify the implementation procedure a simplified model for anisotropic Mullins effect is proposed. Then, it is implemented into a finite element code via an user-defined material subroutine. The finite element simulation results are confronted with analytical solutions to validate the implementation.

Finally, in the last part, an overall conclusion is drawn from the findings in the previous chapters, with recommendations about possible future directions.

Chapter

1

Analysis of the isotropic models of the Mullins effect based on filled silicone rubber experimental results

G. Machado, G. Chagnon, D. Favier

Published in Mechanics of Materials 42 (2010) 841-851

The Mullins effect of rubber-like material is classically defined as the stress softening during initial loading cycles. This effect is not accounted when the mechanical properties of material are modeled by a simple hyperelastic strain-energy function. In order to capture the stress softening it is necessary to define a set of supplementary variables as well as a dissipation function, which evolves with the deformation history. In this paper, we first describe experimental results that illustrate stress softening in particle-reinforced silicone rubber for uniaxial, planar and equibiaxial tensile tests. The results allow to analyze the stress softening for the three different load cases. First, with respect to the choice of a stress-softening measure, the energy loss is evaluated by comparing the stored elastic energy for the first and the second loadings. The results point out that the virgin energy and the first invariant parameters are the best choice. Nevertheless, the maximum principal elongation, classically used in Mullins effect modeling, is not able to describe the different load cases. Furthermore, the ability of different class of models to describe filled silicone rubber is studied. The results show that models with a non-proportional and non-homothetical second load paths seem to be more efficient.

Contents

1.1 Introduction

Like many filled rubber-like materials, as well as soft biological tissues and other biomaterials, filled silicone rubber exhibit highly non-linear mechanical behavior. This nonlinearity is commonly characterized by large strain levels under static conditions, a nonlinear stress-strain response and strain rate dependence. Finally, under cyclic loading conditions, hysteresis and stress-softening behaviors are observed on both filled and unfilled elastomers. For the last half century all these cyclic phenomena were evidenced and modelled to support the most widely engineering applications. However, explanation of their microscopic mechanisms (breaking of weak chains, breaking of links, desabsorption of chains, etc.) remains non-unanimous.

Hysteresis is rather related to the dissipative nature of material, i.e., related with viscoelasticity (Bergstrom and Boyce, 2000) and viscoplasticity (Miehe and Keck, 2000) behaviors. It is characterized as the difference between the loading and unloading paths during a cycle. On the other hand, the so-called Mullins effect (Mullins, 1969) can be described as a stress-softening phenomenon of the material after a first loading. It can be idealized as an instantaneous and irreversible softening of the stress-strain curve, due to rearrangements in the microstructure of the material that occur whenever the load increases beyond its prior all-time maximum value. At times when the load is less than a prior maximum, non-linear elastic behavior prevails. One time the previous maximum stretch is reached the loading path turns up and follows the primary curve again up to a new maximum.

Through the years, the Mullins effect has experimentally been observed in different deformation states and numerous models have been proposed, but there is non-unanimous opinion on the choice of the variable to describe the evolution of the Mullins effect. Many different criteria have been chosen during the last 50 years, the most used remains the strain-energy density or the maximum principal elongation. Within this context, under the assumption of isotropy, the aims of this work are to analyze which are the most suitable modelling for Mullins effect for different loading cases. In this way, a filled silicone rubber is studied under various mechanical loadings, where the Mullins effect becomes evident. Then, the determination of the best criterion to describe the evolution of stress softening and the kind of model able to describe it for every loading cases are evaluated. Hence, the different types of modelling are summarized in 1.2. Material preparation procedures are described in Section 1.3, testing procedures and strain field measurements techniques based on optical methods are described in Section 1.4. Experimental results are then presented, in Section 2.4.1. An analyze of the strain measure criteria and the best way to model Mullins effect is finally presented in Section 1.6.

1.2 Mullins effect modelling

There exist a large number of Mullins effect constitutive equations, with different kind of isotropic or anisotropic modelling hypotheses. More and more modelling tackles the anisotropy of the Mullins effect (see for example, Ehret and Itskov, 2009; Diani *et al.*, 2006b; Miehe and Göktepe, 2005). In this paper, we focus on isotropic approaches of the Mullins effect to analyze what are the best ways of modelling. Whatever is the modelling, a deformation measure parameter is used to control Mullins effect evolution and its choice is critical.

1.2.1 Choice of the modelling

A classical approach to describe Mullins effect is to use damage mechanic theory. The strain-energy density of a virgin material $\mathcal{W}_0(\mathbf{F})$ submitted to the deformation gradient $\mathbf{F}$ can be modified incorporating continuum damage parameter d in order to take into account the stress softening. The classical form is given by

$$\mathcal{W}(\mathbf{F}) = (1-d)\mathcal{W}_0(\mathbf{F}). \tag{1.1}$$

All proposed models vary from each other by the definition of the damage criteria and the form of the damage evolution function. The definition can involve any microstructural chain damage and microvoid formations both associated with physical phenomena like breaking of chains and/or links, desabsorption of chains, etc. A common approach assumes that damage is a function of a discontinuous quantity like the maximum applied stretch or the maximal energy density with respect to the primary load path. Nevertheless, as reported by Chagnon *et al.* (2004), these models assume that the stress ratio between two different secondary load curves are related by a constant multiplicative factor:

$$\frac{P_s^j}{P_s^i} = \frac{1-d(x_s^j)}{1-d(x_s^i)} \tag{1.2}$$

where s denotes the secondary load curves numbered $i = 1, \ldots, 3$ and $j = 2, \ldots, 4$ $(i < j)$ for the presented experimental data.

Pseudo elasticity models are based on a different approach. Ogden and Roxburgh (1999) present an additive function to describe the second loading curves, this permits to have two distinguished functions to describe the first and the second loading curves. In this case, some conditions must be imposed to ensure the continuity of the strain-stress behavior. Now, no more proportionality is imposed between the second loading curves and the evolution function for the second loading curves is described by means of $\mathcal{W}_0$ measure. This permits to have a model able to characterize the different loading cases. This approach has been very employed in the past few years (see for example, Dorfmann and Ogden, 2004; Horgan *et al.*, 2004).

The double network theory is different from damage mechanics as the multiplicative function used for describing Mullins effect is not constant on the second loading curves. It can no longer be considered as a damage function as the value of the function is evolving on second loading curves and it comes back to a value of one on the first loading curve whereas the material has already be stretched. De Souza Neto *et al.* (1994), based on the

Table 1.1: Definition of damage criteria for some representative models

Variable	Description	Reference
$\sqrt{2\mathcal{W}_0(\mathbf{F})}$		Simo (1987), Miehe and Keck (2000), Septanika and Ernst (1998)
$\mathcal{W}_0(\mathbf{F})$		Ogden and Roxburgh (1999), Laraba-Abbes *et al.* (2003), Miehe (1995)
$\lambda_{\max}$	Maximum largest principal stretch	Laiarinandrasana *et al.* (2003)
$\sqrt{I_1/3}-1$	$I_1 = trace(\mathbf{C}) = trace(\mathbf{B})$	Chagnon *et al.* (2004), Qi and Boyce (2004)
$\boldsymbol{\varepsilon} : \boldsymbol{\varepsilon}$	$\boldsymbol{\varepsilon} = \frac{1}{2}\left(\mathbf{C}^{-1} - \mathbf{I}\right)$	Lion (1996)
$\sqrt{\mathbf{B} : \mathbf{B}}$	$\mathbf{B} = \mathbf{F}\mathbf{F}^T$	Zuñiga and Beatty (2002)
$\sqrt{\mathbf{e} : \mathbf{e}}$	$\mathbf{e} = \frac{1}{2}\left(\mathbf{I} - \mathbf{B}^{-1}\right)$	Krishnaswamy and Beatty (2000)
P_{max}	Maximal principal stress	Johnson and Beatty (1993)

C, B, $\boldsymbol{\varepsilon}$ and **e** are respectively the *Right Cauchy-Green, Left Cauchy-Green, Piola* and *Euler-Almansi* strain tensors. **I** denotes the so-called identity tensor.

idea of Gurtin and Francis (1981) proposed a damage master curve, that describes the evolution of the network, that is magnified to the considered maximum previous strain level.

A physical approach, proposed by Marckmann *et al.* (2002) is based on the position of the strain hardening when the material reaches it maximum previous deformation level. They assume that the macro-molecular chain network is evolving with the maximum deformation, they assume that the number of active monomers is constant. This hypothesis was relaxed by Chagnon *et al.* (2006) who considered that some chains can become hanging, that means that the number of active monomers is a decreasing function of the deformation. In another way, Qi and Boyce (2004) developed a double network model also based on evolution of chain elongation deformation measure. This permits to have independent second loading curves.

As shown, there exists a large kind of models (all existent models have not been presented here) but it seems that the choice of an energy deformation measure is quite important. This choice ensures an ability of the model to describe the different load cases, moreover the different modelling have different consequences on the strain-stress curves.

1.2.2 The history parameter choice

The choice of the Mullins effect evolution criterion is fundamental for the description of different loading cases. As pointed out by Diani *et al.* (2009), many criteria are exhibited by different authors. The Table 1.1 summarizes different choices of the past years. Usually, the choice of the measure is not justified, but is able to represent the experimental curves. For an uniaxial representation, the choice of the parameter is not essential, as all can describe the stress softening. The Mullins effect evolution function is then built in function of this parameter. Nevertheless, in a tridimensional representation, the choice becomes very crucial as it rules the position of the second loading curves in the different deformation modes. In the next sections, the experimental procedures and results are provided to enhance this discussion.

1.3 Preparation of the Silicone Specimens

The samples used in the experiments were made of a filled silicone rubber called Rhodorsil RTV3428 supplied as two liquid components: the uncured silicone and the curing agent. The final material is produced by a polyaddition, curing at room temperature. The liquid mixture is molded by injection to obtain a sheet with constant thickness. Although the experiments are performed separately and the strain states are different, data from all of the individual experiments is often used as a set. This means that the specimens used for each of the experiments must be made using the same protocol of elaboration, in order to obtain specimens with reproducible mechanical properties, as follows: (i) mixing the components with a 10/1 mass ratio, (ii) putting the mixture under vacuum for 20 min in order to eliminate undesirable entrapped air bubbles, (iii) sheet molding injection, (iv) putting mold inside an oven at 70 °C for 4 h in order to accelerate the curing process and assure a sufficient cross-linking density, and (v) sheet demolding after 1 h exposed at ambient temperature. Finally, the external surface of the molded plate was coated with a stochastic silicone paint pattern (Meunier *et al.*, 2008). Made of small speckles, the pattern is necessary for the digital image correlation (DIC) and stereo digital image correlation (SDIC)* field measurements. Note that the quality of the coated pattern (size, density and grey contrast level) is a critical point to obtain a good estimation of the strain field measurement.

1.4 Testing procedures and strain field measurements techniques

1.4.1 In-plane tests

In-plane quasi-static experiments were conducted on a MTS 4M universal testing machine with an Entran ELPM-T2 ±250 N load cell. The images were recorded at 0.5 Hz with a Jai TM-4200GE CCD camera using a reduced scan of 2048 pixels × 1000 pixels. Fig. 1.1 presents the experimental setup. First, simple tensile tests were performed on rectangular samples having an initial gauge length $l_0 = 40\,\mathrm{mm}$, width $w_0 = 13\,\mathrm{mm}$ and a thickness $e_0 = 2\,\mathrm{mm}$. Since the experiment was not intended to fail the specimen, there was no need to use a dumbbell shaped specimen commonly used to prevent specimen failure nearby the clamps. But knowing that the effects of clamps create an indeterminate state of stress and strain in the region surrounding the clamp, due to the process of gripping, the initial gauge length was adopted as being less than the real physical size of the samples. Fig. 1.2(a)

---

*also called 3D-DIC.

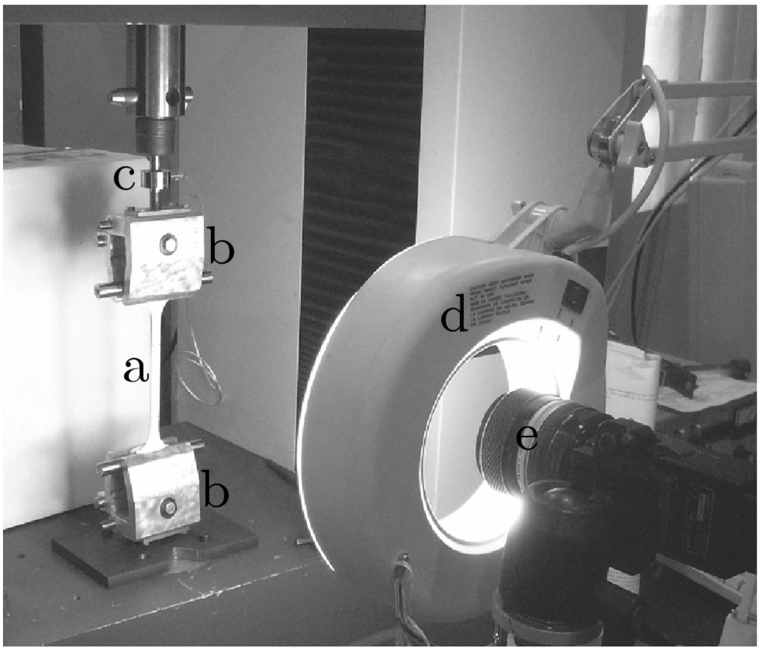

Figure 1.1: In-plane experimental setup. (a) silicone specimen; (b) clamps; (c) load cell; (d) omni light; and (e) CCD camera.

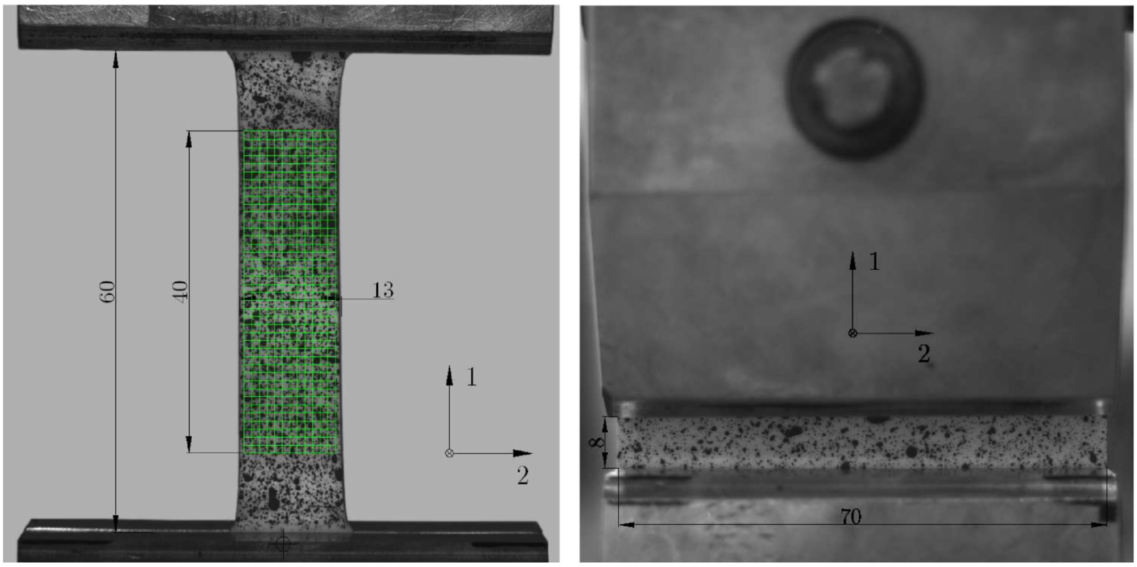

Figure 1.2: Test specimen dimensions (a) uniaxial tensile specimen (b) planar tensile specimen.

presents the tensile test specimen. Second, the pure shear strain state was approached by performing planar shear tensile test (see Fig. 1.2(b)). The initial height l_0, the constant width w_0 and the thickness e_0 of samples were 8 mm, 70 mm and 2 mm, respectively. These dimensions have as objective to create an experiment where the specimen is perfectly constrained in the lateral direction such that all specimen thinning occurs in the thickness direction.

The DIC technique, like a non-contact method, is often used to characterize rubber-like materials, see for example, Meunier *et al.* (2008) and Sasso *et al.* (2008). In each testing time step an image of the deformation of samples was recorded using a CCD camera. Using the DIC, it is possible to reconstruct the surface of the deformed samples and determinate the full-field surface displacements. An accuracy on the order of 10^{-2} pixels or better for in-plane displacement components and point-to-point strain accuracy of $\pm 10^{-4}$ in-plane can be obtained. The DIC method is preferred because there is no change in stiffness resulting from the presence of a attached sensor (classical extensiometry) and for being insensitive to ambient vibrations and rigid body motions (speckle pattern interferometry). Moreover, the method is able to deal with high strain levels, what is a very desirable feature given the high strain level experienced by the tested material. Also the DIC allows demonstrating and measuring a heterogeneous deformation field. See Sutton (2008) for further explanation about digital image correlation method.

1.4.2 Out-plane tests

A bulge test was also conducted in order to determinate an equibiaxial state. This test, also called “balloon”test, consists of a thin disk specimen, of initial diameter $d_0 = 180\,\mathrm{mm}$ and thickness $e_0 = 2\,\mathrm{mm}$, constrained between two clamping flanges. This test machine, performed at the same way in Meunier *et al.* (2008), consists of a air piston connected to the bottom circumferential clamp. The internal pressure is measured with a pressure sensor Foxboro 0-500 mbar. For these tests, out-of-plane displacements measurements were needed, therefore a Dantec Q-400 Stereo Digital Image Correlation (SDIC) system was used to acquire and correlate the images. Fig. 1.3 presents the experimental setup. Since a large out plane displacement is experienced by the silicone sample, a good focal distance is absolutely necessary. Nevertheless, a high spatial resolution is needed to permit an accurate measurement. Using the stereo-correlation it is possible to reconstruct the deformed sample surface geometry as well as determinate the displacement and strain fields. Because rigid body motion has no effect on the measurements, a high level of strain has been achieved in this kind of experiment. The Fig. 1.4 shows the strain level curves for the maximal pressure value of 18 kPa in the center of the membrane. The curvature on the top of the bulge is computed, using a post-treatment routine.

1.5 Experimental results

First, time dependence of the material is studied and then the stress softening is analyzed. Different tests are realized to evaluate the Mullins effect in different loading cases. To capture a large range of loading cases: uniaxial, planar and equibiaxial extensions are tackled. This permits to obtain very different paths in the well-known I_1, I_2 invariants plane, which is recalled under incompressibility hypothesis in Fig. 1.5.

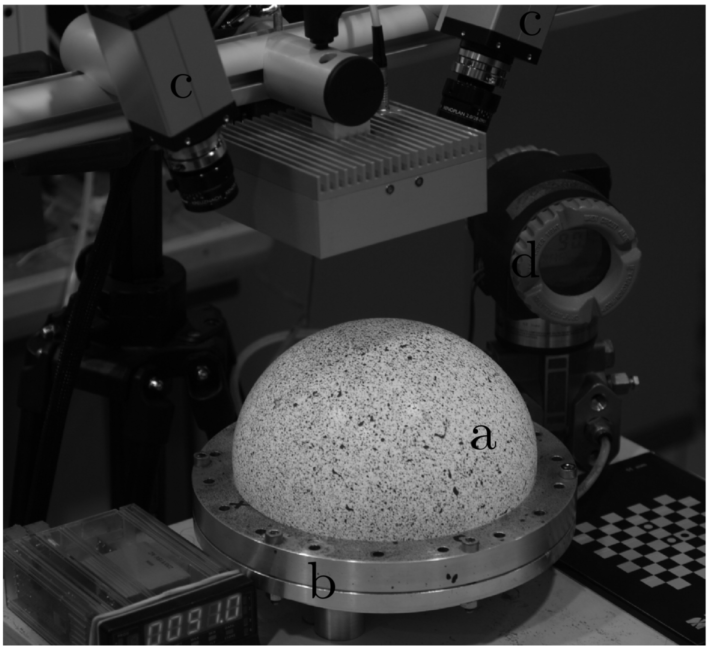

Figure 1.3: Bulging test set-up. (a) bulge specimen; (b) circular clamp; (c) CCD cameras; and (d) pressure sensor.

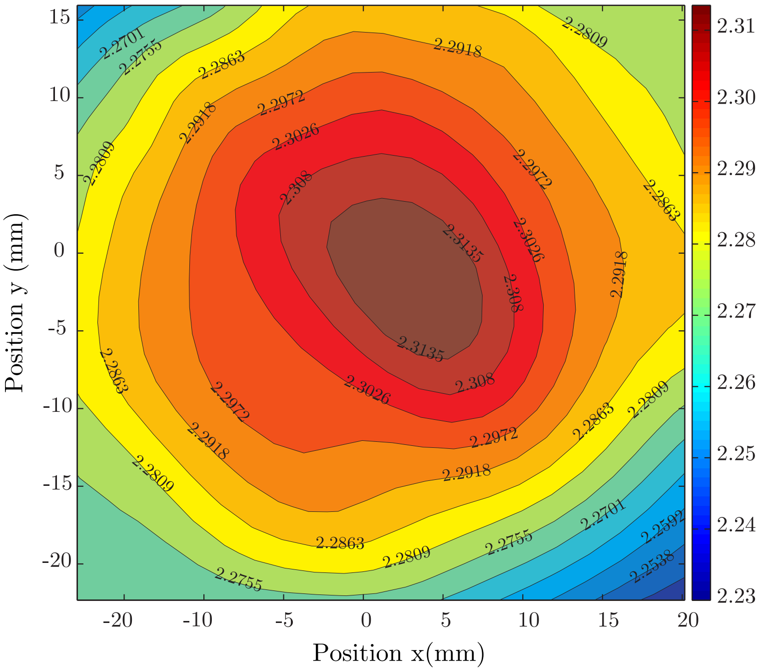

Figure 1.4: First principal strain (Green-Lagrange measure) in the center of the membrane for the maximal pressure value of 18 kPa.

1.5.1 Time dependent response

A creep tensile test was performed, where a constant monotonic load of 20 N was applied resulting in a initial stretch of $\lambda_i = 2.16$. It can be observed in Fig. 1.6 that the material

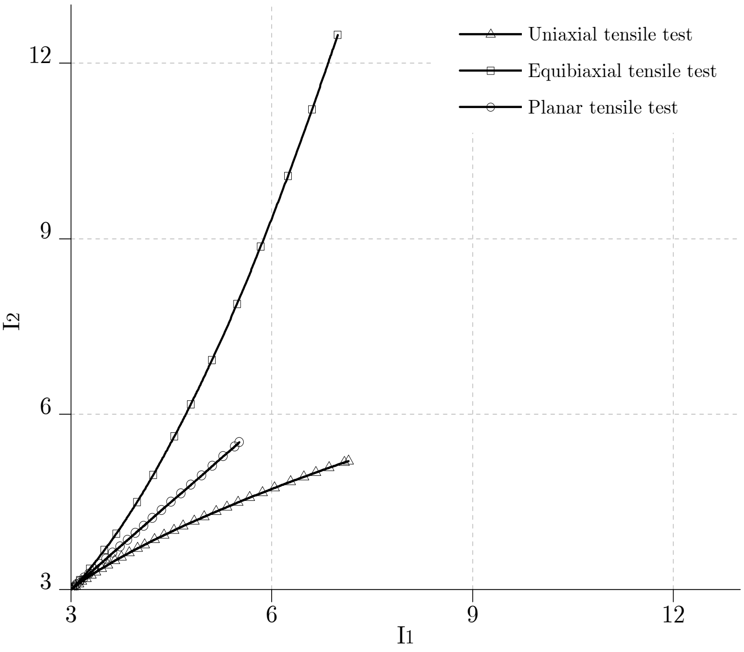

Figure 1.5: Range of deformation covered in simple tests in the invariants I_1, I_2 plane.

response tends towards an equilibrium state, which cannot be reached within laboratory time scale. However, the stretch increased by less than 1 % within the observed time range. In a second time, a tensile specimen has been subjected to a load/unload sequence at different elongation rates $\dot{\lambda} = 2.50 \times 10^{-3}\,\mathrm{s}^{-1}$ to $1.25\,\mathrm{s}^{-1}$ in order to verify the rate-dependence influence. No noticeable difference between stress-strain responses was observed at the considered strain rate range. Consequently, the RTV3428 behavior can be assumed independent of the rate of deformation for the observed ranges.

1.5.2 Uniaxial tension test

During the test, using an elongation rate of $\dot{\lambda} = 1.60 \times 10^{-2}\,\mathrm{s}^{-1}$, the nominal stress tensor $\mathbf{P}$ (*First Piola–Kirchhoff* stress tensor) is assumed to be homogeneous within the gauge region as well as the deformation gradient tensor $\mathbf{F}$. Since the current thickness is not measured, the material is assumed to be incompressible, i.e., $\det(\mathbf{F}) = 1$ for convenience. In the central zone, the deformation gradient, considering that the direction 1 is the loading one, is given by:

$$\mathbf{F} = \lambda(\mathbf{e}_1 \otimes \mathbf{E}_1) + \lambda^{-1/2}\,(\mathbf{e}_2 \otimes \mathbf{E}_2 + \mathbf{e}_3 \otimes \mathbf{E}_3) \tag{1.3}$$

and the nominal stress tensor is:

$$\mathbf{P} = P_{11}(\mathbf{e}_1 \otimes \mathbf{E}_1) \tag{1.4}$$

where $(\mathbf{E}_1, \mathbf{E}_2, \mathbf{E}_3)$ and $(\mathbf{e}_1, \mathbf{e}_2, \mathbf{e}_3)$ are the initial and deformed orthonormal basis, respectively, here identical. Table 1.2 summarizes the analytical values of the different deformation criteria, in terms of principal elongation.

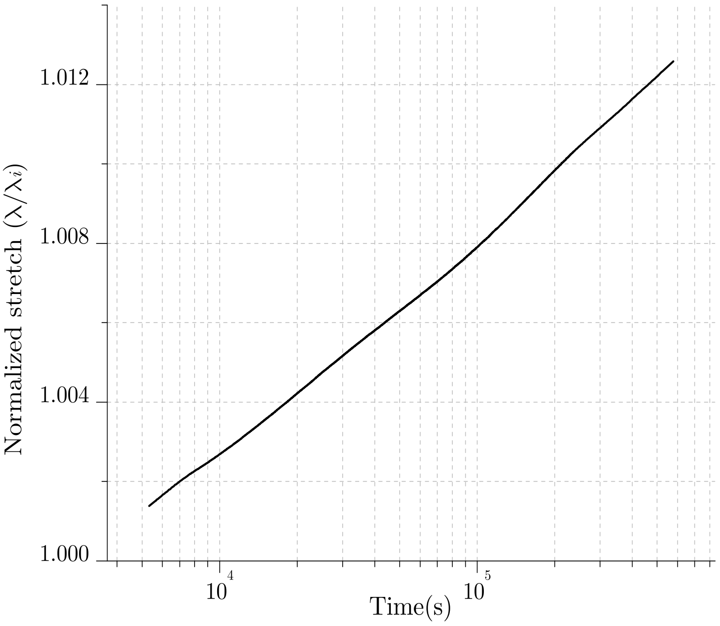

Figure 1.6: Time evolution of the normalized stretch for a creep test performed at constant load 20 N recorded after a monotonic tensile resulting in $\lambda_i = 2.16$.

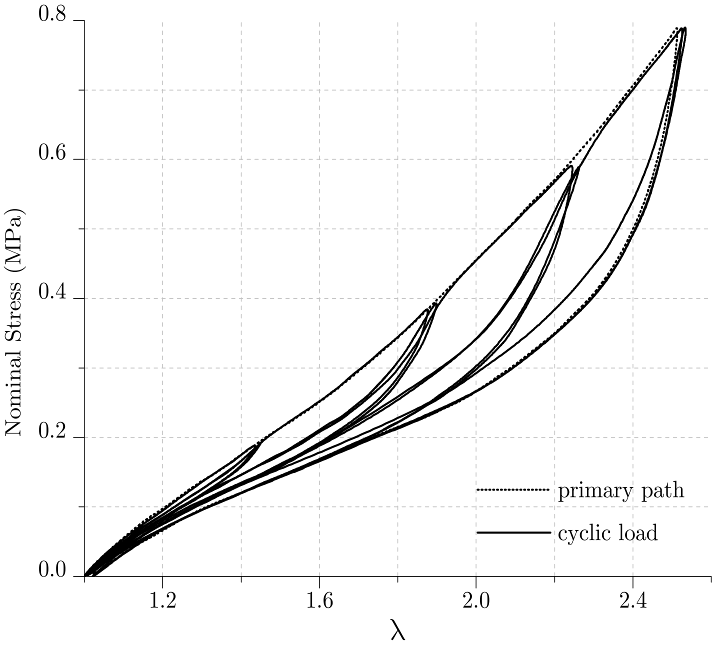

Figure 1.7: Cyclic loading-unloading tensile test with increasing maximum stress: 0.2, 0.4, 0.6 and 0.8 MPa at $\dot{\lambda} = 1.6 \times 10^{-2}\,\mathrm{s}^{-1}$.

A cyclic loading test was realized, the results are presented in Fig. 1.7. Different phenomena are highlighted, first a large Mullins effect appears by comparing the two first loading at each strain level, but with very few residual elongation. Moreover, a little hysteresis after the first cycle (difference between loading and unloading during the second cycle) is observed.

1.5.3 Plane strain tensile test

Also, the strain state during the test was supposed to be homogeneous, by assuming the direction 1 is the loading one and direction 2 is the specimen width direction, the deformation gradient tensor is expressed as:

$$\mathbf{F} = \lambda \left(\mathbf{e}_1 \otimes \mathbf{E}_1 \right) + \left(\mathbf{e}_2 \otimes \mathbf{E}_2 \right) + \lambda^{-1} \left(\mathbf{e}_3 \otimes \mathbf{E}_3 \right) \tag{1.5}$$

where the stress tensor is

$$\mathbf{P} = P_{11} \left(\mathbf{e}_1 \otimes \mathbf{E}_1 \right) + P_{22} \left(\mathbf{e}_2 \otimes \mathbf{E}_2 \right) \tag{1.6}$$

Like for uniaxial extension, the analytical values of the deformation criteria are presented in Table 1.2.

A cyclic planar loading test was realized, the results are presented in Fig. 1.8. Planar tensile response, likewise uniaxial traction, presents the same phenomena. Here, the residual stretch shows to be more evident. The maximum principal stretches experienced by the planar specimens are smaller if compared with uniaxial tensile test specimens. This limitation lies in the fact that the planar tensile specimens must be constrained in the lateral direction without slipping.

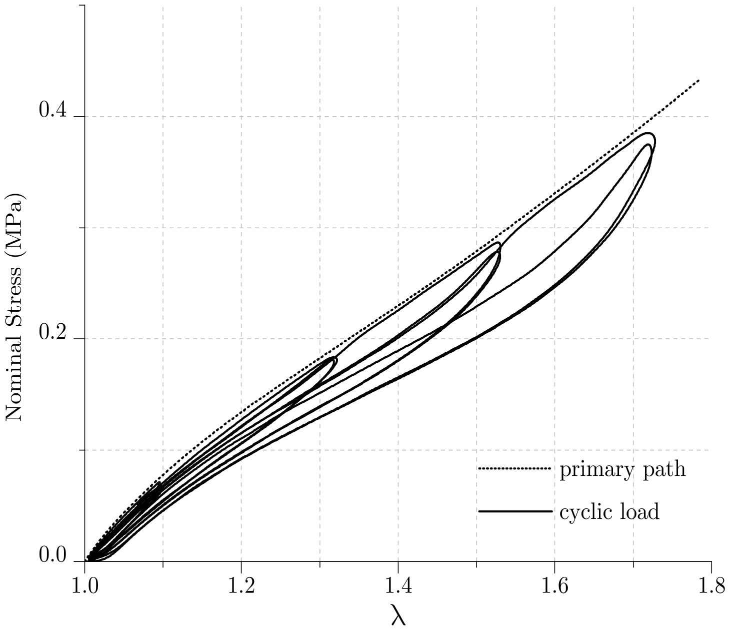

Figure 1.8: Cyclic loading-unloading planar tensile test. Maximum stress: 0.18, 0.28, and 0.38 MPa at $\dot{\lambda} = 2.60 \times 10^{-2}\,\mathrm{s}^{-1}$.

1.5.4 Equibiaxial tension state approached by the bulge test

Due to the axial-symmetry of the experimental configuration the equibiaxiality of the stress and strain is obtained on the top the inflated sample. The deformation gradient tensor in a local coordinate system is

$$\mathbf{F} = \lambda \left(\mathbf{e}_1 \otimes \mathbf{E}_1 + \mathbf{e}_2 \otimes \mathbf{E}_2 \right) + \lambda^{-2} \left(\mathbf{e}_3 \otimes \mathbf{E}_3 \right) \tag{1.7}$$

where λ is the elongation in the tangential direction of the specimen measured by SDIC. Finally, with all assumptions above, the stress tensor is given by

$$\mathbf{P} = P_{11} \left(\mathbf{e}_1 \otimes \mathbf{E}_1 + \mathbf{e}_2 \otimes \mathbf{E}_2 \right) + P_{33} \left(\mathbf{e}_3 \otimes \mathbf{E}_3 \right). \tag{1.8}$$

Similar to previous loading cases, the expressions of the deformation criteria are presented in Table 1.2.

Once thickness dimension is much smaller than the other two planar dimensions ($d_0 \gg e_0$), the stress is also assumed to be negligible along the thickness. Another consideration comes from the fact that the curvature of the inflated sample was presumed to be the same along all directions at the disk center. The component P_{11} can be calculated from knowledge of curvature radius r, the tangential elongation λ and the pressure p recorded during the test:

$$P_{11} = P_{22} = \frac{pr}{2e_0}\lambda; \; P_{33} \approx 0. \tag{1.9}$$

The results for the central area are presented in Fig. 1.9 for a cyclic loading. The response are qualitatively similar to uniaxial loadings with hysteresis and Mullins effect.

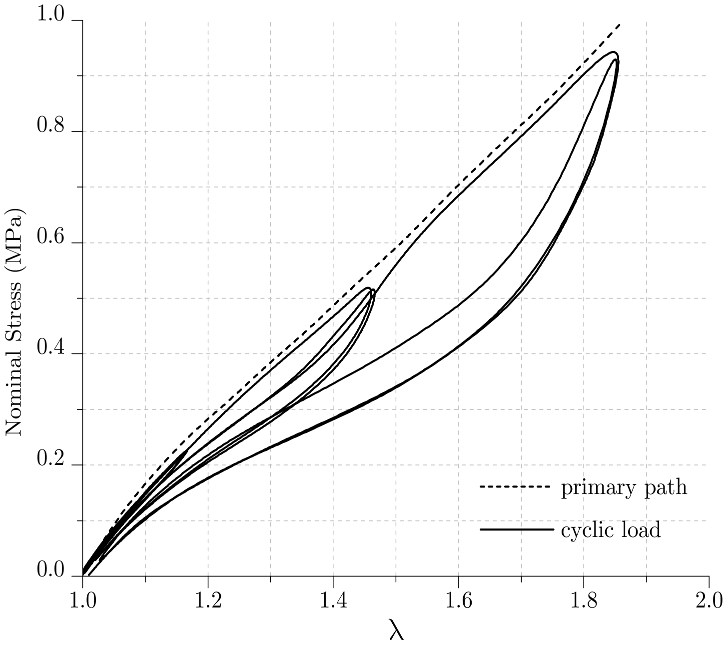

Figure 1.9: Cyclic equibiaxial stress-strain behavior obtained using the tension bulge test.

Table 1.2: Analytical expressions for the damage criteria in terms of stretch.

Criterium	Uniaxial traction	Planar traction	Equibiaxial traction
I_1	$\lambda^2 + \frac{2}{\lambda}$	$\lambda^2 + \frac{1}{\lambda^2} + 1$	$\frac{1}{\lambda^4} + 2\lambda^2$
I_2	$\frac{1}{\lambda^2} + 2\lambda$	$\lambda^2 + \frac{1}{\lambda^2} + 1$	$\lambda^4 + \frac{2}{\lambda^2}$
$\sqrt{\mathbf{B}:\mathbf{B}}$	$\sqrt{\lambda^4 + \frac{2}{\lambda^2}}$	$\sqrt{\lambda^4 + \frac{1}{\lambda^4} + 1}$	$\sqrt{\frac{1}{\lambda^8} + 2\lambda^4}$
$\boldsymbol{\varepsilon}:\boldsymbol{\varepsilon}$	$\frac{1}{4}\left(\frac{1}{\lambda^2} - 1\right)^2 + \frac{1}{2}\left(\lambda - 1\right)^2$	$\frac{1}{4}\left[\left(\frac{1}{\lambda^2} - 1\right)^2 + \left(\lambda^2 - 1\right)^2 + 1\right]$	$\frac{1}{4}\left(\lambda^4 - 1\right)^2 + \frac{1}{2}\left(\frac{1}{\lambda^2} - 1\right)^2$
$\sqrt{\mathbf{e}:\mathbf{e}}$	$\sqrt{\frac{1}{4}\left(\frac{1}{\lambda^2} - 1\right)^2 + \frac{1}{2}\left(\lambda - 1\right)^2}$	$\sqrt{\frac{1}{4}\left[\left(\frac{1}{\lambda^2} - 1\right)^2 + \left(\lambda^2 - 1\right)^2 + 1\right]}$	$\sqrt{\frac{1}{4}\left(\lambda^4 - 1\right)^2 + \frac{1}{2}\left(\frac{1}{\lambda^2} - 1\right)^2}$

Note that $\mathbf{B}:\mathbf{B} = (I_1)^2 - 2I_2$ and $\boldsymbol{\varepsilon}:\boldsymbol{\varepsilon} = \mathbf{e}:\mathbf{e}$.

1.6 Discussion

On the one hand, using the experimental data, we propose to analyze the consequence of the choice of a stress-softening measure. In agreement with the usual consideration that the main part of the Mullins effect is represented by the difference between the first and the second loading paths, the energy loss is evaluated by comparing the stored elastic energy for the first and the second loadings. The evolution of the ratio of these two quantities is plotted according to all the Mullins effect measure parameters of Table 1.1, for the three loading cases: uniaxial and equibiaxial extensions and planar tension. The results are presented in Fig. 1.10. It can be noticed that none of the parameters presents a perfect correlation for all loading cases. Although, for the tested strain range, it seems that the virgin energy ($\mathcal{W}_0$) and the first invariant (I_1) parameters are the best choice. The maximal principal stress (P_{max}) can be acceptable for low strain levels. What clearly appears is that the maximum principal elongation ($\lambda_{\max}$), usually used in Mullins effect modelling, is not able to describe the different loading cases. All the other parameters derived from the trace operator of a strain measure are not more efficient. All these measures become less and less efficient at large deformation. It emphasizes the fact that the Mullins effect should be described by $\mathcal{W}_0$ or I_1 parameter. All this means that the use of a non-efficient parameter implies the construction of the second loading modelling on wrong bases. Whatever is the model, the evolution function used to describe the stress softening will be fitted on a non-adequate parameter. Many Mullins effect modelling have a large number of parameters, this permits to have a good fit, but if the wrong deformation criterion is used, the physics of the phenomenon is lost.

On the other hand, some modelling hypotheses are discussed. A damage modelling approach imposes to these ratios to be constant whatever is the maximum deformation parameter. Fig. 1.11 presents the ratios between the different second loading curves (plotted according to the principal elongation). The beginning of the curves varies very quickly, but this is due to experimental errors which are more significative at low strain levels. It clearly appears that no damage model can correctly represent the Mullins effect of a mate-

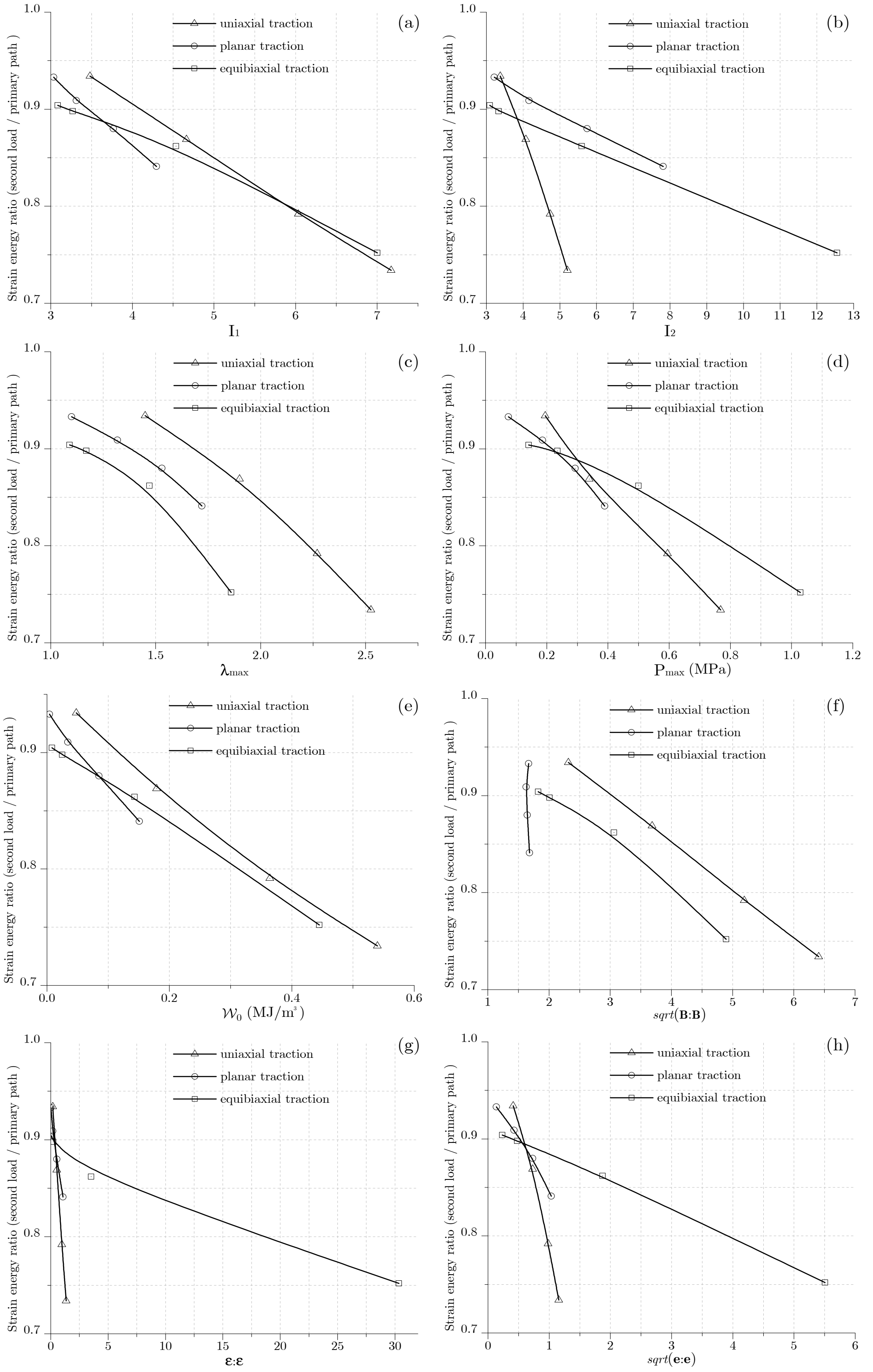

Figure 1.10: Energy loss between the primary path and the second load for the different mechanical loadings with respect to (a) the first strain invariant I_1; (b) the second strain invariant I_2; (c) maximal principal stretch $\lambda_{\max}$; (d) maximal principal stress P_{max}; (e) strain energy density $\mathcal{W}_0$; (f) *Left Cauchy-Green* strain measure; (g) *Piola* strain measure; (h) *Euler-Almansi* strain measure.

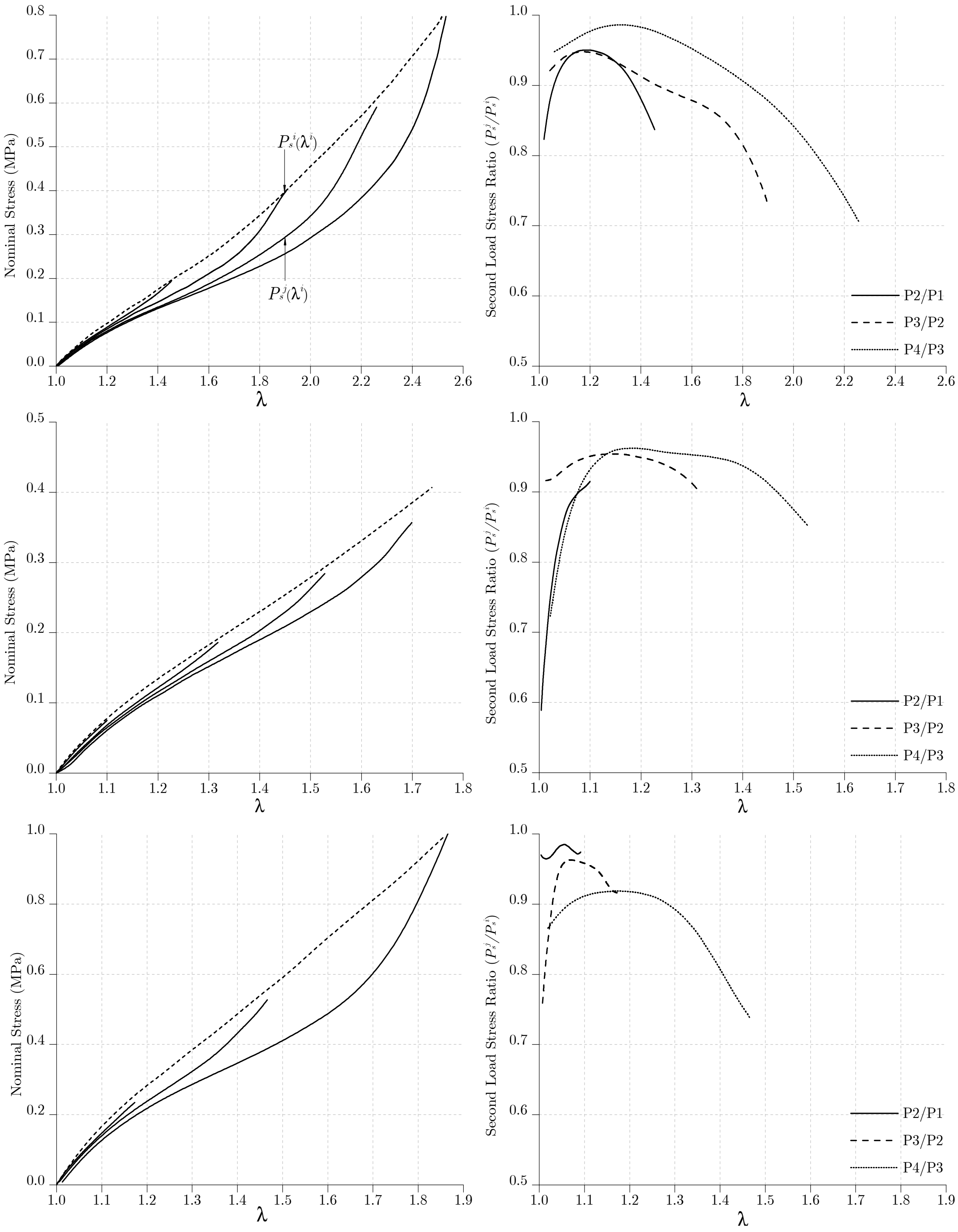

Figure 1.11: Second loads ratio. Rows correspond, respectively, to uniaxial planar and equibiaxial tensile tests. In the left column dot lines represent the primary path and continuous lines are the second loads. The right column shows the ratio between second loads.

rial that has a similar behavior than the RTV3428 silicone. A choice must be done, but the beginning of second loading curves and strain hardening cannot be described correctly at the same time using these models. The proportionality between the second loading curves prevents from describing large strain hardening, then it can only be applied to materials that have a weak influence of Mullins effect. But this discards the imposition of proportionality between second loading curves, like proposed by Beatty and Krishnaswamy (2000) and Zuñiga and Beatty (2002). But their proposition is written thanks to a strain measure that does not seem to be very efficient to characterize all loading cases. This was improved by Zuñiga (2005) by changing the strain measure to an energy measure. An interesting analysis and criticism of this model is proposed by Kazakeviciute-Makovska (2007).

De Souza Neto *et al.* (1994) proposed a master second loading curve to describe Mullins effect, the curve is magnified to join the stress-free state to the maximum deformation. Fig. 1.12 presents a normalization of the strain-stress curve for the three simple tests for the maximum strain and the normalized strain energy. It clearly appears that all the curves are not superimposed, that means that the idea of a single master curve is not adequate. The form of the second loading curve is varying a lot, according to the maximum deformation. The strain hardening is very different and is not appearing at the same in a second loading curve. This phenomenon is also more important for natural rubber because of strain induced crystallization.

All these remarks emphasize the fact that an efficient Mullins effect modelling, by an isotropic approach, must not use a formalism where the second loading curves are proportional or homothetical. The modelling should be able to describe different forms of strain-hardening according to the maximum previous deformation level. Moreover, governing Mullins effect parameter should be built thanks to different loading cases; a simple uniaxial test can drive to abnormal conclusion. We suggest to use the elastic energy or the first strain invariant. The physical or pseudo-elastic approaches seem to be the best way to tackle correctly Mullins effect evolution functions to be able to well describe all second loading curves.

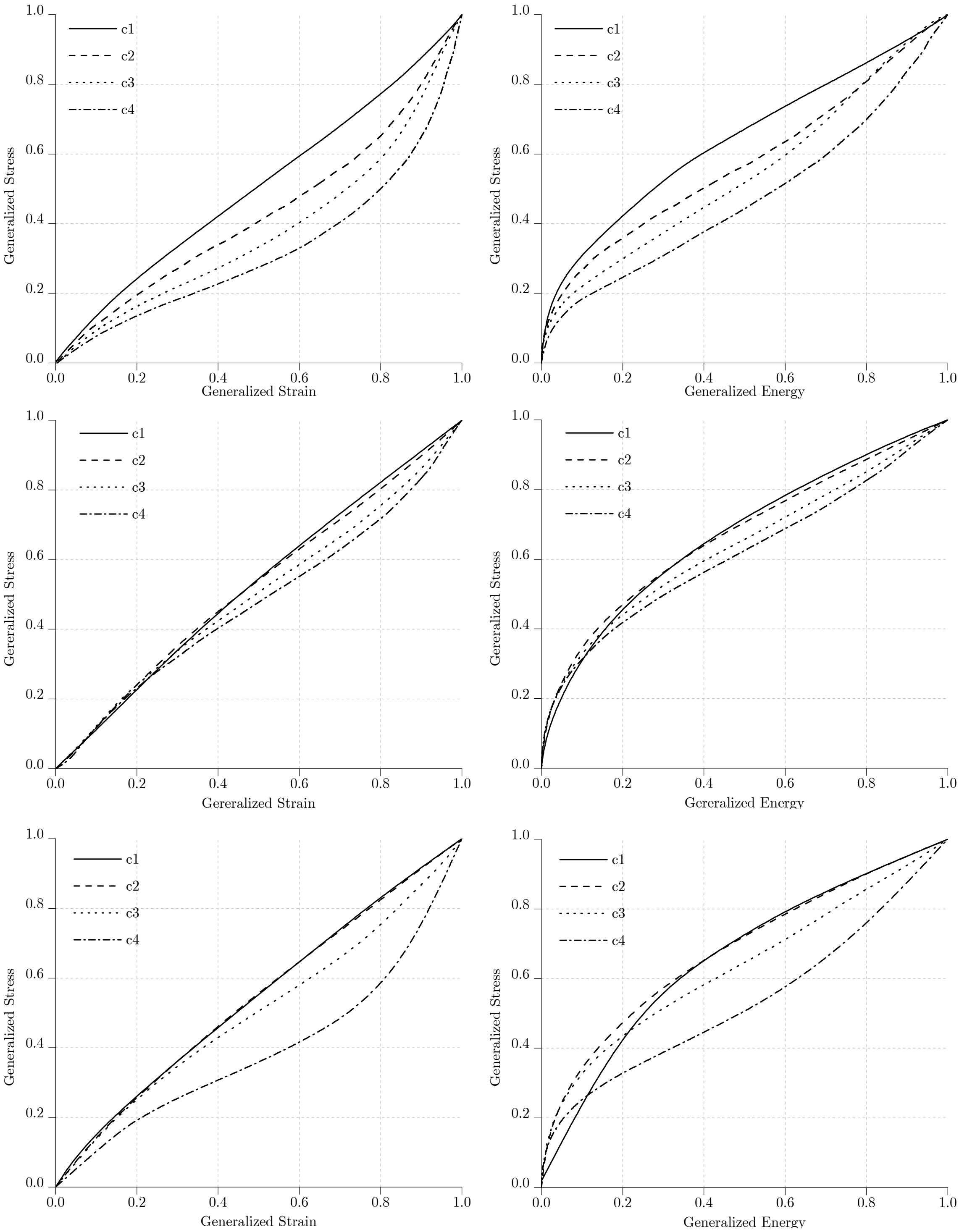

Figure 1.12: Normalized second stress loading curves with respect the maximum strain (left column) and the normalized energy of deformation (right column). Rows correspond, respectively, to uniaxial planar and equibiaxial tensile tests.

1.7 Conclusion

In this paper, limitation of isotropic models of the Mullins effect have been tackled thanks to experimental tests. In this way, filled silicone rubber has been characterized. The reproducibility and accuracy of measurements were evaluated through several successive tests. Results have shown that our protocol to manufacture the silicone specimens and our experimental methodology work well and provide a precise experimental characterization of softening phenomena. Uniaxial, equibiaxial and planar tensions have been realized, this permits to compare first and second loading curves in different loading modes. Energy losses are compared and analyzed. It clearly appears that the strain energy measure ($\mathcal{W}$) is the best choice and in a lesser the first strain invariant (I_1).

The analysis of experimental data proved that proportionality between second loading curves is not a good way to model the strain-stress curves. There are two main ways to well describe the Mullins effect. The first one, by using a non-constant multiplicative function on second loading curves or by using different non-proportional functions, this, respectively, corresponds to double-network and physical approaches.

The governing parameters and description function forms have been analyzed under isotropic assumption. The main extension of this study is to, now, take into account the influence of the loading direction of the stress softening.

CHAPTER

2

Membrane curvatures and stress-strain full fields of bulge tests from 3D-DIC measurements. Theory and validation on virtual and experimental results.

G. Machado, D. Favier, G. Chagnon

Submitted to Experimental Mechanics

The bulge test is mostly used to analyze equibiaxial tensile stress state at the pole of inflated isotropic membranes. Three-dimensional digital image correlation (3D-DIC) technique allows the determination of three-dimensional surface displacements and strain fields. In this paper, a method is proposed to determine also the membrane stress tensor fields, independently of any constitutive equation. Stress-strain state is then known at any surface point which enriches greatly experimental data deduced from bulge tests. Our method consists, first in calculating from the 3D-DIC experimental data the membrane curvature tensor at each surface point of the bulge specimen. Then, curvature tensor fields are used to investigate axisymmetry of the test. Finally in the axisymmetric case, membrane stress tensor fields are determined from meridional and circumferential curvatures combined with the measurement of the inflating pressure. Our method is first validated for virtual 3D-DIC data, obtained by numerical simulation of a bulge test using a hyperelastic material model. Afterward, the method is applied to an experimental bulge test performed using as material a silicone elastomer. The stress-strain fields which are obtained using the proposed method are compared with results of the finite element simulation of this overall bulge test using a neo-Hookean model fitted on uniaxial and equibiaxial tensile tests.

Contents

2.1 Introduction

Modeling the deformation behaviour of materials requires first of all its experimental characterization which in a classical manner is based on simple mechanical tests, e.g., uniaxial tension, equibiaxial tension, pure shear tests and others. These tests, under an assumption of uniform strain and stress fields in the zone of interest, are the starting point to propose constitutive equations aiming to describe various kinds of more or less ideal material response, in order to approximate physical observation of real material response. Modeling the deformation behavior of a given material requires then to identify material parameters of the adopted constitutive equation. Considering the current development and flexibility of full-field measurements techniques, tests under non-uniform conditions can be conducted providing very rich experimental data. As pointed out in Avril *et al.* (2008), performing experiments of increased complexity thus allows extracting more (and more reliable) information from small numbers of tests. However, the developed methods consist mainly in constitutive parameter identification, namely the finite element updating method, the constitutive equation gap method, the virtual fields method, the equilibrium gap method and the reciprocity gap method. All these identification techniques require to adopt a specific constitutive equation (elasticity, plasticity, viscoplasticity, hyperelasticity, etc.) to exploit full-field measurements.

In the past fifty years, the inflation of a plane circular membrane (or simply called bulge test) has become a very useful technique to characterize material mechanical behavior. The mechanical test of an initially flat membrane constrained between two circumferential clamps subjected to a lateral hydrostatic pressure was used by many authors to examine mechanical properties of different types of materials. It was the first experimental method adopted by Treloar (1944) to describe vulcanized latex behavior and determine their analytical model parameters. In plasticity field, Brown and Thompson (1949) used the bulge test for five different alloys covering a wide range of stress-strain and failure characteristics. Bulge tests were also used to investigate mechanical properties of thin films, for determining residual stress, Young's modulus and Poisson's ratio (Tsakalakos, 1981; Mitchell *et al.*, 2003). In the study of biological soft tissues, the bulge test is an important tool, for example, for understanding the aneurysms multiaxial stress and strain fields (Seshaiyer *et al.*, 2001), for studying the mechanical properties of human tissues (Miller, 1979; Kriewall *et al.*, 1983) and for measuring the finite load-deformation behavior of a sheet of living cells cultured on a mesoscopic freestanding elastomer membrane (Selby and Shannon, 2007). More recently Grolleau *et al.* (2008) combined a Hopkinson bar system with a conventional bulge test to study the biaxial testing of sheet materials at hight strain rates.

On the theoretical point of view, the bulge test was as well studied in detail. A seminal work was proposed by Adkins and Rivlin (1952) that details the boundary value problem, in the field of nonlinear elasticity, associated with the Mooney isotropic membrane inflation. Other important work has come from Hill (1950) introducing a theoretical analysis of plastic flow at the pole of a metal diaphragm, which is bulged plastically, based on the Lévy-Mises stress-strain equations. In an analogous manner, Ross and Prager (1954) showed that the use of Tresca's yield condition and associated flow rule leads to a simple theory where the basic equations can be integrated in closed form even for finite deflections.

Bulge test was mostly conducted as an easy way to determine mechanical behavior of isotropic materials subjected to equibiaxial tensile stress state. Indeed, due to the axial symmetry of the problem and respecting the primary assertions of the membrane theory, the equibiaxiality of the stress and strain is obtained at the top of the inflated sample. Found over the pole neighborhood, where is supposed to exist a spherical cap, the equibiaxial stress-strain state can be easily calculated from knowledge of the curvature radius, tangential elongation and of the pressure recorded during the test. Such approach was used for recent examples for rubber-like materials in Meunier *et al.* (2008) and Sasso *et al.* (2008), and for NiTi superelastic sheets Grolleau *et al.* (2011). However, the current shape of the total bulge is rarely spherical, as shown in Dudderar *et al.* (1977) using the two-source holographic technique. Therefore, much more information is available from axisymmetrical bulge test than stress and strain states at the pole if the pressure and principal curvatures fields are measured. The membrane stress tensor can be determined from these data using membrane theory and equilibrium equations without any explicit constitutive equation. However, the accurate experimental measurement of curvatures is not a simple task. Indeed, for this reason, a relation that describes the material behavior was often used in the past. In this case, the principal curvatures are often written in terms of the principal stretch ratios and replaced in the Lagrangian form of the equilibrium equations. In a general manner, this procedure intends to reduce the problem to a first order system by introducing new variables (Wineman, 1976; Yang and Feng, 1970). As a consequence, there is also loss in generality in assuming an explicit form for the constitutive relation which is chosen to represent the material. See for example the works Klingbeil and Shield (1964) for hyperelastic potentials; Wineman (1978) and Feng (1992) for viscoelastic behavior.

In a classical manner, the bulge specimen is supposed to be deformed axisymmetrically and profiles are measured. In that case, meridional curvature is directly measured and circumferential curvature is deduced under axisymmetric assumption (Hsu *et al.*, 1995). The accuracy of this process heavily depends on the finite number of experimental measurements points, and information data is restricted to a meridional path only, i.e., this manner to compute the principal curvatures is restricted to axisymmetric problems. Regardless, a numerical procedure must be employed to solve the coupled nonlinear differential problem.

In this context, the present work intends to provide an useful method to obtain the membrane stress and strain fields during the bulge test using the three-dimensional digital image correlation (3D-DIC) technique. The 3D-DIC is able to capture three-dimensional surface geometry and displacements of the deformed surface. This paper explains how these kinematical fields permit to evaluate in each point of the membrane the strain and curvatures fields, and the stress field in the axisymmetrical hypothesis. Section 2.2 starts with a brief description of 3D-DIC technique, where the bases of contour and strain measure principles are outlined. In the same section, the theoretical framework for evaluation of the first and second fundamentals forms of surface and relations between principal curvatures and membrane stress are emphasized. Thus, a method to determine the curvature fields from 3D-DIC data is presented. Then we show that curvature fields combined with the measurements of the inflation pressure allow calculating the stress fields for an axisymmetric bulge. In Section 2.3, a finite element calculation is realized on a Mooney hyperelastic membrane to emulate experimental data, i.e., generate a virtual 3D-DIC information. These data permit to validate the curvature calculation method and estimate errors in stress determination. In Section 2.4 the method is applied to real experimental data. The experimental results obtained in the bulge test of a silicone rubber-like material are presented. All precautions concerning the experimental setup are emphasized. The tridimensional correlation process is not perfect in view of missing and outlying values that can occasionally occur, a strategy is invoked to treat these occurrences. Finally, the experimental data fields are compared to a finite element model carried out using a neo-Hookean hyperelastic law fitted on uniaxial and equibiaxial tensile tests. This permits to highlight the advantages of the proposed method compared to usual methods of analysis of bulge test.

2.2 Theoretical framework

2.2.1 A brief outline of 3D-DIC

In the 3D-DIC technique, random gray-value dot patterns on specimen surfaces are observed by two cameras in a stereoscopic setup. Also called stereo digital image correlation (SDIC), the 3D-DIC is based on both stereo-vision technique and digital image correlation (DIC). A comprehensive description of metrological aspects of 3D-DIC technique can be found in the literature, e.g. Luo *et al.* (1993), Sutton (2008) and Sutton *et al.* (2009). For references on applications of stereo-vision and 3D-DIC to experimental mechanics, see Orteu (2009).

The stereo-vision technique permits to recover the three-dimensional information of a scene from two different view points. Considering a physical point M of coordinates X^i in a Cartesian reference frame to be measured. Forward, Latin indices represent the values 1, 2, 3 and, the Greek ones the values 1, 2. The stereo-projections of the point $M(X^i)$ on the images planes of two cameras $C1$ and $C2$ are given by $M_{C1}(X^{\alpha}_{S1})$, $M_{C2}(X^{\alpha}_{S2})$, where X^{α}_{S} are the camera sensor coordinate system. Every deviation from the straightness of the projection can be related to the presence of radial and tangential distortions. Fig. 2.1 illustrates the epipolar geometry, i.e., the geometry of stereo vision, with pinhole C, focal length f , and image plane center P, imaging a general object point M. It is convenient to define a set of coordinate systems to represent the imaging process. The first coordinate system is the global coordinate system (GCS), with axes (X^1, X^2, X^3). The second coordinate system typically defined is the camera coordinate system (CCS) located at the pinhole C. The third set of axes defines the sensor coordinate system (SCS) with X_S^1, X_S^2 in terms of pixels, where a pixel defines positions/sensor locations.

The 3D-DIC uses a DIC algorithm to determine point correspondences between two images of a specimen acquired at the same time from two bounded cameras. The digitized images are compared to match subsets - so called facets - from one image to another. The facet is a square area, with size f_{size} pixels, around the evaluation grid point which is used from the correlation algorithm in order to identify the corresponding area in another image. The correlation scores are computed by measuring the similarity of a fixed facet in the first image to a shifting subset window in the second one. With knowledge of the imaging parameters for each camera and the orientations of the cameras with respect to each other by a calibration procedure, the position of each object point in three dimensions is calculated. The minimal facet size (f_{size}) is limited by the size and roughness of the stochastic pattern on the object surface. Each facet must contain a characteristic part of the pattern with good contrast features.

As a result, the 3D-DIC provides a set of physical points M in terms of Cartesian coordinates X^i in a global reference system, arbitrarily defined during the calibration phase. The calibration, in the commercial system used in this work, is done by taking a series of exposures of a calibration target with both cameras simultaneously, i.e., both cameras are calibrated as a stereo rig. The calibration target is a chess pattern with known geometry and this target is put into different spatial orientation with respect to the cameras sensors. The software detects the corners of the squares. Additional circular markers placed on the target surface define the center and the orientation of the calibration target. The evaluation algorithm calculates the intrinsic parameters (focal length f, image plane center P, radial and tangential distortion parameters) for each camera. Intrinsic parameters are influenced by focal lens, focal distance and aperture and they are considered as intrinsic since the cameras remain in fixed positions relative to each other during the experiment. The evaluation algorithm calculates as well the extrinsic parameters (translation vector and the rotation matrix between the GCS and the SCS) which in turn are influenced by the intrinsic parameters and the positions of the cameras. Finally, the uncertainties of the calibration parameters, resulting from the deviations of the detected markers from the model positions are calculated. Typically a total number of ten images are sufficient to calculate all calibration parameters accurately. A comprehensive description of the 3D-DIC calibration method with the mathematical development can be found in Sutton (2008).

Note that the spatial resolution (S_{res}) of the discretized surface depends essentially on camera sensor resolution (C_{res}) and on the choice of the evaluation grid. The grid spacing (G_s) is the distance between the grid points in pixel and therefore set spatial resolution or the distance between the data points on the object. Thus, grid spacing limits the spatial resolution, as each grid point represents one single data point of the result. Finally data output is arranged in a matrix representation in the form $X^i(u, v)$ where the integer values $u, v \in [1, \lfloor C_{res}/G_s \rceil]$ are respectively lines and columns indices of the matrix representation for each coordinate (X^i). See the scheme in Fig. 2.1.

Once the 3D contour has been determined, the next step in digital 3D correlation is the determination of the three-dimensional deformation of the object surface. This

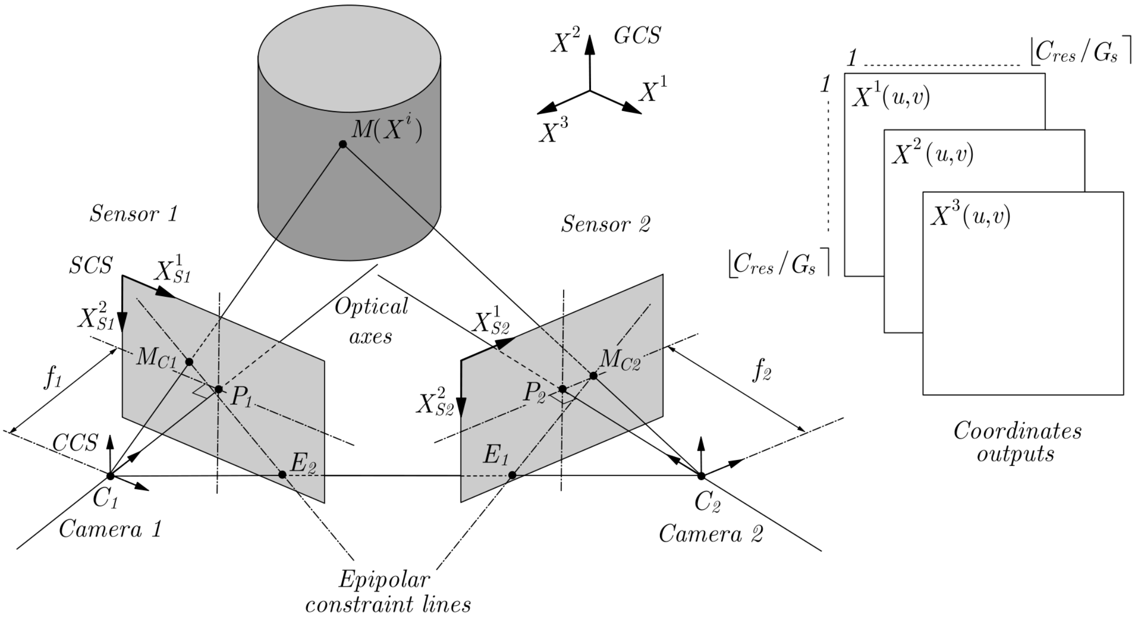

Figure 2.1: Representation of the epipolar geometry and the coordinates output format.

process is carried out by correlation of the images, taken by both cameras in the deformed state, with their original reference images. To evaluate the 3D displacement field, 3D-DIC determines point correspondences between the stereo pairs acquired before and after deformation. The correlation algorithm tracks the observed gray value patterns for each camera and transforms corresponding facet positions in both cameras into 3D coordinates for each deformation step, resulting in a track of each surface facet in 3D space and over time. With the known position vectors of each surface point and the reference contour, the strains can be determined by calculating the gradient of the deformation or by the distortion of the facets, i.e., they can be derived either directly by the differentiation of the displacements of adjacent surface points or measured pointwise by the analysis of the distortion of each local facet, which was used for correlation (Sutton, 2008; Sutton *et al.*, 2009).

2.2.2 Errors sources on the 3D-DIC

The evaluation of a 3D correlation measurement results in 3D coordinates, displacements and in-plane strains on the specimen surface. The corresponding data uncertainties originate from different sources, which can be divided into three categories Becker *et al.* (2006): statistical correlation errors, systematical correlation errors and 3D reconstruction errors. Statistical correlation errors are principally related to the limited number of pixels and corresponding gray values in each facet, and finally by the fact that the facet position has to be determined with subpixel accuracy. Additional potential error sources are statistical noise of the gray values, different illumination conditions for the two cameras, image contrast and size of the speckle pattern on the specimen surface. Systematical correlation errors are introduced by subpixel effects. They might occur if the facet transformation model used is not appropriate to describe the complexity of the real transformation, e.g., in a curved specimen surface or for significant lens distortions (see reference Schreier and Sutton (2002) for details). Systematical errors build a principal limitation for the resolution of the resulting data Becker *et al.* (2006). Finally, uncertainties of the calibration parameters lead to errors, when reconstructing the 3D coordinates. Calibration errors appear in a systematical manner as a function of the facet positions in the camera frames, causing local distortions of the reconstructed 3D space. However, results from multiple experiments performed in (Sutton, 2008) indicate a typical accuracy for the displacement field on curved or planar specimens, on the order of ± 0.01 pixels for the in-plane components and $D/50000$ in the out-of-plane component, where D is the distance from the object to the camera, for typical stereo-camera arrangements. The point-to-point accuracy of $\pm 10^{-4}$ for the in-plane surface strains is achievable even when the object is subjected to large rigid-body rotations and arbitrary amounts of rigid-body translations since these motions do not corrupt the strain measurements.

2.2.3 Curvature evaluation from coordinates fields measured by 3D-DIC

Using the 3D-DIC, the reference surface Ω_0 of the object in question is discretized by a regular grid that represents the surface curvilinear coordinates Θ^α. These coordinates are obtained directly from the grid placed by 3D-DIC using the grid indexes $\Theta^1 = u$ and $\Theta^2 = v$ where u and v are respectively lines and columns indices of the matrix representation $X^i(u, v)$. This grid maps any discrete point M_0 of the undeformed body, associating a set of curvilinear coordinates, so called Θ^α–*curves*. Since the coordinates Θ^α are convective, these curves are subjected to the same deformation as the body, and are transformed at time t in a new set of curves that represents the deformed state Ω_t, as presented in Fig. 2.2. In the same figure, an arbitrary surface in three-dimensional Euclidean space $\mathbb{E}^3$ is considered. The mapping of Ω_0 into Ω_t is such that the correspondence of the points M_0 and M is assumed one to one. The reference and deformed surfaces are defined by $\mathbf{S} = \mathbf{S}(\Theta^\alpha)$ and $\mathbf{s} = \mathbf{s}(\Theta^\alpha, t)$, respectively, with $\mathbf{S}$ and $\mathbf{s} \in \mathbb{E}^3$, where Θ^α are the surface curvilinear coordinates. In the following, $\mathbf{s}$ is supposed to be single-valued and sufficiently differentiable with respect to both arguments Θ^α as many times as required.

In order to handle with surfaces, two important pieces of data associated with any surface are recalled: the *first* and *second fundamental forms of surface.* Let M be a point on the surface whose coordinates are Θ^α and Q be a neighboring point of the surface with coordinates $\Theta^\alpha + d\Theta^\alpha$. Defining ds as the elementary distance between M and Q, the first fundamental form can be expressed by the quadratic form

$$(ds)^2 = g_{\alpha\beta}\, d\Theta^\alpha d\Theta^\beta. \tag{2.1}$$

where the elements $g_{\alpha\beta} = \mathbf{g}_\alpha \cdot \mathbf{g}_\beta$ are the covariant components of the surface metric tensor $\mathbf{g} = g_{\alpha\beta}\, \mathbf{g}^\alpha \otimes \mathbf{g}^\beta$. This symmetric and positive-definite tensor can be expressed on covariant, $\mathbf{g}_\alpha$, or contravariant, $\mathbf{g}^\alpha$, basis where $\mathbf{g}_\beta \cdot \mathbf{g}^\alpha = \delta^\alpha_\beta$ and δ^α_β is the *Kronecker* symbol. The first fundamental form is an invariant of surface and encodes the intrinsic data about the surface without referring back to the ambient space where the surface lies.

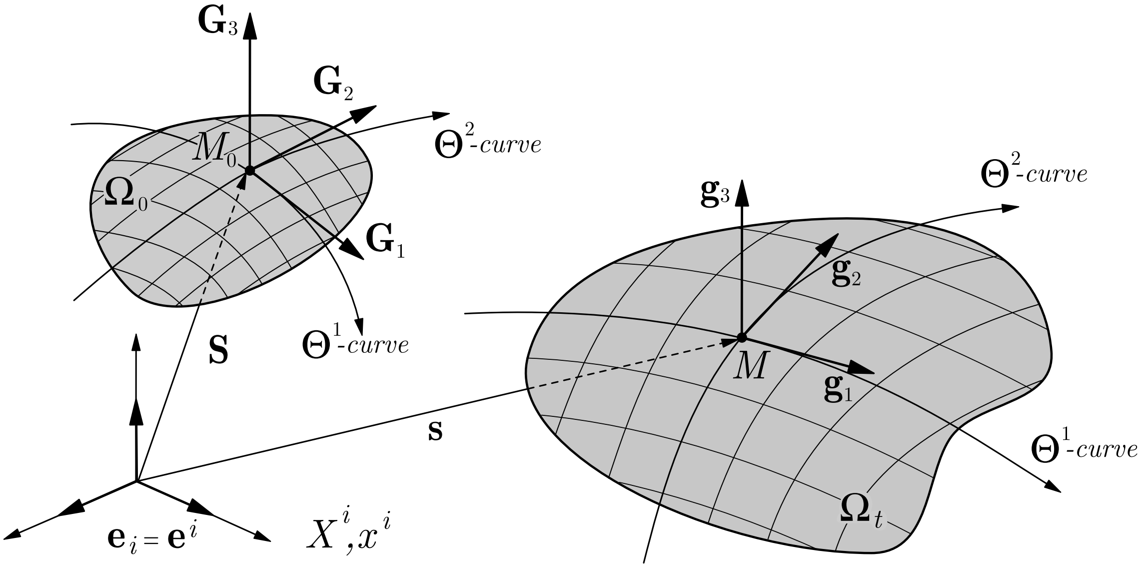

Figure 2.2: The surface basic geometric variable definition: $\mathbf{e}^i$ are the unit base vectors related with the orthogonal Cartesian coordinates X^i and x^i; $\mathbf{G}_i$ and $\mathbf{g}_i$ are the covariant basis related with M_0 and M respectively.

The second fundamental form, on the other hand, is a surface invariant that encodes the information about how the surface is curved in the embedding space. From the analysis of the differential geometry, it follows that the covariant components of surface curvature tensor $\mathbf{b} = b_{\alpha\beta}\, \mathbf{g}^{\alpha} \otimes \mathbf{g}^{\beta}$, associated with the second fundamental, are given by

$$b_{\alpha\beta} = \frac{\partial \mathbf{g}_{\alpha}}{\partial \Theta^{\beta}} \cdot \mathbf{g}_3 \tag{2.2}$$

where

$$\mathbf{g}_3 = \frac{\mathbf{g}_1 \times \mathbf{g}_2}{\|\mathbf{g}_1 \times \mathbf{g}_2\|} = \mathbf{g}^3. \tag{2.3}$$

The interest is focused in the two principal curvatures κ_n at a given point M in the membrane surface. Considering now the eigenvalue problem in each point M

$$(\mathbf{b} - \kappa_n \mathbf{g})\, \mathbf{v} = \mathbf{0} \tag{2.4}$$

where the surface *shape operator* is given by $\mathbf{b}\mathbf{g}^{-1}$. Since the shape operator is self-adjoint on the tangent plane at the surface in M, the corresponding eigenvalues κ_I, κ_{II} are called the principal curvatures at M, and $\mathbf{v}_I$ and $\mathbf{v}_{II}$ are the principal curvature directions at M. Recalling the definition of the *Gaussian-curvature*, $\mathcal{K}$, and *mean-curvature*, $\mathcal{H}$, it follows that

$$\mathcal{K} = \det(\mathbf{b}\mathbf{g}^{-1}) = \kappa_I \kappa_{II} \tag{2.5}$$

and

$$\mathcal{H} = -\frac{1}{2}\,\mathrm{trace}(\mathbf{b}\mathbf{g}^{-1}) = \frac{1}{2}(\kappa_I + \kappa_{II}). \tag{2.6}$$

As consequence, the maximal and minimal curvatures resulting from the quadratic form $\kappa^2 - 2\mathcal{H}\kappa - \mathcal{K} = 0$ associated with the surface shape operator are given by

$$\kappa_I, \kappa_{II} = \mathcal{H} \pm \sqrt{\mathcal{H}^2 - \mathcal{K}}. \tag{2.7}$$

For comprehensive exposition of other definitions and concepts on differential geometry with applications, see for example Carmo (1976), Ciarlet (2005) and Toponogov (2006).

Finally, a MatLab routine (see Appendix A) was developed to perform a two-dimensional numerical differentiation scheme over the Θ^α coordinates for each time t. Thus, the terms of Eqs. (2.1) to (2.7) are computed and principal curvatures can be determined at each membrane point. Given that 3D-DIC is able to capture any 3D contour and the curvature tensor is calculated for each surface point, the presented scheme of curvature calculation is not restricted to shape characteristics like axisymmetry.

2.2.4 Meridional and circumferential stress determination

Considering now the axisymmetric bulge test, the equilibrium equations can also be derived directly by balancing the forces of an element of the deformed shape. Employing the primary assertions of the membrane theory, every material point of the membrane in both reference and deformed configuration is in a plane stress state (Green and Adkins, 1970). In Fig. 2.3(a) the initially flat thin planar circular sheet of radius a and with an uniform thickness h_0 is presented. For convenience, to describe the strain field, cylindrical coordinates $(R, \Phi, Z = 0)$ define the position of a material particle M_0 in the middle surface of the stress-free membrane in the reference configuration. Let the pressure p acts in the bottom surface of specimen, the membrane experiences a deformation. The point M_0 moves to the position M, and the deformed configuration is defined by the coordinates $r(R, \Phi)$, $\phi(R, \Phi)$ and $z(R, \Phi)$. Note that in either configuration, the profile of the membrane has no circumferential dependence. Under the assumption of material isotropy, the principal directions of both stretch and stress at each material particle are known *ab initio* to be the meridional and circumferential directions to the membrane surface. From this point forward, these directions will be denoted by the subscripts m and c respectively, as shown in Fig. 2.3(b).

Assuming quasistatic motion, the equations of equilibrium, at point M, for a thin axisymmetric isotropic membrane, as adopted by Hill (1950), can be expressed as

$$\sigma_m = \frac{p}{2h\ \kappa_c} \tag{2.8}$$

$$\sigma_c = \frac{p}{2h\ \kappa_c}\left(2 - \frac{\kappa_m}{\kappa_c}\right), \tag{2.9}$$

where p is the time-dependent normal pressure acting uniformly $(dp/dR = 0)$ and h the current thickness. The stress components are expressed in Eqs. (3.2) and (3.3) directly in terms of pressure and the current bulge geometry. As mentioned in Wineman (1976) and Humphrey (1998) a remarkable consequence of membrane theory is that it admits equilibrium solutions without explicitly requiring a constitutive equation, since the equilibrium equations are derived directly by balancing forces of an element of the deformed shape. As consequence they are valid for all classes of in-plane isotropic materials. As pointed out by

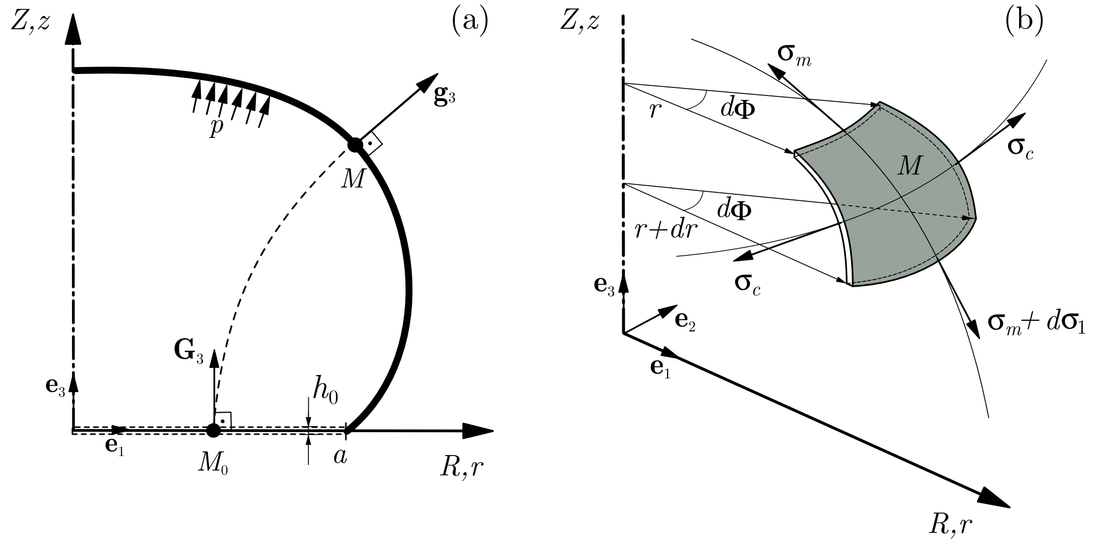

Figure 2.3: (a) The axisymmetric bulge test scheme. (b) A deformed differential element and principal directions of stresses.

Hsu *et al.* (1995), however, principal curvatures κ_m, κ_c can be experimentally computed, thus Eqs. (3.2) and (3.3) are very useful for exploiting axisymmetric bulge test data.

2.3 Benchmark inflation test using a Mooney membrane

2.3.1 Experimental data emulation

In order to demonstrate some quantitative predictions of the presented method to obtain the membrane stress field presented in Sec. 2.2 the finite element method (FEM) was used to emulate experimental data similar to that obtained by 3D-DIC. The aim here is to use a regular finite element mesh that represents in the same way the grid used by 3D-DIC to describe the surface geometry. Therefore, these virtual data are free from the usual experimental problems of the real 3D-DIC data, like missing and outlying values.

Using the Mooney hyperelastic model Mooney (1940) the FEM outputs nodal coordinates and displacements are used as data. Thus, an uniform mesh with an element edge length of 2 mm, was used to discretize a square zone inscribed into the circular geometry to obtain a good spatial resolution for the curvatures calculation. The Mooney model was arbitrarily chosen and any other constitutive model could have been used as well. For details of Mooney model and basic equations on large deformations see Meunier *et al.* (2008).

2.3.2 The finite element model description

Numerical simulations were performed using the finite element code ABAQUS. Assuming an incompressible isotropic hyperelastic material behavior, the Mooney (1940) strain-

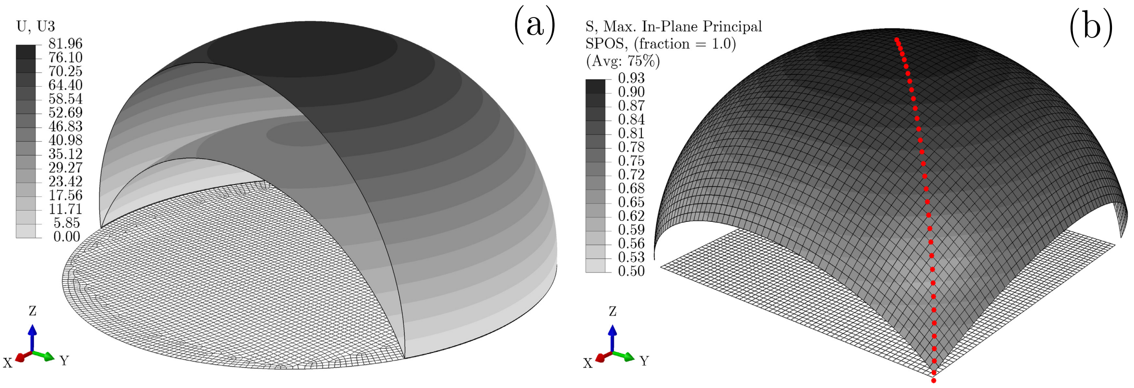

Figure 2.4: Numerical inflation of Mooney behavior membrane. (a) z direction displacements (in mm) for pressure loads of 7.5 kPa and 15 kPa. Mesh are represented only in reference configuration and the two pressure steps are superposed; (b) Principal in-plane stress (in MPa) are plotted onto deformed shape and only the regular square zone is represented. Solid circles represent the meridional path.

energy function $\mathcal{W}_{\mathrm{M}}$ can be written as

$$\mathcal{W}_{\mathrm{M}}\left(I_1, I_2\right) = C_{10}\left(I_1 - 3\right) + C_{01}\left(I_2 - 3\right) \tag{2.10}$$

where C_{10} and C_{01} are material parameters. I_1 and I_2 are the first and second strain invariants of the right Cauchy-Green deformation tensor $\mathbf{C}$ ($\mathbf{C} = \mathbf{F}^T\mathbf{F}$, where $\mathbf{F}$ is the deformation gradient tensor). Due to its mathematical simplicity as well as its prediction accuracy in the range of moderately-large strains, this hyperelastic model have been widely employed in the description of the behavior of rubber-like materials.

The model geometry consists in a thin circular plate, of initial radius $R(a) = 90$ mm with $h_0 = 2$ mm of thickness. The circular plate is simply supported and subjected to an uniform inflating pressure acting perpendicular to the current configuration. The Mooney hyperelastic model parameters are those given in Meunier *et al.* (2008), where $C_{10} = 0.14$ MPa and $C_{01} = 0.024$ MPa for the RTV141 silicone rubber cured at 70 °C during 150 min. The finite deformation problem was modeled with the S4R shell elements (4-node doubly curved general-purpose shell, reduced integration with hourglass control, finite membrane strains) with eleven Gauss integration points through the thickness. Fig. 2.4(a) depicts a sliced sequence of deformed configurations for two pressure loads of 7.5 kPa and 15 kPa, respectively.

2.3.3 Curvature Method: application to the virtual data

Using the FEM deformed nodal coordinates output, the principal curvatures κ_m, κ_c are computed over all surface, as described in Sec. 2.2.3, by means of the MatLab implemented post-treatment routine, presented in Appendix A. To illustrate the curvature evaluation, the isovalues are presented in Fig. 2.5 for $p = 15$ kPa. This figure shows clearly the bulge axisymmetry, as curvatures iso-curves are perfectly concentric. Stress components can thus be evaluated from Eqs. (3.2) and (3.3). Further, since boundary conditions are

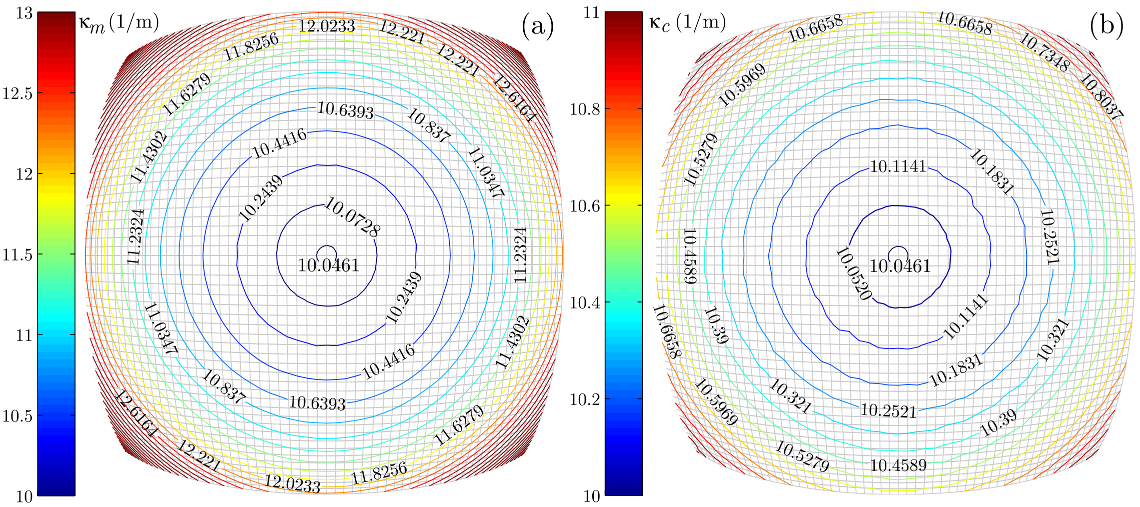

Figure 2.5: Curvatures of Mooney behavior membrane at $p = 15\,\text{kPa}$. (a) Meridional and (b) circumferential isovalues evaluated using the FEM deformed nodal coordinates output as data.

perfectly balanced over the circumferential perimeter at $R(a)$, a perfectly spherical cap is obtained, i.e., surrounding the pole a cap of *umbilical points* κ_m=$\kappa_c \neq 0$ can be easily identified. At such points, both principal curvatures are equal every tangent vector is a principal direction.

The output fields principal stretches (λ_m,λ_c), principal curvatures (κ_m,κ_c) and principal stresses (σ_m,σ_c) are plotted for a single meridional path in Fig. 2.6(a), (b) and (c), respectively. Afterward, the principal stresses (σ_m,σ_c) computed using Eqs. (3.2) and (3.3) were compared with the Mooney membrane FEM outputs. It can be seen that the results fit very well in Fig. 2.6(c). The relative differences between both stress components using the presented method and FEM are plotted in Fig. 2.6(d) for 7.5 kPa and 15 kPa. Errors tend to be less than 2 % for both stress directions for maximum pressure level of 15 kPa. On the other hand, errors increase for lower pressure levels. This notice seems to be natural knowing that principal curvatures vanish when the surface becomes flat. However, the principal explanation in disagreement of the stress results comes from the fact that, no matter how thin, all structures are three-dimensional and possess some bending stiffness. It is important bearing in mind that the membrane theory is an approximation. Fig. 2.7 shows the variation of FEM principal stresses over the membrane thickness h in the pole ($R = 0$) and in the border ($R = 0.95a$), for an initial ratio radius/thickness of $a/h = 45$. Note that, bending effects are more pronounced nearest to the border ($R \to a$) in both configurations. This fact justifies the form of curves presented in Fig. 2.6(d). The other important observation from Fig. 2.7 is that the bending influence can increase for low pressure levels. A similar result was found by Kyriacou *et al.* (1997) for an inverse finite element characterization using a bulge test sample with $a/h \approx 30$ stretched at the pole of about 1.3. Authors notice that the error in the estimated parameter increased with an decrease in the pressure at which the data were generated. Thus, depending of sample material and geometry, the amount of bending could be non-negligible for small strain

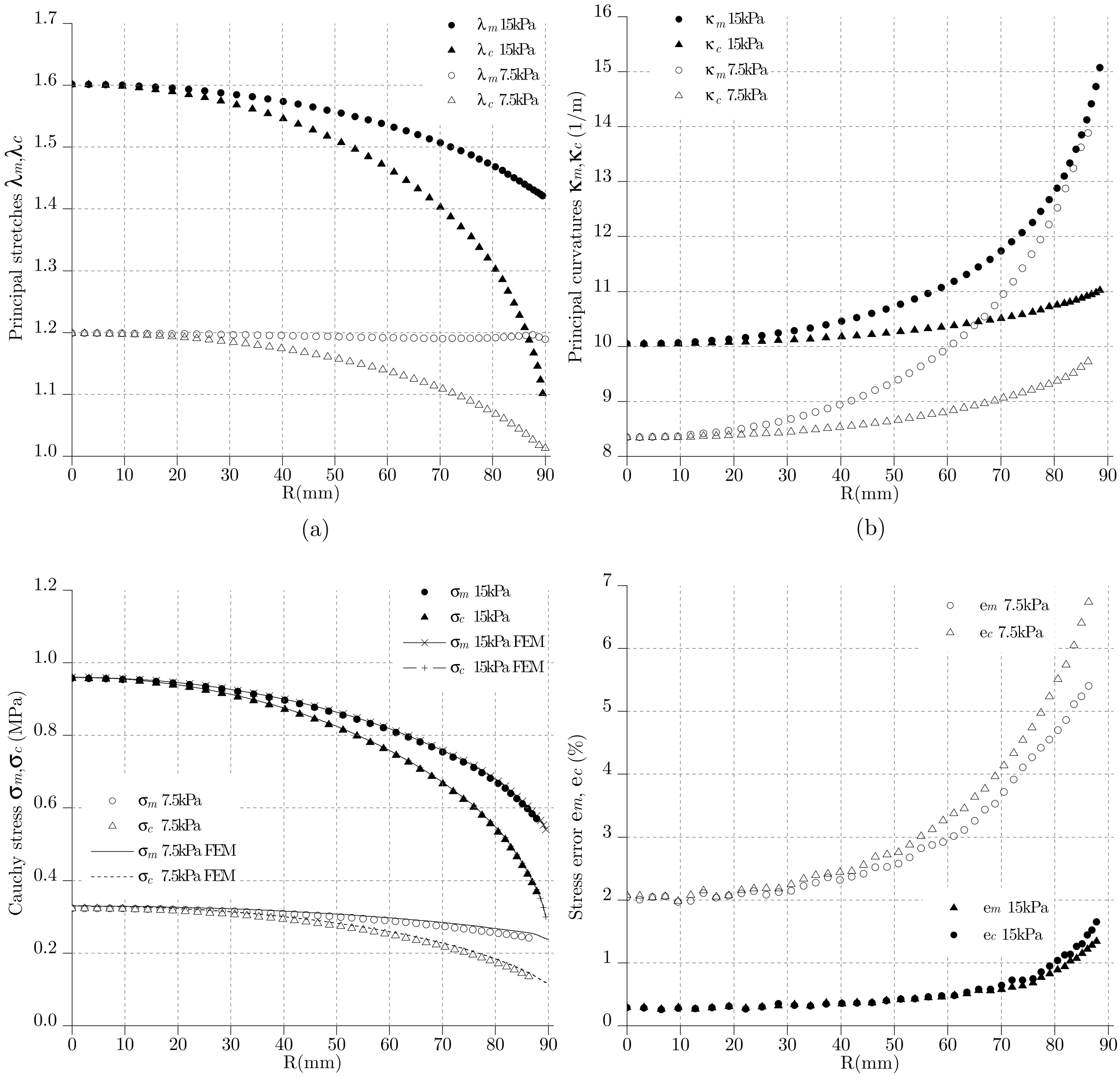

(a) (b)

(c) (d)

Figure 2.6: Two deformed configurations 7.5 kPa and 15 kPa pressure levels for the incompressible Mooney ($C_{10} = 0.14$ MPa and $C_{01} = 0.024$ MPa) membrane. (a) Principal stretches (λ_m,λ_c); (b) Principal curvatures (κ_m,κ_c); (c) Cauchy stress (σ_m,σ_c) confronted with the finite element results (FEM); (d) Errors with respect to principal stresses in both deformed configurations.

levels.

A last important remark arises from the fact that curvatures estimated for real 3D-DIC data are very sensitive to experimental noise since estimates of partial derivatives of second order are necessary. Gaussian noise was then introduced into the X^i coordinates of FEM data results to simulate potential experimental errors. Applying our method to these noisy data leads to very poor estimation of both circumferential and meridional stresses, as shown in Fig. 2.8. Smoothing can be used to reduce experimental additive noise and small-scale information while keeping the most important imprints of data set. For these cases, a

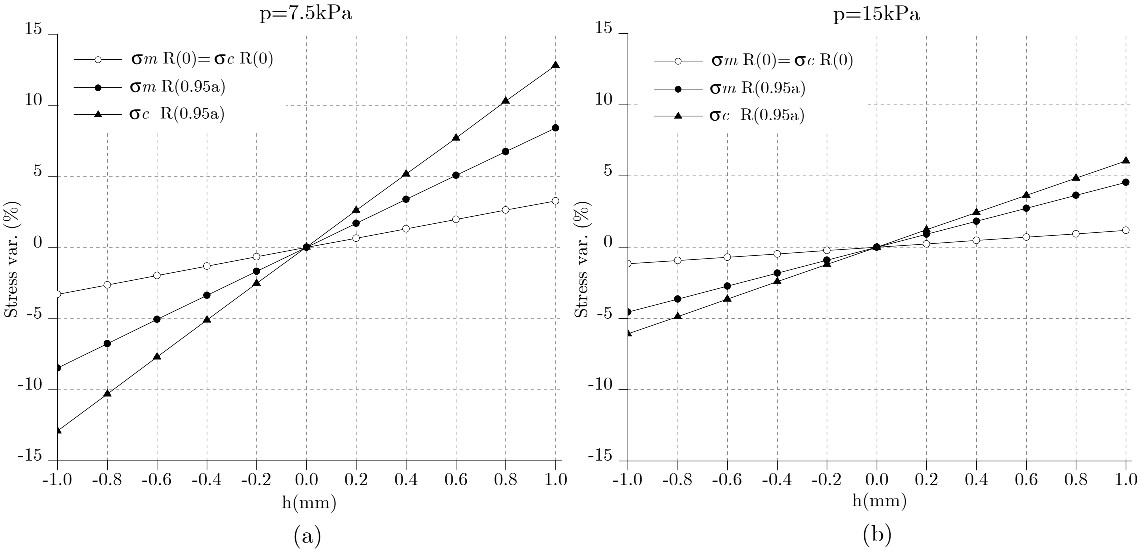

(a) (b)

Figure 2.7: Bending stiffness effects in both deformed configurations (7.5 kPa and 15 kPa pressure levels) for the numerical benchmark. Principal stresses variation (i.e. $\sigma_m/\sigma_{m(mean)}$ analogous for σ_c) over the element thickness (h) at the sample pole ($R(0) = 0mm$) and border ($R(a) = 90mm$).

discretized smoothing spline algorithm proposed by Garcia (2010) was implemented. The weighted robust version of the algorithm was used to deal with occurrences of missing and outlying values of gridded data. The perturbed data were input into the post-treatment routines. Curvatures and stresses were recalculated and Fig. 2.8 presents the results. Smoothing allows obtaining estimated values of the stresses from the noisy data very close to those of the original FEM data.

This numerical study validates the developed post-treatment routines, as the stress results are quite similar to FEM results by considering the hypotheses presented.

2.4 Application of the method to experimental bulge test of a silicone elastomer

2.4.1 Experimental bulge test

The objective of this section is to experimentally validate the proposed method to determine curvatures and stresses on bulge test of a silicone elastomer. Experimental difficulties are pointed out and results are confronted with a finite element model. The chosen silicone rubber is an unfilled formulation produced by Rhodia (RTV 141). Specimens were produced using the processing described in Meunier *et al.* (2008), following the processing route: (i) mixing the two liquid components, i.e., the uncured silicone and the curing agent, with a 10/1 ratio, (ii) putting the uncured mixture under vacuum for 30 min in order to eliminate undesirable entrapped bubbles, (iii) injecting the liquid mixture in sheet mold and (iv) putting mold inside an oven at 70 ^oC for 4 hours to cure the silicone. Comparing with Meunier *et al.* (2008), the cure was augmented in order to increase the

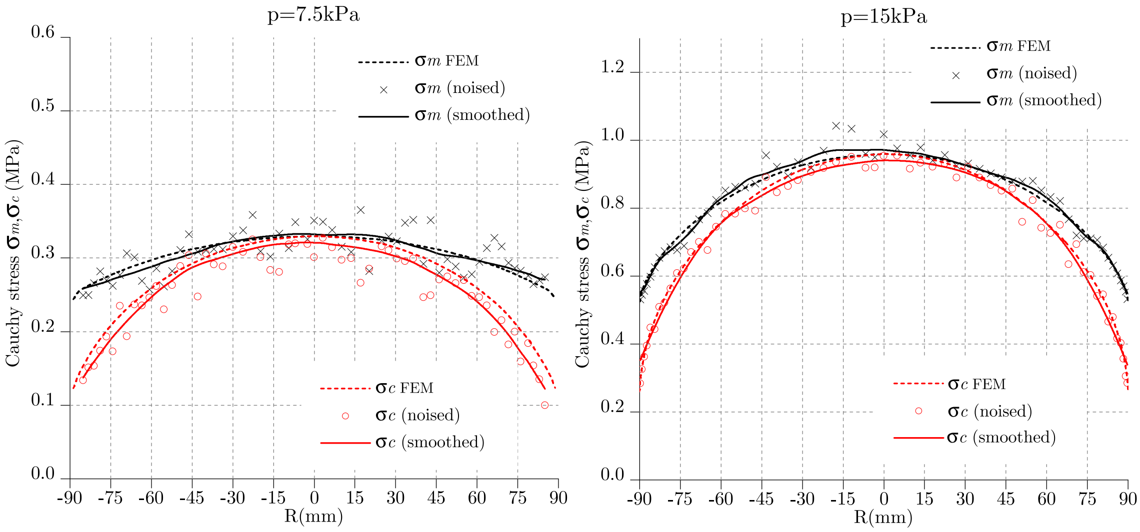

(a) (b)

Figure 2.8: Principal stress (σ_m,σ_c) results. Original finite element output (FEM), calculated using the artificially noised data (noised) and calculated using the smoothed data (smoothed).

tear resistance of the material. This permits to largely swell the membranes. Using the RTV141 silicone, experimental bulge tests were carried out to determine a non-uniform stress strain state over the membrane surface.

Bulge test setup

The disk specimen dimensions are the same as in Sec. 2.3 (initial radius $R(a) = 90\,\text{mm}$ with $h_0 = 2\,\text{mm}$ of thickness) constrained between two clamping flanges. In this test machine, the principle consists of a pressurized air line connected to the bottom circumferential clamp. Given the small pressures used during the experiments, a regulator is required to reduce the line pressure to a maximum of 30 kPa. To decrease the pressure, an unloading valve is opened to create a leak. The internal pressure is measured by a Foxboro $0 - 500\,\text{mbar}$ pressure sensor. A picture of the experimental setup is shown in Fig. 2.9(a).

3D-DIC setup and experimental difficulties

The out-of-plane displacement measurement is needed, therefore the Dantec Q-400 commercial 3D-DIC system was used to acquire and correlate the full-field bubble shape information. Since a large out-plane displacement is experienced by the silicone sample, a good focal distance is absolutely necessary. The biplane CCD cameras, using 20 mm focal length lenses opened at $f/16$, are focused in manner to maximize the acquired area to the pole up to the border. However, it is important that the object surface shows enough structure to allow the algorithms to correlate identical points from both cameras. Note that, using only two cameras, the information near to the border will be lost if the membrane experiences large displacements creating a self-shadow effect. Thus a R_{max} defines the limit of the correlation zone, i.e., the maximum distance from the membrane center which is seen by the two cameras. A third camera should be added in this case to be able to correlate along all a meridional direction, see Orteu *et al.* (2010) for a multiple-camera instrumentation example.

A high spatial resolution is needed to permit an accurate measurement of curvatures. The spatial resolution achieved in practice depends on a number of factors, including but not limited to camera resolution, lens optical quality, and marker size and quality. Facet size limits the spatial resolution as well, as the result of each evaluation grid point follows from the image correlation of the extended facet region. Thus increasing facet size causes smoothing of the results and decreasing so the spatial resolution. In order to have independent data points the facets of neighboring data points should not overlap. The full camera resolution (C_{res}) is used (2048 pixels × 2048 pixels) with an evaluation grid size $G_s = 12$ pixels and a facet size $f_{size} = 21$ pixels, resulting in a spatial resolution of $S_r = 1.45$ mm over the membrane surface.

Fig. 2.9(b) presents an example of reconstructed surface. Note that in some small regions on surface, missing data occur due to some correlation abnormalities, normally associated with locally irregular pattern.

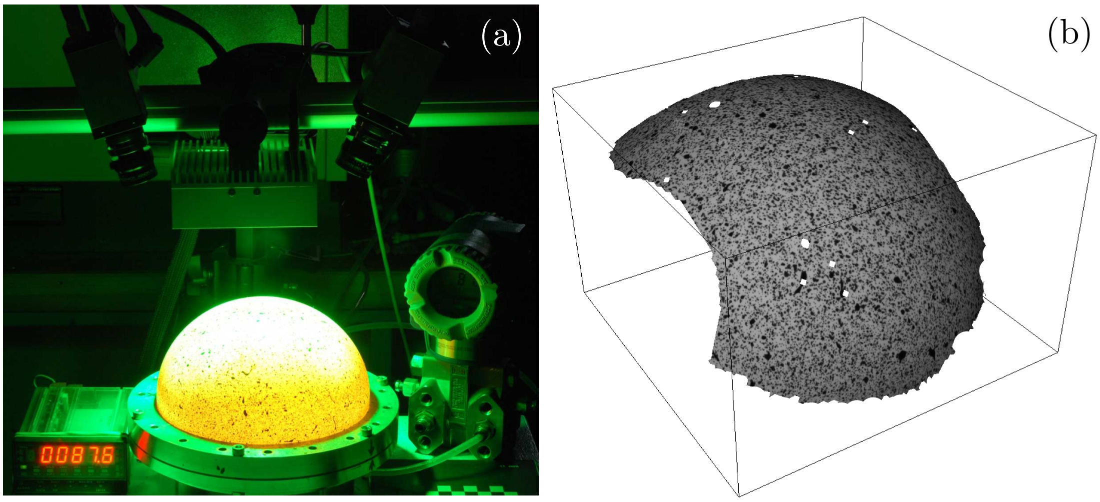

Figure 2.9: (a) The bulge test experimental setup using 3D-DIC technique; (b) Reconstructed RTV141 membrane surface.

Test Results

Cyclic inflations were performed, applying $p = 30$ kPa several times, to pre-stretch the specimen in order to accommodate the material. This is due to the fact that silicone rubber can exhibit considerable stress softening phenomenon for different loading cases (Machado *et al.*, 2010). After the recovery time of 1 h and starting from an initially flat surface, inflations were performed from 8 kPa to a maximum pressure of 27.1 kPa. These inflations yielded principal stretches at the pole of about 1.10 and 1.36 respectively. Fig. 2.10 shows the principal curvature κ_m plotted onto 3D-DIC reconstructed surface.

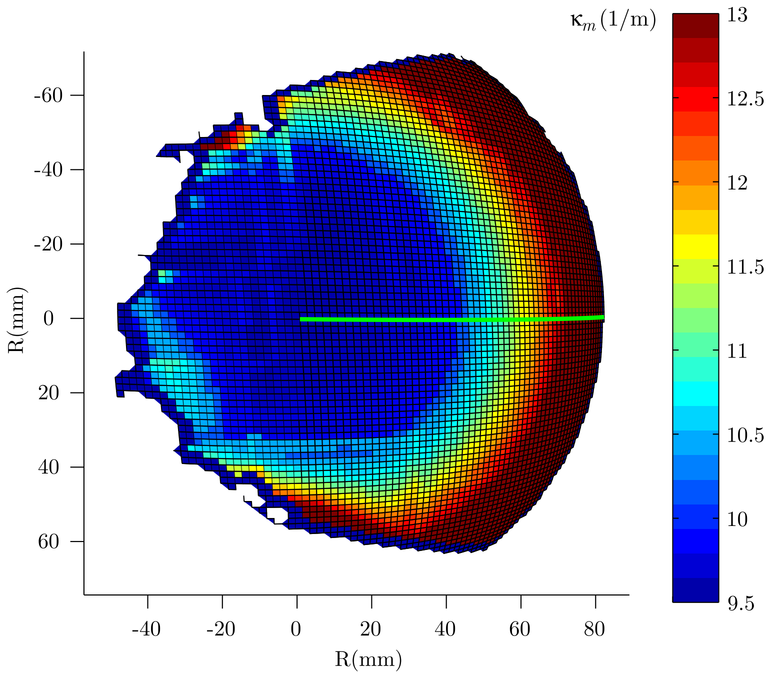

Figure 2.10: Principal curvature κ_m plotted onto 3D-DIC reconstructed surface. Solid line represents the meridional path used in Fig. 2.11

This bulge test can be considered as axisymmetric. Plots of the deformed membrane, over the meridional path, for each of the two inflation states can be found in Fig. 2.11. The values of z direction displacements (in mm) and principal stretches (λ_m,λ_c) were obtained direct from 3D-DIC system. Principal curvatures (κ_m,κ_c) and principal stresses (σ_m,σ_c) were computed using Eqs. (2.7), (3.2) and (3.3) respectively.

The experimental fields are plotted in Fig. 2.11. For each of the two inflation states all material points, save the pole ($R(0) = 0$ mm) and the clamped boundary ($R(a) = 90$ mm), experience both axial and meridional displacements as a result of their respective finite deformations. The plots of the principal stretches (λ_m,λ_c) in Fig. 2.11(c) show that each inflation state involves a heterogeneous strain state, i.e., equibiaxial stretch at the pole, planar stretching at $R(a)$. As expected, the circumferential stretch λ_c tends to one towards the clamped boundary, i.e., when $R \rightarrow R(a)$. With respect to principal curvature distributions (κ_m, κ_c), note that equibiaxial membrane deformations near the membrane pole are associated with an approximately spherical geometry, i.e., $\kappa_m \approx \kappa_c$. The non perfect equality may be explained by the fact that the umbilical point may not lie exactly on the z direction axis. This subtile difference can increase for high deformed states. Stress state can be assumed to be approximately balanced-biaxial at the pole, following by the circumferential stress σ_c which steadily decreases when $R \rightarrow R(a)$.

2.4.2 Material characterization and numerical simulation

In the previous section, stress and strain fields have been obtained by the presented method which does not require any constitutive equation and parameter determination. The aim

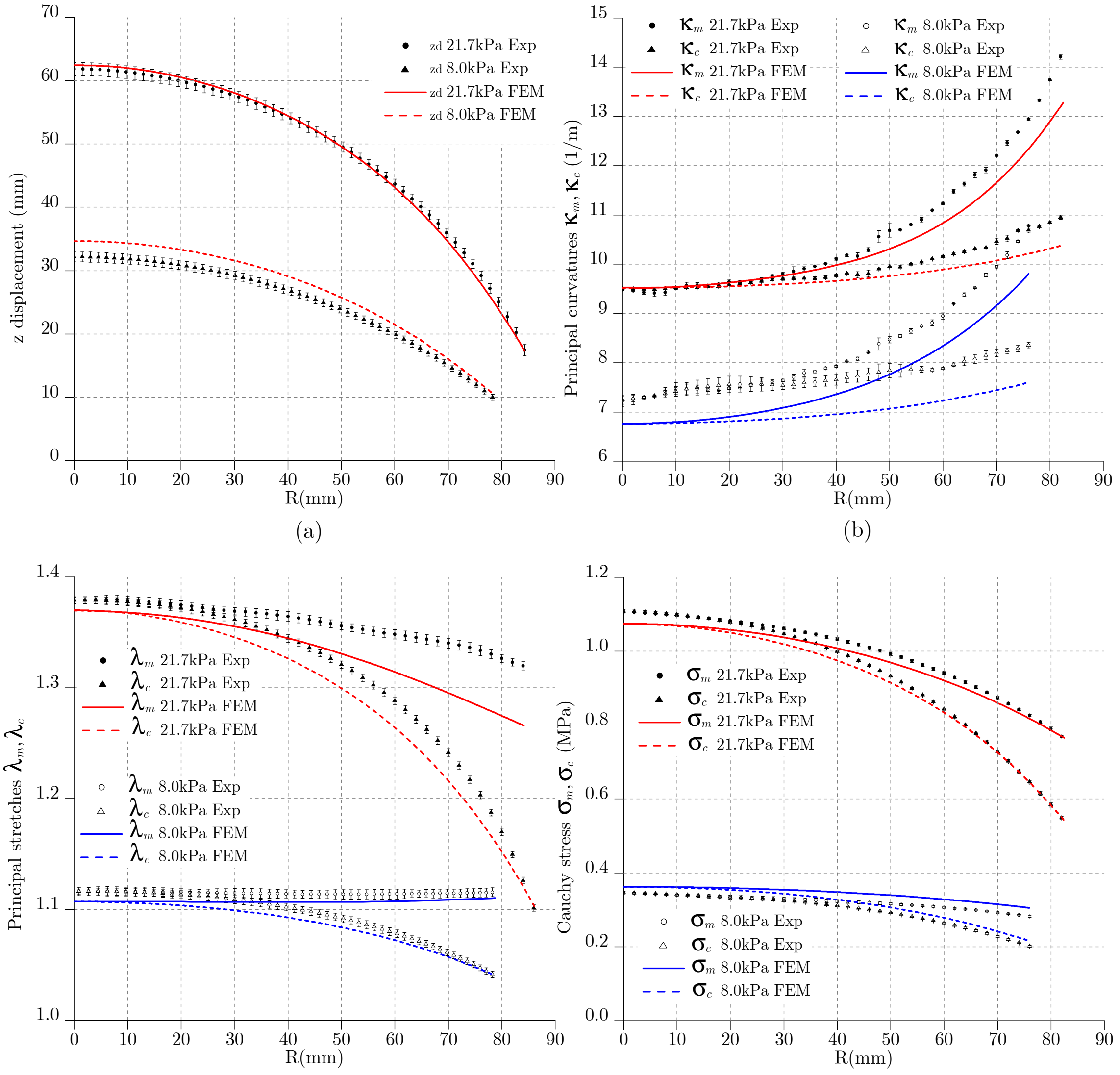

(a) (b) (c) (d)

Figure 2.11: Distributions of experimental (Exp) and numerical (FEM) fields: (a) z direction displacements; (b) principal curvatures (κ_m,κ_c); (c) principal stretches (λ_m,λ_c); (d) principal stresses (σ_m,σ_c); corresponding to 8 kPa and 21.7 kPa inflation states.

of this section is to compare these results with an usual analysis of such as bulge test. This analysis is done by means of a numerical simulation implying a modeling of the mechanical behavior of the unfilled silicone rubber RTV141. It is known that different modes of deformation are required to obtain the constitutive equation and the parameters that define the stress-strain relationship accurately. The tests used in this investigation are cyclic uniaxial and equibiaxial tension, completely independent, i.e., they were performed in parallel from the bulge test described in the last section.

Uniaxial tensile test and equibiaxial test are performed at room temperature at $\dot{\lambda} = 1.25 \times 10^{-2}\,\mathrm{s}^{-1}$. The material presents a weak hysteresis and a very little strain rate dependency (Meunier *et al.*, 2008). Nevertheless, a stress softening phenomenon, called

Mullins effect (Mullins, 1969) appears, contrary to Meunier *et al.* (2008) using a smaller curing time. Mullins effect strongly depends on the maximum previous deformation. To measure the influence of the previous maximum deformation, increasing cyclic uniaxial tests were performed at $\lambda = 1.75$ and $\lambda = 1.95$. Fig. 2.12(a) highlights that for moderate deformations $\lambda < 1.40$, the second loading curves are nearly the same whatever is the previous maximum strain. This means that increasing the maximum strain has only a slight effect on the behavior at moderate deformations. Therefore, for the range of deformation, a hyperelastic constitutive equation is sufficiently accurate to model the mechanical behavior. The neo-Hookean constitutive equation (Treloar, 1943) is chosen to describe mild deformations:

$$\mathcal{W}_{\mathrm{N}}\left(I_1\right) = C_{10}\left(I_1 - 3\right). \tag{2.11}$$

The material parameter is fitted on second loading curves for uniaxial and equibiaxial tests, $C_{10} = 0.335\,\mathrm{MPa}$ is obtained. The results are presented in Fig. 2.12(a) and (b). This shows that the model predicts satisfactorily the two loading stress for $\lambda < 1.40$.

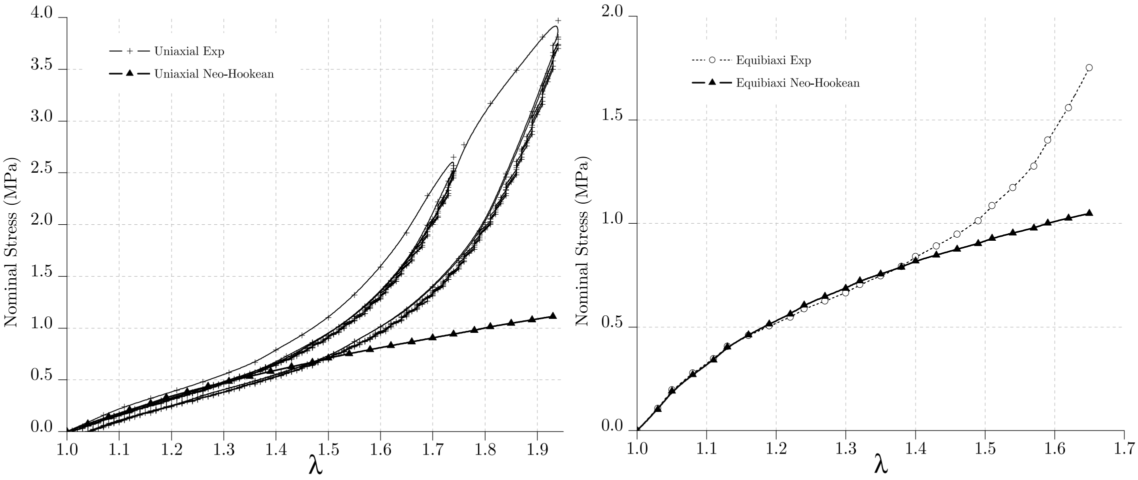

(a) (b)

Figure 2.12: Experimental data and the hyperelastic fitting using the neo-Hookean hyperelastic model: (a) Uniaxial and (b) equibiaxial tensile tests at $\dot{\lambda} = 1.25 \times 10^{-2}\,\mathrm{s}^{-1}$.

2.4.3 Experimental and numerical comparison of bulge test results

Results of FEM using the neo-Hookean model are superposed with the experimental fields (displacement, principal curvatures, principal stretches and principal stresses) in Fig. 2.11. All numerical predictions clearly follow the trends calculated from the presented method to obtain the principal curvatures applied to the experimental data. For the z displacement field (Fig. 2.11(a)) a pronounced difference, for the lower pressure value, is observed. Consequently the curvatures evaluation (Fig. 2.11(b)) for this same load state is obviously affected. Nevertheless, errors in curvatures determination decreased with an increase in the strain level as observed in the benchmark of Section 2.3. Considering the principal stresses plots, a good agreement is observed in spite of the hyperelastic constitutive equation simplicity.

It is important to keep in mind the simplicity of the neo-Hookean model, the simple procedure used for material parameter identification and the precaution taken to accommodate the material before testing. An interesting characterization method for rubber is proposed in Guélon *et al.* (2009), performing only one heterogeneous mechanical test, measuring the displacement and strain fields using DIC and applying an inverse method. They obtain a large set of heterogenous states, represented in the $I_1 \times I_2$ invariants plane, between uniaxial tensile and planar shear tensile paths. Fig. 2.13 illustrates the strain states, in the $I_1 \times I_2$ invariants plane, for the classical three homogeneous tests used in material parameter identification. In the same figure, the gray zone represents all the heterogenous states covered in the bulge test, with the advantage of knowledge about the stress field. For the presented material test, the distribution of loading cases in this zone are limited to R_{max} achieved during the correlation step. This zone is represented by a circular hatch pattern in Fig. 2.13. As aforementioned, the R_{max} depends of the membrane displacements levels and camera dispositions in order to acquire the information over the border, i.e., the zone dominated by planar shear tensile state.

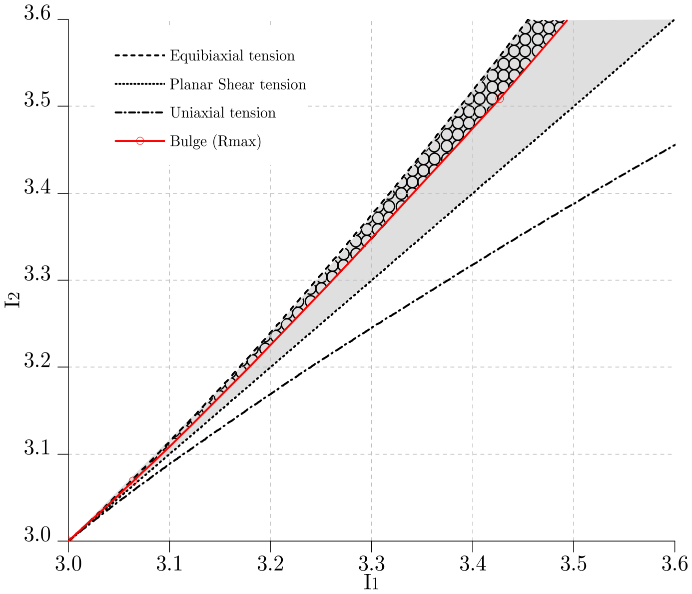

Figure 2.13: Loading case in $I_1 \times I_2$ plane. The gray zone represents all heterogeneous deformations states covered by the bulge test. The Bulge(R_{max}) curve refers to the heterogeneous path at R_{max} point. The circular hatch pattern represents the distribution of loading cases for the presented material test.

2.5 Conclusion

The aim of the present work was to propose a method which enriches greatly the analysis of usual bulge tests by using the 3D-DIC technique. Firstly, this paper presented a general method to determine surface curvature tensors from 3D-DIC data. This requires no assumptions regarding axisymmetry or other shape characteristics of the membrane surface. Secondly, the determination of the curvature tensor fields allowed checking the axisymmetry of the bulge test, which has to be obtained for planar-isotropic material and perfect boundary conditions. Once this axisymmetry was proved, the proposed method permitted to determine the stress-strain fields associated with the membrane inflation problem without any constitutive equation. The method was applied in this paper both on virtual data generated by numerically simulating the bulge test and on real data of one experiment performed on a silicon elastomer. In this last case, experimental difficulties were pointed out, particularly the difficulty to obtain the information near to the border for the chosen material. These two examples showed that bulge test can be used as one very rich heterogeneous mechanical test which allows obtaining valuable information for testing different types of materials for a wide potential range of stress-strain states ranging from equibiaxial to planar tensile stress state.

CHAPTER

3

Induced anisotropy by the Mullins effect in filled silicone rubber

G. Machado, G. Chagnon, D. Favier

Submitted to Mechanics of Materials

This study is concerned with the experimental characterization of anisotropy induced by the Mullins effect in a particle-reinforced silicone rubber. Experimental data concerning the influence of type and direction of initial loading on the subsequent stress-softening are quite scarce. In this scope, a set of experimental tests were carried out on a filled silicone rubber. Uniaxial tensile test and bulge test were used to precondition the samples, i.e., to induce some primary stress-softening. In both cases, subsequent uniaxial tensile tests are conducted on preconditioned specimens. The first set of experiments consists of a homogeneous tensile path followed by tensile along different directions. It appears that the stress softening varies from a maximum in the same direction load to a minimum in the orthogonal direction, with respect to the first tensile load direction. Next, the bulge test is proposed as an original way to yield very different biaxial strain-histories for first loading path. The fact that the biaxiality ratio varies from the pole until the bulge border, permits to analyze second tensile load curves in a material that experienced a more complex first load path. These experimental data allow to discuss the most appropriate criteria to describe the strain-induced anisotropy phenomenon.

Contents

3.1 Introduction

Rubber-like materials exhibit a significant stress softening after a first loading. This phenomenon called Mullins effect has been observed in different paths of deformation during the last six decades. A detailed review for experimental references in different deformations states like uniaxial tension, uniaxial compression, hydrostatic tension, simple shear and equibiaxial tension is given in Diani *et al.* (2009).

In a first approach, the Mullins effect was analyzed under the isotropy hypothesis, which leads to numerous models in terms of pseudo elasticity (Ogden and Roxburgh, 1999; Dorfmann and Ogden, 2004), damage modeling (Chagnon *et al.*, 2004) and macromolecular approaches (Govindjee and Simo, 1991; Arruda and Boyce, 1993; Marckmann *et al.*, 2002). More references can be found in Diani *et al.* (2009). Nevertheless, this softening phenomenon is known to exhibit very strong directional dependency. This phenomenon was first exhibited in Mullins (1947), where the author alluded that the degree of softening for natural rubber was not the same for samples cut along and perpendicular to the direction of the previous preconditioning tensile stretch, and thus some anisotropic stress strain properties were developed. However, the corresponding experimental data have not been published.

More recently the evidence that stress softening is an inherently anisotropic phenomenon can be found for different rubber-like materials under different load cases. However, these investigations are almost restricted to a simple deformation history. Tension tests in two orthogonal directions have been the most usual method to point out the strain-induced anisotropy. Results can be seen in Laraba-Abbes *et al.* (2003) for a carbon-black filled natural rubber as material, Diani *et al.* (2006b) for filled black ethylene propylene diene (EPDM), Itskov *et al.* (2006) for carbon-black filled acrylate rubber (ACM), Hanson *et al.* (2005) for a silica-filled polydimethylsiloxane (PDMS) and Park and Hamed (2000) for different compositions of black filled styrene-butadiene rubber (SBR) and sulfur-cured carbon black filled natural rubber (NR). Simple shear experiments were performed by Muhr *et al.* (1999), they noticed that strain softening of polysiloxane polymer investigated is smaller in directions orthogonal to the strain cycle causing the softening. Similarly under simple shear, Besdo *et al.* (2003) showed that a prior loading, generated by a cyclic one-side shear, lead to a material anisotropy verified during a symmetric loading, i.e., both-sided shear. Pawelski (2001) carried out two tests, first, a homogeneous plane-strain compression using a cubic sample of an elastomeric material (VLGQ-rubber) rotated and rotated back by 90° with respect to the first preloaded configuration. Here a special procedure was required to correct the original measurements since compression is accompanied by friction which spoils the experimental data. Second, for a polyurethane material, a modified biaxial tension with tensile tests on secondary specimens afterward, was used in a way to find an evidence for more complex memory behavior of the material.

Many physical interpretations for the Mullins effect have been proposed but few give an interpretation of the direction influence of the stress softening. Let us quote Papkov *et al.* (1975), who investigated the softening of siloxane rubbers. Their investigations suggest that the most probable softening mechanism is not the separation of the polymer molecules from the surface of the filler particles but the rearrangement of the chains on that surface as a result of slippage under stress. In addition, they considered that the transition of a given filled system to the quasi-stable state during the deformation may be accompanied not only by slippage of the chains on the surface of the particle but also by a certain rotation and irreversible displacement of the particle in the polymer matrix. This should lead to a corresponding change in the three-dimensional structure of the filled rubber and may be accompanied by the development of anisotropy of the mechanical properties. Hanson *et al.* (2005) provided another interpretation for the stress softening mechanism, based on the remove of chains entanglements that causes the stress to be lower on the second and subsequent strains, i.e., their mechanism conserves the number of network chains and only the entanglements density is reduced with respect to the original strain axis of the first load.

Some models aiming to describe the anisotropy of the stress softening are proposed in the literature (see for example, Diani *et al.*, 2004; Göktepe and Miehe, 2005; Shariff, 2006; Diani *et al.*, 2006b; Ehret and Itskov, 2009). All these models provide a solid theoretical basis for mathematical description of the stress softening, like an anisotropic phenomenon, in rubber-like materials. However, the predictive capabilities of models describing the anisotropic Mullins effect are mainly restricted to the uniaxial load case. Horgan *et al.* (2004) reported that the anisotropic model cannot be validated since suitable experimental data are not available. Pawelski (2001) advised that further experimental works are necessary before one can decide how complex a material constitutive equation for rubber-like material should be. Itskov *et al.* (2006) pointed out that additional experiments regarding other load cases are needed. This allows to study further the influence of loading cycles with complex deformation states on the appearance and evolution of the Mullins effect in the case of changing principal stretch directions.

Within this context, the aim of this work is to quantify clearly the induced anisotropy according to the applied strain history. The objective is to focus on the strain-induced anisotropy study by verifying the influence of loading cycles in distinct directions using two different pre-stretch methods to drive the primary stress-softening history. The paper is organized as follows. In Section 3.2 the experimental method and results are presented. First, uniaxial extension of a large plate was used to induce the primary deformation. Then, the influence of induced anisotropy was investigated for different directions by cutting different specimens from the original plate and comparing the second load tensile curves. Second, the bulge test was used to generate different biaxial deformation histories, and again cut specimens from the original plate are thus submitted to tensile tests. In Section 3.3 a study of generated anisotropy is realized by analyzing the second load curves of the different tests and comparing their strain histories. Finally, Section 4.5 contains some concluding remarks and outlines some future perspectives.

3.2 Experimental study and analysis

The induced anisotropy by stress softening was experimentally studied. For this purpose, samples were made of a filled silicone rubber called Rhodorsil RTV3428. Supplied as two liquid components, the uncured silicone and the curing agent, this liquid mixture is molded by injection to obtain a sheet with constant thickness (Meunier *et al.*, 2008).

The final samples are produced by a polyaddition, curing at 70 °C for 4 h in order to accelerate the curing process and assure a sufficient cross-linking density. This material exhibits a pronounced stress softening under different load cases, as reported in Machado *et al.* (2010). In the same work, the manufacture procedure of specimens without any pre-existent anisotropy and testing methods details using three-dimensional image correlation (3D-DIC) are also described. With the 3D-DIC technique, it is possible to determine the 3D contour and the in-plane strain fields of the object surface. This process is carried out by correlation of the images, taken by two cameras in the deformed state with their original reference images. Thus, uniaxial tensile test and bulge test were used to precondition the samples, i.e., to induce some primary stress-softening. In both cases, subsequent uniaxial tensile tests are conducted on preconditioned specimens. The first experiment consists in a homogeneous tensile path followed by tensile in different directions. After, the bulge test is used to yield a very different biaxial strain-histories as first load path.

3.2.1 Mullins anisotropy induced by uniaxial tensile pre-stretch

Two identical rectangular specimens ($l_0 = 100\,\text{mm}$, width $w_0 = 70\,\text{mm}$ and thickness $h_0 = 2\,\text{mm}$) were submitted to one cycle of stretch, at $\lambda = 2.50$ in uniaxial tension along a principal direction referred to 0°, using an elongation rate of $\dot{\lambda} = 5.0 \times 10^{-3}\ s^{-1}$. Note that RTV3428 behavior can be assumed independent of the rate of deformation (see Machado *et al.*, 2010). Then, a set of smaller specimens was cut from each of these preconditioned large samples along five different directions 0° (first loading direction), 15°, 30°, 45° and 90° (orthogonal direction). An illustration is presented in Fig. 3.1(a). All these cut specimens were submitted to the same pre-conditioning strain state and this was verified thanks to strain field measurements.

Fig. 3.1(b) presents the virgin material tensile cycle (*vir* curve) and second loading curves for the different directions specimens, both stretched until $\lambda = 2.5$ at $\dot{\lambda} = 1.6 \times 10^{-2}\ s^{-1}$. All subsamples unload curves are superposed with the virgin reference sample unload curve and, for a clean visualization, they are not presented. A very small residual elongation is observed. Thus the effect of permanent set in the cut samples can be considered as negligible, since they were cut after a recovery time of 1 h.

It clearly appears that all second load curves come back on the first loading curve at the same elongation (*RP*–point) which is the maximal elongation reached during the pre-stretch. However, the main difference is the shape of the second load curves, the amount of stress-softening can be relied to the angle between the first and second loading directions. Note that with the angle increasing, the shape of the second load curves tend toward the virgin material load curve (*vir*). The perpendicular direction (90°) is nearly superposed with the virgin curve. This evidence was noticed by Papkov *et al.* (1975) (for samples with an inferior filler ratio), Park and Hamed (2000), Hanson *et al.* (2005) and Diani *et al.* (2006b). On the other hand, in Papkov *et al.* (1975) (for samples with a superior filler ratio), Laraba-Abbes *et al.* (2003) and Itskov *et al.* (2006), perpendicular specimens have the same shape of the stress-strain virgin curve, but with a pronounced lower modulus. This fact may be attributed to the filler nature, and their mass and volume proportion in the polymeric matrix.

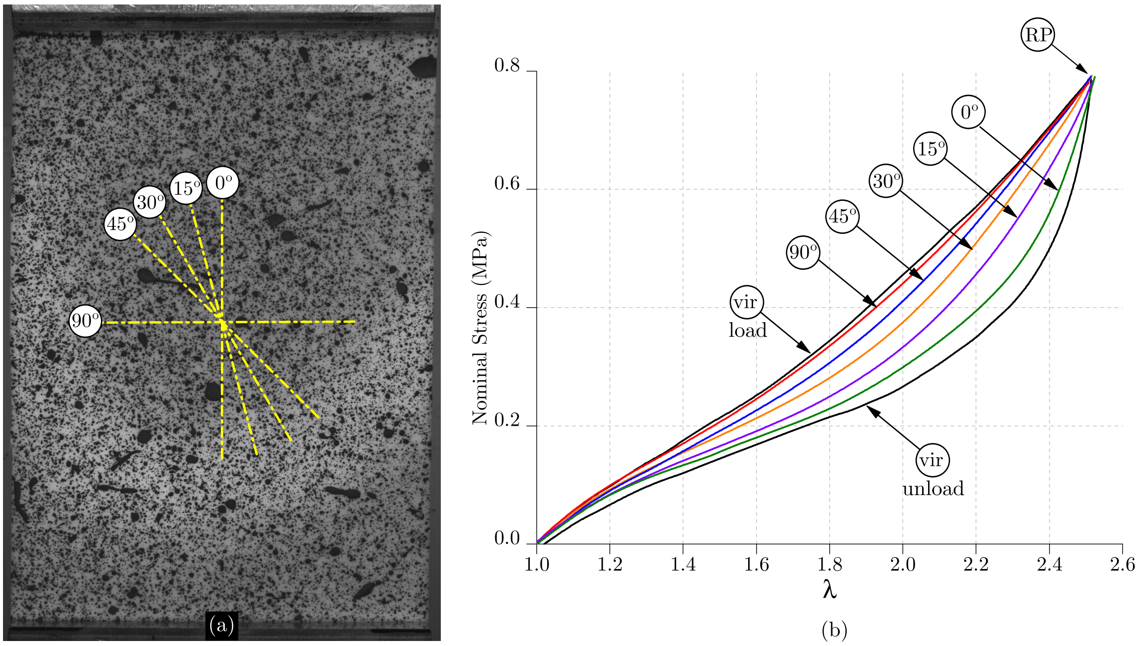

Figure 3.1: (a) Preconditioned large sample with the representation of different orientations of the tensile test cut specimens. (b) Induced anisotropy represented by the superposed uniaxial stress-strain responses for the different angles between the first and second loading directions. Curves are compared with the uniaxial tensile (load-unload) of a virgin specimen.

3.2.2 Mullins anisotropy induced by biaxial tensile pre-stretch

The objective of this section is to propose an experimental test that permits to analyze second tensile load curves in a material that experienced a more complex first load path. A biaxial tensile pre-stretch can be used to generate a complex in-plane deformation history, under incompressibility assumption. The complexity of this deformation history is given by the biaxiality ratio (μ), that can be expressed as a relation between principal in-plane stretches (λ_{max},λ_{min}) in the form

$$\mu = \frac{\ln(\lambda_{min})}{\ln(\lambda_{max})}. \tag{3.1}$$

Thus, biaxiality ratio is very useful to characterize the first history imprinted in the material at the first loading. Note that in the uniaxial tensile pre-stretch (Section 3.2.1), the contractive stretches are the minimal principal directions, then the biaxiality ratio is fixed in $\mu = -0.5$.

In this work the bulge test is proposed as an original way to yield very different biaxial strain-histories for first load path. As pointed in Machado *et al.* (2011b) bulge test is able to provide more information than the traditional application to determine the material equibiaxial response. It can be used to generate different biaxial states along a radial path of specimen from the equibiaxial state ($\mu = 1$) at the pole until the planar (pure) shear ($\mu = 0$), i.e., a large biaxiality ratio interval ($\mu \in [0, 1]$).

Using the 3D-DIC technique, it is possible to determine the three-dimensional surface displacements and the principal stretches (λ_m, λ_c) in the meridional and circumferential directions, as schematized in Fig. 3.2. From this point forward, these directions will be denoted by the subscripts m and c respectively. Nevertheless, in the axisymmetric case, deformed membrane principal stresses (σ_m, σ_c) are determined from principal curvatures (κ_m, κ_c) combined with the measurement of the inflating pressure (p). These fields are related as follow

$$\sigma_m = \frac{p}{2h\ \kappa_c} \tag{3.2}$$

$$\sigma_c = \frac{p}{2h\ \kappa_c}\left(2 - \frac{\kappa_m}{\kappa_c}\right), \tag{3.3}$$

where h is the current thickness calculated using the incompressibility assumption. κ_m and κ_c are deduced from 3D-DIC measurements. Thus, the stress-strain state is then known at any surface point which enriches greatly experimental data deduced from bulge tests. For a comprehensive explanation see Machado *et al.* (2011b).

The specimen geometry consists in thin circular plate, of initial radius $R = 90\,\text{mm}$ with a thickness $h_0 = 2\,\text{mm}$. The circular plate is simply supported and subjected to an uniform inflating pressure acting perpendicular to the current configuration. Using the 3D-DIC strain field measures, a set of interest points are specified along the radius of undeformed membrane permitting to know the stress and strain histories for every point over the deformed membrane surface. This set of points is represented in Fig. 3.2, where each point can be regarded as a small specimen in view of 3D-DIC as a full field strain measure method. Point a corresponds to the membrane center and the other points (b to j) are 10 mm equidistant through the meridional direction.

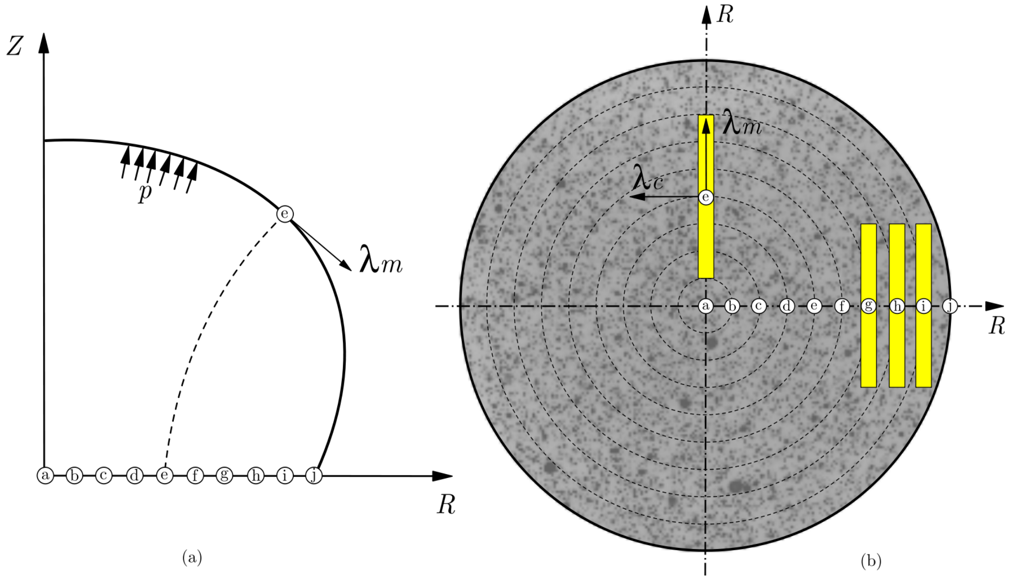

(a)

(b)

Figure 3.2: Schematic representation of biaxial preconditioning method and principal stretches: (a) axisymmetric representation of the bulge test with the interest points; (b) Illustration of the cut subsamples over different directions in the circular membrane.

Fig. 3.3 presents the first loading strain and stress history of points a to h in function of the load pressure. Note that each inflation state involves a heterogeneous stress-strain state that evolves from an equibiaxial state at the pole ($R = 0\,\mathrm{mm}$ - point a) tending to planar stretching nearest the clamp ($R = 90\,\mathrm{mm}$ - point j). Machado *et al.* (2011b) pointed out the experimental difficulty concerning the measurements on the overall membrane surface and the region near the clamp simultaneously. For materials that experience high displacements a self-shadow effect is observed in this last region.

The highest reached values for principal stretches (λ_m, λ_c) and first invariant (I_1) experienced in the pre-stretch test for each point (a to j) are presented in Fig. 3.4(a). Fig. 3.4(b) presents the mean value and the range of the biaxiality ratio (μ) for all pressure load steps in each point a to i. The measured ratio is almost constant at a given point and variations between the different pressure load steps can be disregarded. Due to the experimental difficulties concerning the measurements near the clamp, the curves in Fig. 3.4 were extrapolated for points i and j using polynomial approximation and represented by dotted lines. After a recovery time of 1 h, a set of tensile test specimens are cut. Two series of samples are defined as follows: samples aligned to the meridional direction denoted by 0^o and samples tangent to the circumferential direction (or perpendicular to the meridional direction) denoted by 90^o. Both series are illustrated in Fig. 3.2(b).

At first, the samples aligned to the meridional direction (0^o) were submitted to an uniaxial tension test. The loading consists of a simple load unload cycle, where the upper limit overpass the maximum value reached, in the biaxial pre-stretch (see Fig. 3.4(a)), by the major principal stretch (λ_m). Fig. 3.5 presents the second load curves for the different specimens and a virgin uniaxial tensile load curve (*vir*) as reference. The load curves of points b, c and d are quasi superposed, thus they are not represented in the figure keeping clear the results visualization.

It appears that all the curves are different. The figure highlights that closer the sample is from the bulge pole, more stress-softening is observed. Two aspects are observed, the difference between the reference curve (*vir*) and second load is increasing and the strain-hardening for the return point (RP) on the reference curve appears later. These results are in consistency with the first maximal deformation level presented in Fig. 3.4(a).

Second, the samples cut at points g, h and i perpendicularly to the meridional direction (90^o) are tested. However, the second load–unload curves corresponding to points a, g, h and i are presented for both directions (0^o and 90^o) in Fig. 3.6 and compared to the virgin load curve (*vir*). The deformation is evaluated locally, using DIC, in a small zone located in the samples center. It clearly appears that the second load curves, for both directions, come back on the first loading curve at that same maximal deformation but with different levels of stress-softening. This confirms the results of the previous Section (3.2.1). But this time, a stress softening appears in the orthogonal directions as the material was also stretched in this direction during the preconditioning path.

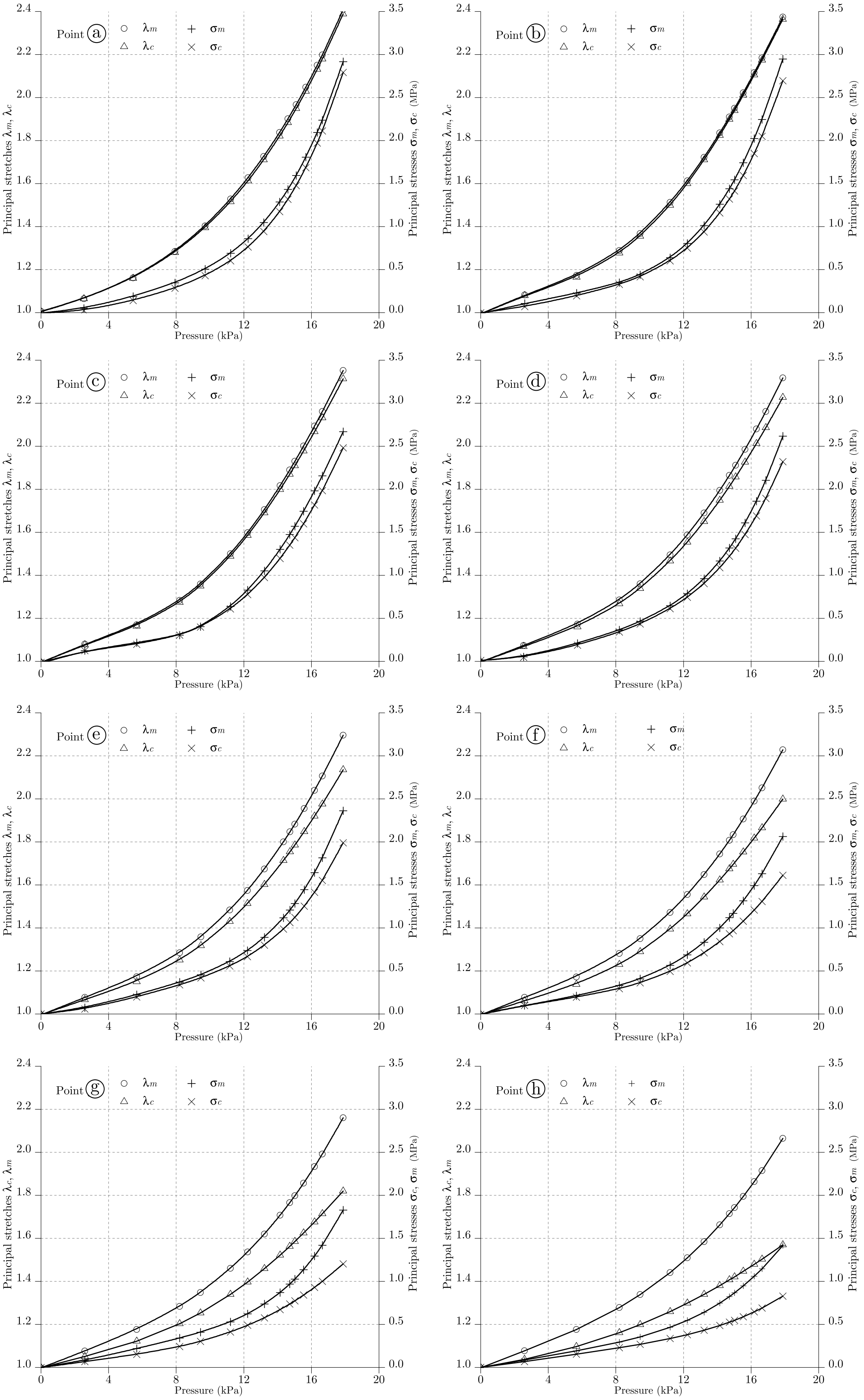

Figure 3.3: Bulge test deformation history for points a to h. Principal stretches (λ_m,λ_c) and current principal stresses (σ_m,σ_c) are presented respectively on left and right axis according to the inflating pressure (p).

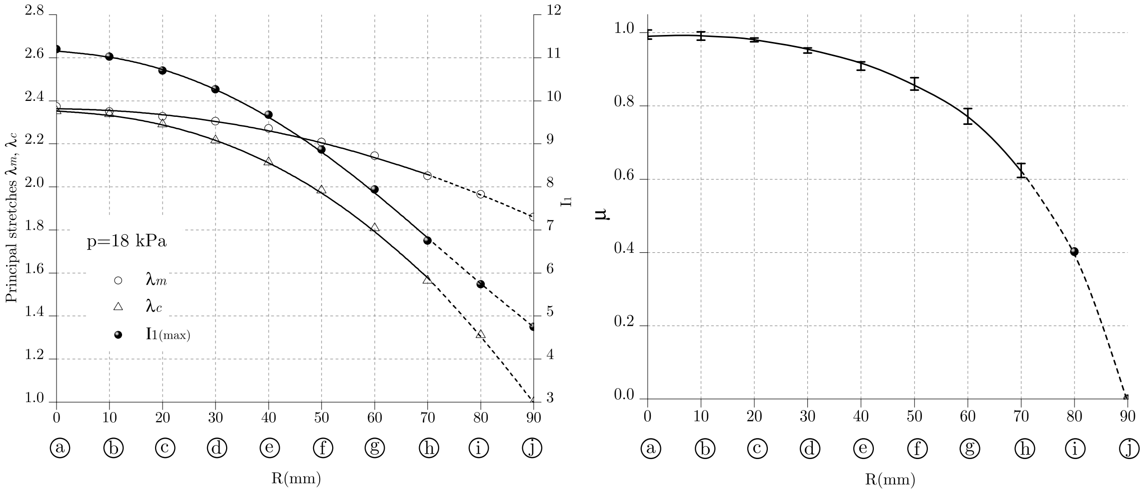

(a) (b)

Figure 3.4: (a) Highest deformation level experienced on the first biaxial load history ($p = 18\,\text{kPa}$) for each meridional point (a to j) in terms of principal stretches (λ_m, λ_c) and first invariant (I_1); (b) Mean value and range of biaxiality ratio (μ) during all pressure load steps. Points i and j were extrapolated using a polynomial approximation (dotted lines).

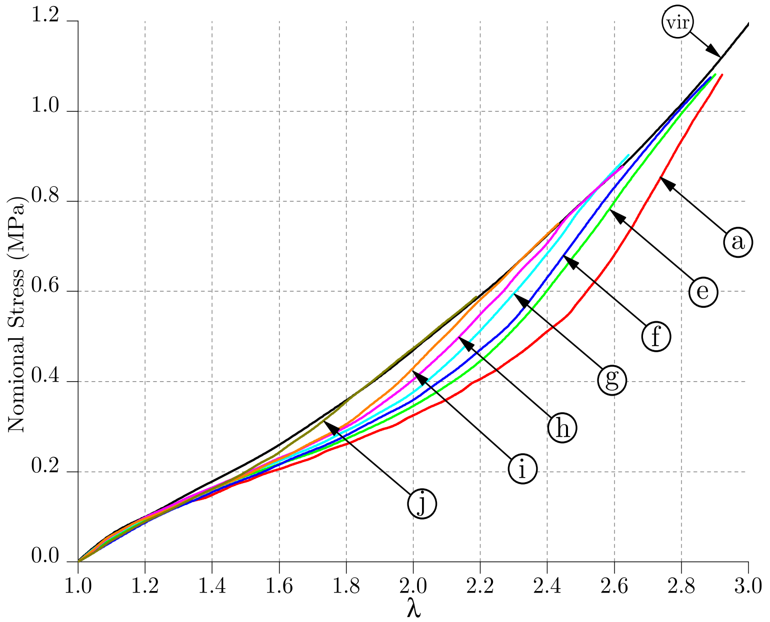

Figure 3.5: Influence of the biaxial first loading on tensile test response. Uniaxial traction performed at 0^o with respect to the meridional direction for the subsamples a, e, f, g, h, i, and j.

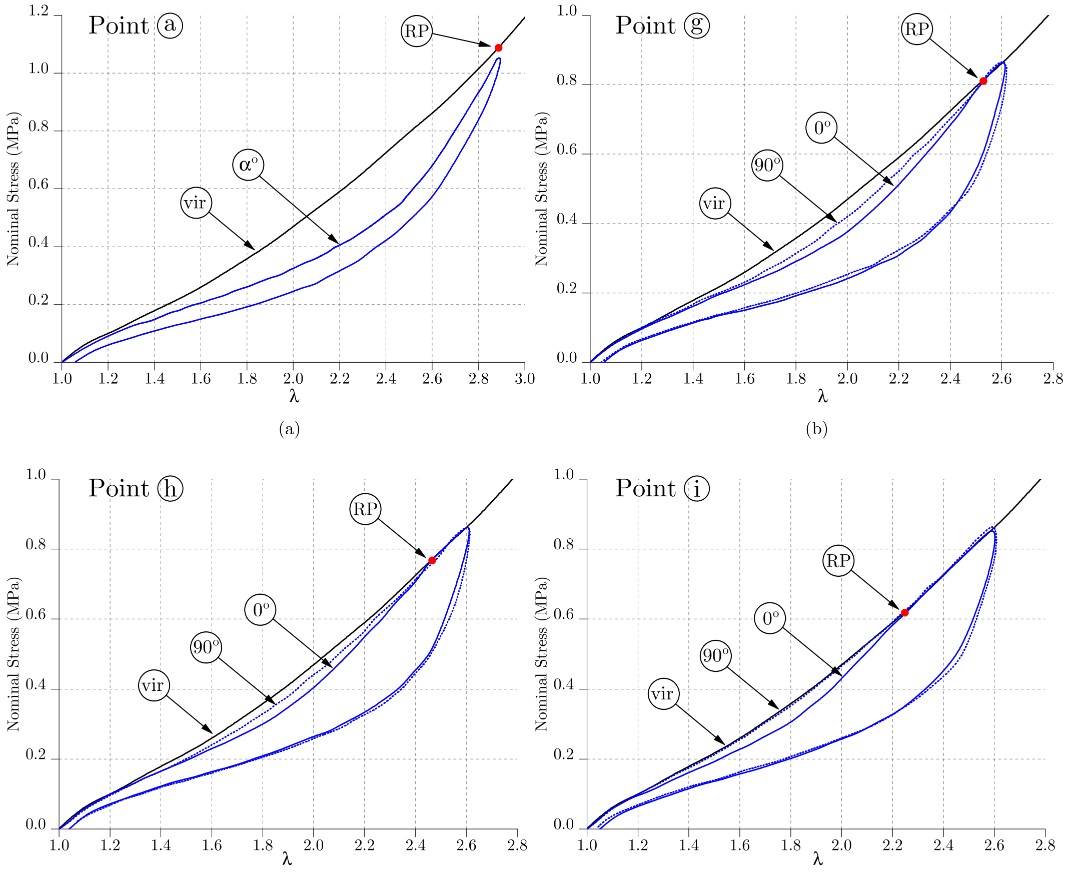

(a) (b)

(c) (d)

Figure 3.6: Second load (and unload) curves of specimens a, g, h and i cut from the bulge plate at 0^o and 90^o with respect to the meridional direction. Note that, for point a, only one curve is presented since the all directions are equivalent.

3.3 Discussion

3.3.1 Anisotropy induced by uniaxial tensile pre-stretch

First, the uniaxial tension deformation history tests are analyzed. Fig. 3.7(a) shows the stress ratio (δ) between the uniaxial tension virgin load curve (P_0) and the set of subsamples orientated at 0^o, 15^o, 30^o, 45^o and 90^o directions ($P_{2^{nd}}^{(\alpha)}$)

$$\delta = \frac{P_{2^{nd}}^{(\alpha)}}{P_0}. \tag{3.4}$$

where P denotes the nominal tensile stress. The curves, concerning Eq.(3.4), highlight that, given a deformation level, there is no stress proportionality between the different directions.

Recalling that the first Piola–Kirchhoff stress tensor $\mathbf{P}$ is work-conjugate to the rate of deformation gradient $\dot{\mathbf{F}}$, a stored strain energy density can be established as the work done by the stresses from the initial to the current position as

$$\mathcal{W} = \int_0^t \mathbf{P} : \dot{\mathbf{F}} \, dt. \tag{3.5}$$

Thus, it becomes possible to define an energy loss ratio η that quantifies the evolution of the energy loss by Mullins effect according to the loading angle α, given by

$$\eta = \frac{\mathcal{W}_0 - \mathcal{W}_{2nd}^{(\alpha)}}{\mathcal{W}_0 - \mathcal{W}_{2nd}^{(0^o)}} \tag{3.6}$$

where $\mathcal{W}_0$ and $\mathcal{W}_{2nd}^{(\alpha)}$ are respectively the strain energy of virgin material and the strain energy of a second loading in a given direction α. Fig. 3.7(b) presents the evolution of the energy loss by Mullins effect according to the loading angle in the uniaxial tensile pre-stretch condition for the maximal reached tensile stretch ($\lambda_{max} = 2.50$). The second load $\mathcal{W}_{2nd}^{(0^o)}$ is used as reference since the same direction is used for the first and the second loading curves. Using a periodic approximation, the function η in Eq. (3.6), is fitted by

$$\eta = a_0 + a_1 \cos(2\alpha) + a_2 \cos(4\alpha) \tag{3.7}$$

where $a_0 = 0.44$, $a_1 = 0.46$ and $a_2 = 0.10$. It appears that the energy loss ratio (η) evolves from a maximum, when first and second loadings are in the same direction to a minimum, close to zero, when the directions of first and second loadings are orthogonal.

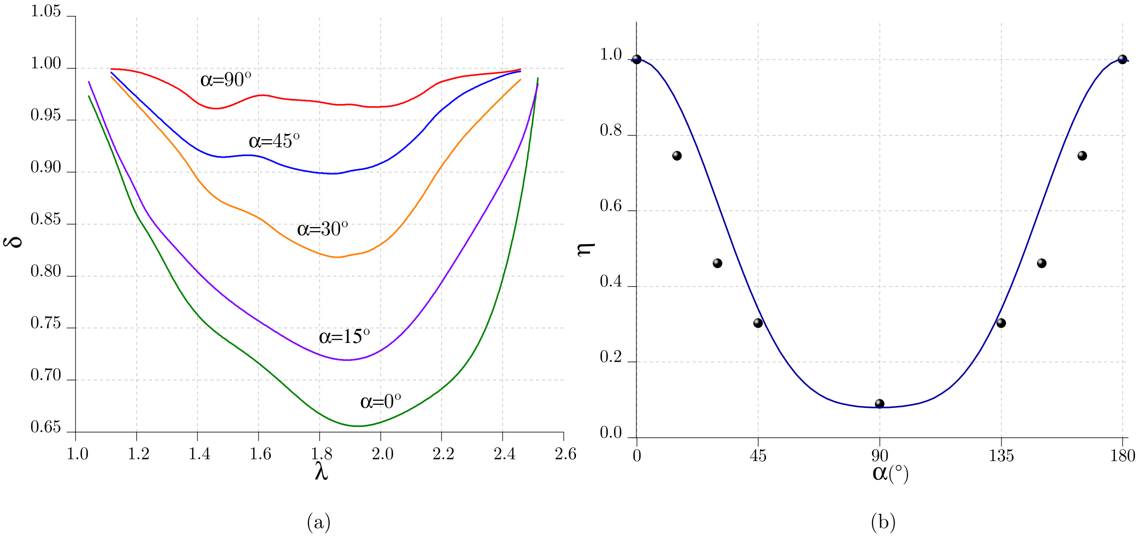

Figure 3.7: (a) Stress ratio between the first virgin load curve and the set of subsamples orientated at 0^o, 30^o, 45^o and 90^o (perpendicular) directions. (b) Ratio of energy loss according to the different loading angles.

3.3.2 Anisotropy induced by biaxial tensile pre-stretch

Concerning the biaxial test preconditioning, Fig. 3.8 shows the tensile test stress ratios of specimens cut in meridional (0^o) and circumferential (90^o) directions in the bulge specimen with respect to the tensile test virgin curve (vir). Similarity to Section 3.3.1, no proportionality between the first and second load curves was observed. Nevertheless, a main difference appears, compared with Fig. 3.7. The curves at 90^o for points g and h present a considerable stress softening. This is due to the biaxial pre-loading where the directional intensity of the stress softening depends on the biaxiality ratio (μ). This emphasizes that subsequent directional behavior is strongly influenced by how the maximal pre-loading is applied.

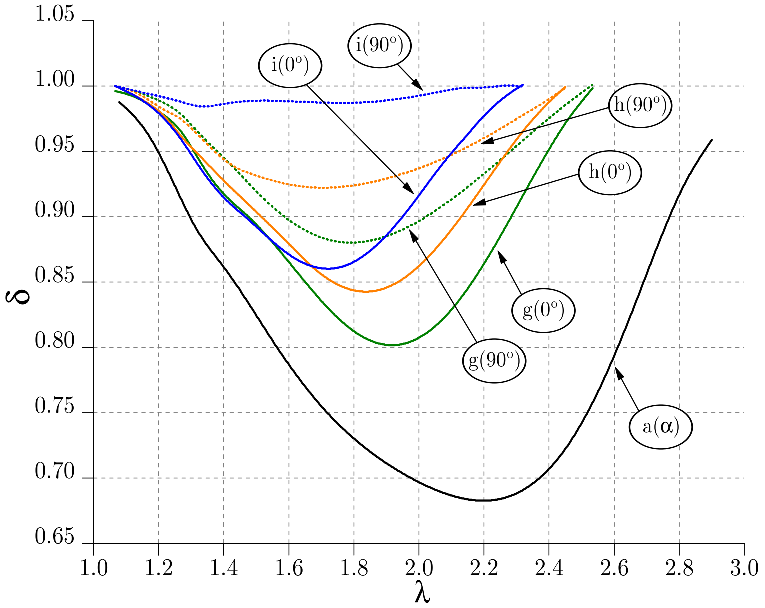

Figure 3.8: Stress ratio between the first virgin load curve (vir) and the second load for the uniaxial extension, performed on meridional (0^o) and circumferential (90^o) specimens for points a, g, h, and i.

3.3.3 Relevance of maximal deformation criterion for describing Mullins effect

The choice of the Mullins effect evolution criterion is fundamental for the description of different loading paths. Considering the deformation of the material as a thermodynamic process, this criterion, i.e., this state variable, must describe the momentary maximum condition of the material deformation regardless of the path by which the system goes from one state to another. In other words, this state variable defines how the stress softening evolves for an arbitrary path with respect to the maximum state achieved in the previous load path.

In the uniaxial tensile pre-stretch case, Fig. 3.1(b) showed that all second load curves come back on the first load curve at the same point (RP), characterized by its tensile stretch, independently of the direction of the second load. For other load types than tension, the maximum value of the major principal stretch is important to define the return point (RP) but deformations in other directions cannot be neglected in stress softening accounting. Machado *et al.* (2010) showed that for an isotropic approach, the strain energy or the first invariant can be used to describe the evolution of stress softening. Fig. 3.5 which presents the second load curves after the biaxial tensile pre-stretch is replotted according to the first invariant in Fig. 3.9(a). In the same figure, the maximal value of $I_{1(max)}$ reached during the biaxial preconditioning load from Fig. 3.4(a) have also been plotted. For each point a to j, the value of the return point ($I_{1(RP)}$), i.e., where the second load curves come back on the first uniaxial loading one (*vir* curve), are compared to the $I_{1(max)}$. The results are presented in Fig. 3.9(b). The points are quite aligned, but they do not fit well the first bisectrix. The bisectrix represents the one-to-one relationship between the first invariant for two different loading paths. It means that the first invariant cannot be an efficient criterion to describe the maximal deformation.

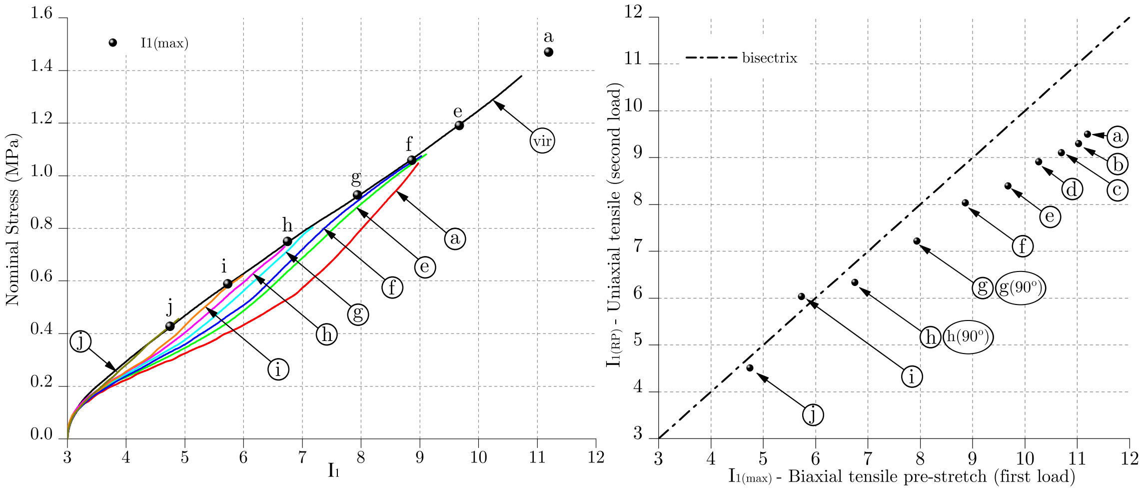

(a) (b)

Figure 3.9: Influence of the biaxial first loading on tensile test response. (a) Uniaxial traction performed at 0^o with respect to the meridional direction for points (a, e, f, g, h, i, and j – represented by solid lines) and the maximal first invariant $I_{1(max)}$ (dots) reached during the biaxial first load (from Fig. 3.4(a)). (b) relation between the maximal first invariant $I_{1(max)}$ and the value of $I_{1(RP)}$ when the second load curve comes back on the reference first loading curve (*vir*-curve).

3.3.4 Relevance of maximal strain energy criterion for describing Mullins effect

The above results highlight that the maximal value of a thermodynamic variable reached in the loading history based on deformation measures are not sufficient as the amount of stress softening varies for a same maximal previous deformation. The fact that the material was loaded in the transverse direction in the biaxial pre-stretching, has a large influence on the stress softening, that means that a three dimensional criterion must be taken into account.

The Mullins effect can be quantified by the ratio between the strain energy during first loading ($\mathcal{W}_0$) and the second loading ($\mathcal{W}_{2^{nd}}$), defined as

$$\psi = \frac{\mathcal{W}_{2^{nd}}}{\mathcal{W}_0}. \tag{3.8}$$

These strain energy densities are evaluated by integration of first and second load curves for both preconditioning methods. Note that, in the biaxial preconditioning, $\mathcal{W}_0$ is evaluated during the bulge test (for each point a to h), whereas $\mathcal{W}_{2nd}$ is evaluated from the second tensile tests up to the return point limit. Hence, the ratio of strain energy is calculated and presented in Fig. 3.10. Furthermore, the cyclic tests results of uniaxial, planar and equibiaxial extensions, published in Machado *et al.* (2010), were extracted and superposed in the same plot composing an additional information about different loading paths. It clearly appears that all points obtained by different strain histories follow a tendency and they can be fitted by a master curve. An exponential decay approximation is proposed for the function (ψ), and given by

$$\psi = \psi_{os} + \psi_0 \exp(-c\mathcal{W}_0) \tag{3.9}$$

where $\psi_{os} = 0.29$, $\psi_0 = 0.63$, and $c = 0.75\,\mathrm{m}^3/\mathrm{MJ}$. Note, in Fig. 3.10 that the energy ratio evolves from a maximum, where even minor deformation starts the dissipation process, to a minimum that cannot be reached before the rupture of the material. However, this master function does not make sense when the second load energy ($\mathcal{W}_{2nd}$) is evaluated in a different direction than the first loading principal direction. The results from the uniaxial pre-stretching clearly show this non-compliance. Thus, strain energy differences between principal directions should be analyzed.

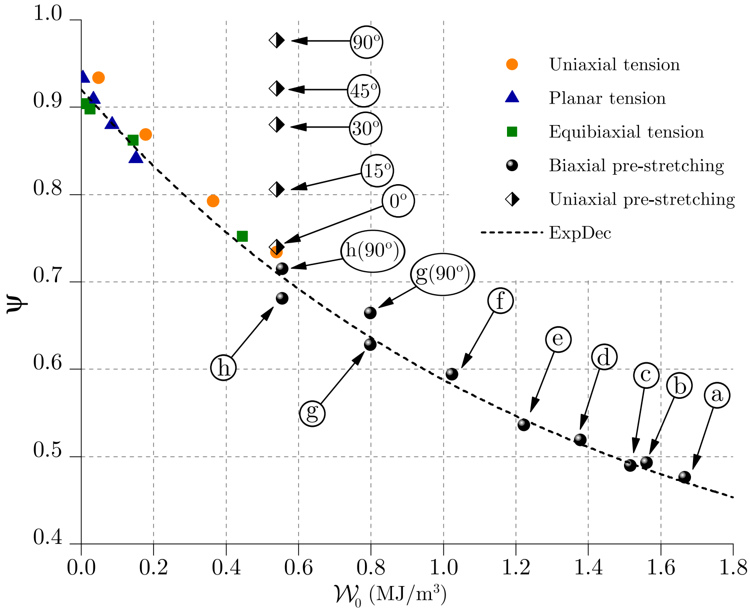

Figure 3.10: Strain energy ratio (ψ) between second loading curve and the primary virgin loading curve for different strain histories. Points are fitted by an exponential decay function.

3.3.5 Analysis of a decomposed strain energy

Considering that the strain energy at first load in biaxial tension ($\mathcal{W}_0^B$) can be decomposed into two parts, then

$$\mathcal{W}_0^B = \mathcal{W}_0^{(m)} + \mathcal{W}_0^{(c)} = \int P_m \, d\lambda_m + \int P_c \, d\lambda_c \tag{3.10}$$

where $\mathcal{W}_0^{(m)}$ and $\mathcal{W}_0^{(c)}$ are the strain energies at the first load for meridional and circumferential directions respectively. A schema is proposed in Fig. 3.11(a) to explain this decomposition. Fig. 3.12(a) shows how these energy portions vary from the pole until the bulge border for the maximal pressure step ($p = 18\,\text{kPa}$). The meridional energy ($\mathcal{W}_0^{(m)}$) decreases along the meridional direction but remains important, whereas the circumferential energy ($\mathcal{W}_0^{(c)}$) tends to zero near the specimen border where there is no circumferential deformation.

With the knowledge of the above decomposition, the suitability of the parameter ($\mathcal{W}_0$) to describe the stress softening can finally be evaluated. The idea is to compare if two different first loading paths can produce an energetically equivalent deformation state. The schema proposed in Fig. 3.11(b) for a generic position (a to h) in the bulge surface helps to explain this evaluation. First, the return point (RP) of second loads in the uniaxial tension (vir-curve) for each sample a to h are identified. It is important to remind that, for a given position in the bulge surface, the return occurs at the same point (RP) independently of the second tensile load direction as shown in Fig. 3.6. Then, an equivalent energy of a virgin material in uniaxial traction ($\mathcal{W}_0^U$) is evaluated up to this same return point RP. Finally, this equivalent energy ($\mathcal{W}_0^U$) is compared with the real energy ($\mathcal{W}_0^B$) used to pre-stretch the membrane.

The strain energy $\mathcal{W}_0^U$ are plotted in function of $\mathcal{W}_0^B$ in Fig. 3.12(b). It clearly appears that the $\mathcal{W}_0^U$ values are not in the graph bisectrix. The fact that the total energy $\mathcal{W}_0^B$ are in the right side from the bisectrix means that a superior amount of energy would be necessary to produce the same state equivalent state given by the $\mathcal{W}_0^U$ energy. In order words, there is a part of the total strain energy that was not used in the stress softening process. Thus, the total strain energy is not the key to describe the return on the virgin curve.

To measure the influence of loading directions, the same comparisons are realized but considering the decomposition proposed in Eq.(3.10). Fig. 3.12(b) shows that the maximal principal direction strain energy, $\mathcal{W}_0^{(m)}$, fit better the bisectrix curve, while for the energy in the other principal direction, $\mathcal{W}_0^{(c)}$, nothing can be concluded. This means that, if the maximal principal direction remains the same during the first and second load cycle, the amount of strain energy can be a measure of the Mullins effect in this direction. In the other directions, a coupling effect exists between different directions and it influences the Mullins effect amount.

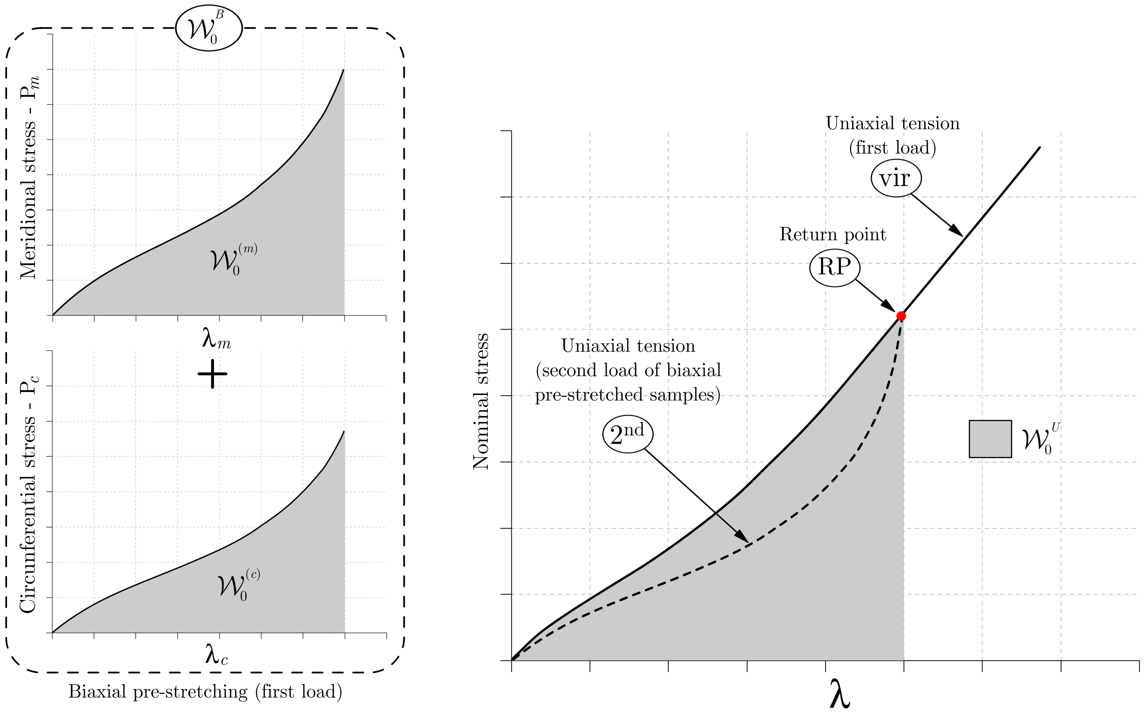

(a) (b)

Figure 3.11: First and second load strain energy schema. (a) The strain energy decomposition for the biaxial pre-stretching. (b) The equivalent energy ($\mathcal{W}_0^U$) evaluated until the return point (RP) of a given biaxial pre-stretched sample on the uniaxial first load reference curve (vir).

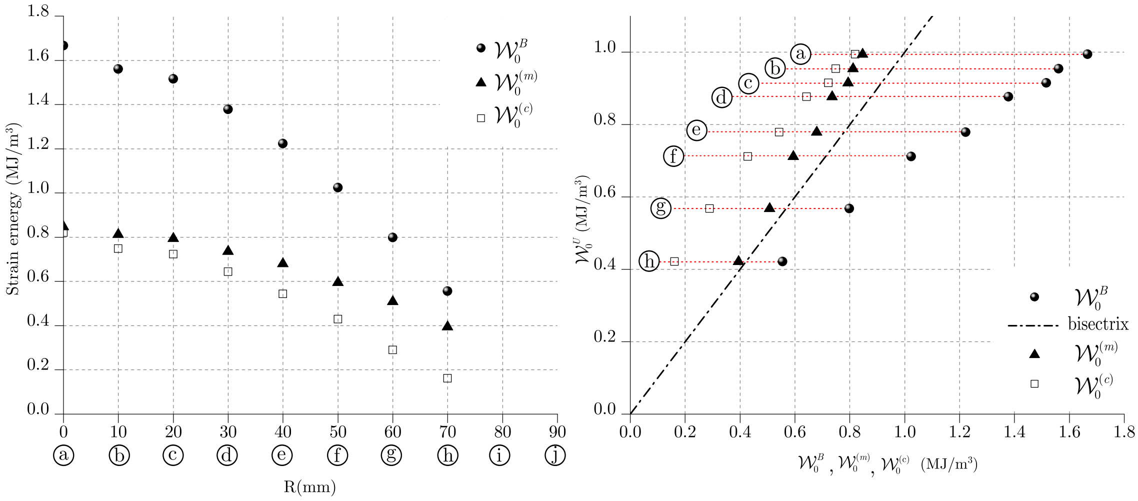

(a) (b)

Figure 3.12: Bulge test strain energy analysis.

3.4 Conclusion

The motivating key for this work was the absence of a comprehensive experimental study to build evidence showing that the Mullins effect in filled silicone rubbers is a strongly anisotropic phenomenon. Using the 3D-DIC method as a non-contact full-field optical measurement, a large strain level was achieved and two methods were employed to record an initial deformation history. The results showed that preconditioning tensile cycles in one direction hardly cause any softening in the perpendicular direction. Nevertheless, all second load curves come back on the first tensile load curve at the same point independently of the direction of the second load. The results with respect to the influence of Mullins effect in the intermediate directions permit to examine in detail the angular distribution of memory effects for testing and calibrating numerical models.

The use of bulge test, as a biaxial preconditioning test, was originally proposed to find an evidence for an even more complex memory behavior of the material. The measurements made along the meridian of the inflated membrane provide unprecedented information about the history of principal stress and principal strain directions without an explicit dependency of any constitutive relation. Results showed that the induced anisotropy is dependent on the pre-stretch biaxiality ratio. Again, the return on the first load reference curve of all second load curves occurs at the same point, independently of the second load direction. On one hand, the ratio of energy between first and second load loading seems to follow a master behavior according to virgin strain energy. On the other hand, the come back on the virgin uniaxial curve can be controlled by the amount of energy, but only in the maximal principal direction whereas in the other directions, a coupling phenomena exist between different directions.

Note also that the form and intensity of the anisotropy of the Mullins effect could depend on the elastomer type, the properties of filler particles, and their mass and volume proportion in the polymeric matrix.

Chapter

4

Theory and identification of a constitutive model of induced anisotropy by the Mullins effect

G. Machado, G. Chagnon, D. Favier

To be submitted

During cyclic loading, rubber like materials exhibit a stress-softening phenomenon known as the Mullins effect. In the last few years, some constitutive equations have been proposed to deal with this effect including induced anisotropy, but all these models lay on few experimental data. In that respect, data on filled silicone rubber were recently presented [Machado, G., Chagnon, G., Favier, D., 2011. Induced anisotropy by the Mullins effect in filled silicone rubber. Mech. Mater., submitted]. The authors used uniaxial and biaxial tests to precondition samples inducing some primary stress-softening. Next, uniaxial tensile tests were conducted on preconditioned samples. An analysis of these data permits to highlight that the maximum elongational energy in the maximum principal direction is the governing parameter that defines the return–point on the virgin loading curve. Moreover, the relation of the elongational energy in each direction with the maximum elongational energy permits to describe the amount of stress-softening. A generic form of modeling is built by superposing an isotropic hyperelastic model and a stress-softening model based on the double network theory, taking into account the contribution of many spatial directions and a global equivalent measure. Finally a constitutive equation is proposed. The model is fitted and compared to experimental data. The abilities of such kind of model are finally explained.

Contents

4.1 Introduction

Rubber-like materials present a stress-softening after a first loading cycle, known as the Mullins effect (Mullins, 1947). Different studies have highlighted that this phenomenon induces anisotropy by a strong directional stress-softening dependency. Different definitions have been given to the Mullins effect, in this paper the Mullins effect is considered as the difference between the first and second loadings.

In a first approach, many isotropic modeling were proposed. First, physical modeling taking into account the evolution of the chain network were proposed. Govindjee and Simo (1991, 1992) proposed a model based on the evolution of the macromolecular network by a decomposition of the network into a hyperelastic one and an evolving one. In an other way, Marckmann *et al.* (2002) considered that the network can be represented by the eight chains model (Arruda and Boyce, 1993) with chain lengths and chain densities which are evolving with the maximum deformation. In another way, double network theory was developed (Green and Tobolsky, 1946) considering that the rubber-like material can be decomposed into a hard and a soft phase; the hard phase is transformed into soft phase with the stress-softening. Different equations were proposed (Beatty and Krishnaswamy, 2000; Zuñiga and Beatty, 2002). At the same time, the damage theory was often used to describe the stress-softening (Simo, 1987; Miehe, 1995; Chagnon *et al.*, 2004). In a last point of view, Ogden and Roxburgh (1999) and Dorfmann and Ogden (2003) proposed models based on pseudo-elasticity. All these models fit more or less accurately experimental data but they consider only one load direction, i.e., without changing loading direction between first and second loadings. For a more exhaustive review about these models, the reader can refer to Diani *et al.* (2009).

To improve the modeling and to fit anisotropic stress softening, new approaches were developed taking into account the difference of stress-softening in each direction. First Diani *et al.* (2006a) proposed a generalization of the Marckmann *et al.* (2002) model by a decomposition of the rubber-like materials by means of chains oriented into 42 or more directions in space. In each direction, the quantity and the length of chains can evolve with the maximum elongation in the considered direction. This model can describe different stress-softening in different directions with permanent deformation after unloading. Dargazany and Itskov (2009) proposed the same kind of approach by taking into account that in each direction, different chains with different length exist. They integrate the density of probability in each direction by taking into account the evolution of the network at each step. Shariff (2006) proposed an anisotropic damage model taking into account different damages in the three principal directions by the introduction of a second order damage tensor. This model permits to describe transverse anisotropy of the Mullins effect. In the same way Itskov *et al.* (2010) proposed three damage evolutions for the three principal directions. These models permit to recover a stiffer material in the orthogonal direction when the material is loaded at a higher deformation than the one previously applied. This property is not adapted to all materials.

All these anisotropic models are proposed by analyzing oriented tensile tests. Nevertheless, Machado *et al.* (2011a) recently performed other original tests based on pre conditioning with uniaxial tension and biaxial tension tests. This paper proposes a new approach for the modeling to describe these experimental data. In Section 4.2, the global framework of the Mullins effect modeling is proposed owing to experimental data of the literature on silicone rubber. In Section 4.3, a new approach is proposed to write constitutive equations by introducing a tensor that describes the repartition of the elongation energy in the space. The conditions to be verified by the equations are detailed. In Section 4.4, a first constitutive equation is proposed. It is fitted and compared to experimental data. Finally, Section 4.5 contains some concluding remarks and outlines some future perspectives.

4.2 Macromolecular approach to model Mullins effect

4.2.1 Filled silicone behavior

Different tests highlighting the stress softening anisotropy have been presented in the literature on different rubber-like materials in the last few years, see for example (Muhr *et al.*, 1999; Besdo *et al.*, 2003; Diani *et al.*, 2006b; Hanson *et al.*, 2005). In this paper, attention is focused on the largest and most diverse database concerning Mullins effect anisotropy of a rubber like material to the best of our knowledge. These data concern the results on the RTV3428 filled silicone rubber Machado *et al.* (2011a).

The first set of experimental data is based on classical experimental tests, i.e., cyclic experiments with an increasing deformation after each cycle, were realized during tensile, pure shear and equibiaxial tensile tests. The data are reported in Machado *et al.* (2010). A second set of experimental data is based on stress-softening anisotropy, induced by two distinguished pre-conditioning methods (Machado *et al.*, 2011a): the first one (noted as TT in the following), consists in a first loading in tension and a second loading also in tension, but at this time in four different directions; and the second pre-conditioning method (noted as BT), consists in a first biaxial extension loading followed by a second loading in tension. The originality of these data is that the loading states are very different between the first and the second loads. Moreover the orientation of the maximal principal deformation is not necessarily the same between the two loads.

These new experimental results question the existing anisotropic constitutive equations and the main reasons are detailed here. First, Diani *et al.* (2006a) and Dargazany and Itskov (2009) models present an important permanent deformation that is related to the stress-softening. But here, the material exhibits an important stress-softening without permanent deformation. Second, for a second tensile loading orthogonal to the first loading one, the models of Shariff (2006) and Itskov *et al.* (2010) present a stiffer behavior than the virgin material which is not the case of the filled silicone rubber. Last, all these modeling consider different material directions and the Mullins effect is controlled only by the maximum elongation in the considered direction. Thus a new way to treat Mullins effect should be proposed, at the sight of Machado *et al.* (2011a) experimental data.

4.2.2 Two-network theory

The results presented on silicone rubber-like materials highlight that unfilled silicone rubbers do not present stress-softening (Meunier *et al.*, 2008) whereas filled silicone rubbers (Machado *et al.*, 2010) present an important one. For this silicone rubber material, it can be argued that the Mullins effect is principally due to the presence of filler in the material which is not the case for every rubber like material. In the light of these findings, a model is proposed based on Govindjee and Simo (1991, 1992) theory. The macromolecular network can be represented by the network drawn in Fig. 4.1. There exist different macromolecular chains in the network, those which are linked to filler and those which are only linked to other macromolecular chains. Govindjee and Simo (1991, 1992) did the hypothesis that only the chains which are linked to filler are concerned with Mullins effect. The same hypothesis is considered here, that means that the energy density can be decomposed into two parts

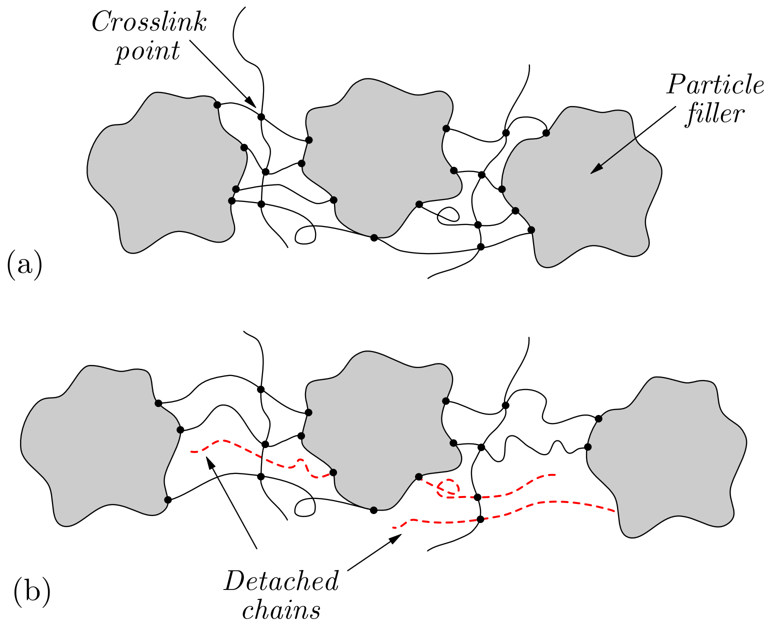

Figure 4.1: Representation of the silicone organization with macromolecular chains and filler particles

$$\mathcal{W} = \mathcal{W}_{cc} + \mathcal{W}_{cf} \tag{4.1}$$

where $\mathcal{W}_{cf}$ and $\mathcal{W}_{cc}$ represent the energy densities of the chains linked to filler, and of the chains linked to other chains, respectively. On the one hand, as it is considered that the chains linked to other chains do not undergo Mullins effect, $\mathcal{W}_{cc}$ is therefore represented by a hyperelastic energy density. Moreover, all the chains are randomly oriented in the material, that means that an isotropic strain energy density can be used. On the other hand, $\mathcal{W}_{cf}$ should represent the anisotropy of stress-softening of the material. Thus $\mathcal{W}_{cf}$ must be decomposed into the contribution of the material in different directions in space. Bazant and Oh (1986) proposed different orientation schemes, that define the set of vectors $\mathbf{a}_0^{(i)}$ with different weight $\omega^{(i)}$ for each direction to obtain a material as close as possible to an isotropic material when all the chains have the same mechanical behavior. $\mathcal{W}_{cf}$ is then written as

$$\mathcal{W}_{cf} = \sum_{i=1}^{n} \omega^{(i)} \mathcal{W}_{cf}^{(i)}(\mathbf{a}_0^{(i)}) \tag{4.2}$$

where n is the number of considered directions and $\mathcal{W}_{cf}^{(i)}(\mathbf{a}_0^{(i)})$ is the elongational hyperelastic energy of the chain in the initial direction $\mathbf{a}_0^{(i)}$.

4.3 Choice of the governing parameters of the Mullins effect

4.3.1 Analyze of literature experimental data

The different conclusions identified by Machado *et al.* (2011a) are analyzed and the consequences for the modeling are detailed. During TT tests (uniaxial tension preconditioning followed by second tensile tests) whatever is the orientation of the second loading cycle, the strain-stress curves come back on the first loading curve on the same point corresponding to the maximum deformation encountered during the first tensile loading cycle. Nevertheless the amount of stress softening depends on the angle between the first and second loading cycles. This means that the return on the tensile virgin curve is controlled by a maximum deformation but the amount of stress softening depends on the orientation of the loadings.

The BT tests (biaxial tension followed by second tensile test) were realized and the heterogeneity of the strain state and the axisymmetry were verified thanks to three-dimensional image correlation measurements. In the preconditioning step, the bulge test specimen underwent biaxial loadings with different biaxiality ratios. At the top of the bulge test, an equibiaxial loading is generated whereas a planar tension state is generated near the grips. Between these two points different biaxial states are generated (Machado *et al.*, 2011b). The specimens were cut along circumferential and meridional directions in the bulge test specimen and they were tested in tension. The different second strain-stress tensile curves, again, come back in the same point on the virgin tensile loading curve but with a different amount of stress-softening according to the direction (circumferential or meridional). The conclusions are thus the same as TT tests but with a biaxial loading as the preconditioning test.

This encourages to consider that the elongational energy in the maximal principal elongation is the governing parameter for the come-back on the first loading curve whatever is the second loading. Moreover the stress softening in the other directions are linked to this parameter but it is attenuated, if the maximum principal loading is not in the same direction between the two loads. A measure for these quantities should thus be introduced.

4.3.2 New measure definition

The strain energy is often used to describe the Mullins effect but, its use can only be limited to isotropic approach as the energy is a scalar global measure of the deformation state. A clue can be to compare the elongational energy in the different directions. It is, thus, proposed to introduce a measure of the elongational energy in one direction. Let us note $\mathbf{a}_0^{(i)}$ a material direction in the undeformed configuration. This direction is transformed into $\mathbf{a}^{(i)} = \mathbf{F}\,\mathbf{a}_0^{(i)}$ after a deformation, where $\mathbf{F}$ is the deformation gradient. The elongational energy increment $d\mathcal{M}^{(i)}$ during a time increment dt in the direction $\mathbf{a}^{(i)}$ is obtained by the scalar product of the stress vector by the deformation vector increment, i.e.,

$$d\mathcal{M}^{(i)} = \mathbf{a}^{(i)} \cdot \boldsymbol{\sigma}\mathbf{D}\,\mathbf{a}^{(i)}\ dt \tag{4.3}$$

where $\boldsymbol{\sigma}$ is the Cauchy stress tensor, $\mathbf{D}$ is the rate of deformation tensor. In the initial configuration, the elongational energy in the $\mathbf{a}_0^{(i)}$ direction is written as

$$d\mathcal{M}^{(i)} = \mathbf{a}_0^{(i)} \cdot\ \mathbf{F}^T\boldsymbol{\sigma}\mathbf{D}\,\mathbf{F}\,\mathbf{a}_0^{(i)}\ dt. \tag{4.4}$$

The global elongational energy is thus defined as

$$\mathcal{M}^{(i)} = \mathbf{a}_0^{(i)} \cdot \left[\int_0^t \mathbf{F}^T\boldsymbol{\sigma}\mathbf{D}\,\mathbf{F}\ dt\right] \mathbf{a}_0^{(i)} = \mathbf{a}_0^{(i)} \cdot \mathbf{M}\,\mathbf{a}_0^{(i)} \tag{4.5}$$

this permits to introduce a tensor $\mathbf{M}$, defined in the reference configuration, that describes the repartition, throughout the three-dimensional space, of the elongational energy. Let us represent the material by a distribution of $n-$direction $\mathbf{a}_0^{(i)}$ oriented in any space direction, as proposed by Bazant and Oh (1986). Different noticeable parameters can be defined. The maximum elongational energy for each direction $\mathbf{a}_0^{(i)}$ in the history is

$$\mathcal{M}^{(i)}_{\max} = \max_{\tau\leq t} \mathcal{M}^{(i)}(\tau) \tag{4.6}$$

At the current time t, the maximum instantaneous elongational energy in any direction is defined as

$$\mathcal{I}(t) = \max_{i} \mathcal{M}^{(i)}(t) \tag{4.7}$$

And last, the maximum elongational energy in any direction in the history is defined as

$$\mathcal{G} = \max_{\tau\leq t} \mathcal{I}(\tau) = \max_{i} \mathcal{M}^{(i)}_{\max}. \tag{4.8}$$

4.3.3 Construction of the evolution equation

An evolution function $\mathcal{F}^{(i)}$ is introduced along each direction, it describes the evolution of the network in the considered direction. The global elongational energy is then rewritten as

$$\mathcal{W} = \mathcal{W}_{cc} + \sum_{i=1}^{n} \omega^{(i)}\mathcal{F}^{(i)}\mathcal{W}^{(i)}_{cf}. \tag{4.9}$$

At the sight of the silicone filled rubber experimental data, the function $\mathcal{F}^{(i)}$ can be written as a function of the characteristic energy measures previously introduced

$$\mathcal{F}^{(i)} = \mathcal{F}(\mathcal{M}^{(i)}, \mathcal{M}^{(i)}_{\max}, \mathcal{I}, \mathcal{G}) \tag{4.10}$$

The main difference with the models from the literature is that the function $\mathcal{F}^{(i)}$ does not only depend on what happens in the considered direction $\mathbf{a}_0^{(i)}$ but also on the global elongational energy in the material, i.e., $\mathcal{I}$ and $\mathcal{G}$. Then, different forms can be proposed.

In this paper, the concept of double-network is employed similarly to the work of (Beatty and Krishnaswamy, 2000), and some hypothesis on the $\mathcal{F}^{(i)}$ definition must be established. During a first loading for the material, i.e., $\mathcal{I} = \mathcal{G}$ the function $\mathcal{F}^{(i)}$ should not evolve, that means that

$$\mathcal{F}(\mathcal{M}^{(i)}, \mathcal{M}_{\max}^{(i)}, \mathcal{I} = \mathcal{G}, \mathcal{G}) = 1 \tag{4.11}$$

Moreover, if the material is stretched in a given direction for the first time, the function $\mathcal{F}^{(i)}$ should not evolve in this direction whatever is the deformation level in this direction as well as the global deformation state, thus

$$\mathcal{F}(\mathcal{M}^{(i)} = \mathcal{M}_{\max}^{(i)}, \mathcal{M}_{\max}^{(i)}, \mathcal{I}, \mathcal{G}) = 1 \tag{4.12}$$

That means that during a first loading curve the function $\mathcal{F}^{(i)}$ does not intervene (i.e. $\mathcal{F}^{(i)} = 1$) and the energy density is simply hyperelastic. However, during a second loading curve the function evolves in the interval given by

$$\mathcal{F}(\mathcal{M}^{(i)}, \mathcal{M}_{\max}^{(i)}, \mathcal{I}, \mathcal{G}) \in [0, 1] \tag{4.13}$$

Considering the deformation of the material as a thermodynamic process, the double network approach establishes that the evolution function depends on the difference between the maximum instantaneous state and the maximum state achieved along the history. In an anisotropic approach, it is possible to decompose this contribution according to the maximum principal value and according to each direction. Moreover, the amount of stress-softening is directly linked to the orientation of the loading, the ratio of what happens in each direction compared to the maximum deformation should be taken into account. In this way, a general form is proposed as follow

$$\mathcal{F} = 1 - \mathcal{F}_1(\mathcal{G} - \mathcal{I}) \ \ \mathcal{F}_2(\mathcal{M}_{\max}^{(i)} - \mathcal{M}^{(i)}) \ \ \mathcal{F}_3\left(\frac{\mathcal{M}_{\max}^{(i)}}{\mathcal{G}}\right) \tag{4.14}$$

where $\mathcal{F}_1$, $\mathcal{F}_2$ and $\mathcal{F}_3$ are functions to be determined. The conditions evoked in Eqs. (4.11) and (4.12) lead to

$$\mathcal{F}_1(\mathcal{G} - \mathcal{I}) = 0 \quad \text{if} \quad \mathcal{G} = \mathcal{I} \tag{4.15}$$

$$\mathcal{F}_2(\mathcal{M}_{\max}^{(i)} - \mathcal{M}^{(i)}) = 0 \quad \text{if} \quad \mathcal{M}_{\max}^{(i)} = \mathcal{M}^{(i)}. \tag{4.16}$$

Now, different constitutive equation forms can be proposed for each function $\mathcal{F}_1$, $\mathcal{F}_2$ and $\mathcal{F}_3$ in Eq. (4.14).

4.4 First anisotropic modeling constitutive equation

4.4.1 Hyperelastic constitutive equation

The advantage of such formulation is that the first loading curve is independent of the evolution function on the contrary of damage mechanics (Lemaitre and Chaboche, 1990).

Thus, the choice of the hyperelastic energy only depends on the first loading curves. In a first approach, it is proposed to use the classical Mooney (1940) constitutive equation to represent the isotropic energy density, then

$$\mathcal{W}_{cc} = C_1(I_1 - 3) + C_2(I_2 - 3) \tag{4.17}$$

For the anisotropic part of the constitutive equation, the classical centrally symmetric 2×21 scheme was chosen to represent the material directions (Bazant and Oh, 1986). The vector and weight of each direction are re-called in Appendix B. All the other direction distribution schemes could also be used. For a comparative study between different numerical integration schemes, see Ehret *et al.* (2010).

The non-Gaussian theory is classically used to capture the anisotropy. Diani *et al.* (2006a) and Dargazany and Itskov (2009) use the Langevin chain representation for $\mathcal{W}_{cf}^{(i)}$ energy. The great advantage of this choice is that it brings physical understanding to the modeling and it presents two main consequences. The first one is that the zero-stress state is only ensured by the compensation of all the directions contribution as $\partial\mathcal{W}(\lambda^{(i)})/\partial\lambda^{(i)} \neq 0$ if $\lambda^{(i)} = 1$. Hence, this formulation could hardly be used for an initially non-isotropic material. In the second, this choice permits to capture an important permanent deformation of the material after a loading cycle. However, in filled silicone experiments, it was shown that the permanent deformation is quite negligible. For this purpose, the classical approach of hyperelastic anisotropy approach using the anisotropic strain invariant $I_4^{(i)} = \mathbf{a}_0^{(i)} \cdot \mathbf{C}\,\mathbf{a}_0^{(i)}$ is used, where $\mathbf{C} = \mathbf{F}^T\mathbf{F}$ is the right Cauchy-Green strain tensor. The function should verify the following conditions

$$\mathcal{W}_{cf}^{(i)}(I_4^{(i)}) \quad = \quad 0 \quad \text{if} \quad I_4^{(i)} = 1 \tag{4.18}$$

$$\frac{\partial\mathcal{W}_{cf}^{(i)}(I_4^{(i)})}{\partial I_4^{(i)}} \quad = \quad 0 \quad \text{if} \quad I_4^{(i)} = 1. \tag{4.19}$$

In a first approach, an ordinary constitutive equation is used, considering that the chains are only stretched by tensile stresses. In otherwise, compressive stretches lead to buckling of the chains. Thus, one may write

$$\mathcal{W}_{cf}^{(i)} = K^{(i)}\left(I_4^{(i)} - 1\right)^2 \quad \text{if} \quad I_4^{(i)} \geq 1 \quad \text{else} \quad 0. \tag{4.20}$$

This formulation can be adapted to non-initially isotropic material by choosing different functions for $\mathcal{W}_{cf}^{(i)}$. As the filled silicone rubber is initially isotropic, every $\mathcal{W}_{cf}^{(i)}$ is initially the same in all directions, i.e., $\forall i, j \;\; K^{(i)} = K^{(j)}$.

4.4.2 Stress softening constitutive equation

In part 4.3.3, a multiplicative decomposition was postulated in Eq. (4.14). The use of simple power functions, for $\mathcal{F}_1$, $\mathcal{F}_2$ and $\mathcal{F}_3$, is proposed to represent the stress softening, given by

$$\mathcal{F}^{(i)} = 1 - \eta\sqrt{\frac{\mathcal{G} - \mathcal{I}}{\mathcal{G}}}\sqrt{\frac{\mathcal{M}_{\max}^{(i)} - \mathcal{M}^{(i)}}{\mathcal{G}}}\left(\frac{\mathcal{M}_{\max}^{(i)}}{\mathcal{G}}\right)^2 \tag{4.21}$$

where η is a material parameter. The functions $\mathcal{F}_1$ and $\mathcal{F}_2$ are normalized according to the maximum elongational energy $\mathcal{G}$ to ensure a normalized evolution function for each second loading curve. It is important to note that, even if the objective is to describe Mullins effect anisotropy, the constitutive equation for stress-softening only depends on one parameter η. All the other parameters describe the hyperelastic first loading. The evolution functions have the same form in all directions, but this approach could be extended to non-isotropic material by defining different values for the parameter η in the different directions.

4.4.3 Comparison of the modeling with experimental data

The model is fitted on all the experimental data presented in Machado *et al.* (2010, 2011a), i.e., tests where the principal stretch directions remain unchanged during first and second load or tests where the principal stretch directions are not necessarily the same during first and second loads. First, the parameters of the hyperelastic constitutive equations are fitted on the different first loading curves. Different parameters can be chosen according to the repartition of the elongational energy between $\mathcal{W}_{cc}$ and $\mathcal{W}_{cf}$.

Considering a second tensile loading immediately before the sample rupture, the most stress softening level is obtained and this state corresponds to the elongational energy of chains that were not affected by the Mullins effect. Thus, to ensure a good balance between $\mathcal{W}_{cc}$ and $\mathcal{W}_{cf}$ the portion $\mathcal{W}_{cc}$, i.e., the Mooney model, is fitted on the beginning of the second tensile loading curve at the higher deformation achieved.

Next, the part of $\mathcal{W}_{cf}$ is fitted to complete the stress amount. The fitted parameters are presented in Table 4.1. The simulations of the first loading curve are illustrated in Fig. 4.2. It appears that the model describes perfectly uniaxial and pure shear tests whereas equibiaxial tests are underestimated.

Table 4.1: Values of the constitutive equation parameters

Parameter	Value
C_1	0.05 MPa
C_2	0.03 MPa
$\forall i \quad K^{(i)}$	0.10 MPa
η	2.0

The last parameter that describes the stress-softening is fitted on the second loading curves for all the tests, the value $\eta = 2.0$ is obtained. The condition in Eq. (4.13) must be satisfied, and as explained the function $\mathcal{F}^{(i)}$ cannot be negative. If its softening is too large, i.e., $\mathcal{F}^{(i)} < 0$, the value $\mathcal{F}^{(i)} = 0$ is imposed. That means that in the considered direction a great number of chain–filler links were broken. In the second load, for the same direction, the suspended chains are no longer acting enough to impose a force at the macromolecular network.

The simulations of the cyclic uniaxial tensile, pure shear and equibiaxial tensile tests are presented in Fig. 4.2 and it appears that the model describes quite well all these tests. However, the equibiaxial stress is underestimated, presenting the same deviation as previously quoted. This phenomenon is due to the hyperelastic equation and not to stress softening equation. As pointed out by Marckmann and Verron (2006) and Boyce and Arruda (2000), there are very few hyperelastic constitutive models able to simultaneously simulate both multi-dimensional data with a unique set of material parameters. Even if the first loading curve is underestimated, the form of the stress softening is well described.

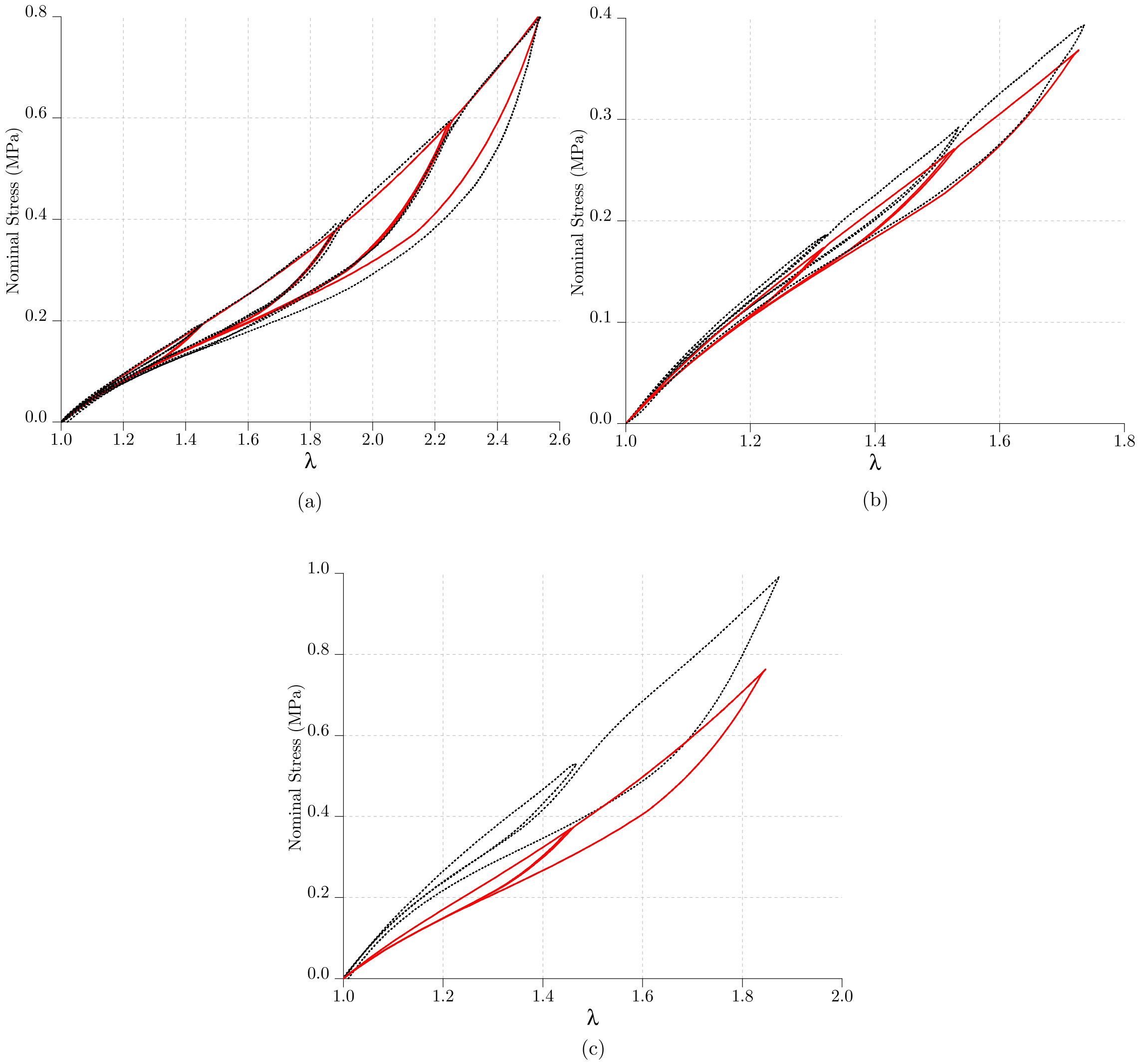

Figure 4.2: Comparison of the model (solid lines) with experimental data from Machado *et al.* (2010) (dotted lines) for: (a) cyclic uniaxial tensile test, (b) cyclic pure shear test and (c) cyclic equibiaxial test.

Next, tensile tests with a change of loading direction between the first and second loads are confronted. A simulation of the modeling is presented in Fig. 4.3(a). It appears that the trend is exactly what is presented in Machado *et al.* (2011a). All the second loading curves come back on the same point of the first loading curve and the amount of stress softening is directly linked to the angle between the principal stretch directions of the first and second loads. A detailed comparison with experimental data is presented in Fig. 4.3(b-f). The model does not superpose perfectly experimental data, but all trends are quite well described.

To finish, the model is used to simulate BT tests, the first load being a biaxial test and the second load being a tensile test. The comparison of the second loading curves is presented in Fig. 4.4. It appears that stress softening is moderately overestimated by the model, however the come-back on the first loading curve is perfectly described.

All these simulations emphasize that the use of this new elongation energy measure is a good point to describes the come back of the second loading curve on the virgin one. The amount of stress-softening is well described for cyclic loading experiments and for TT tests, where the principal stretch directions were not the same during first and second loads. Nevertheless, the stress softening during BT test is overestimated.

It can be noticed that the model describes correctly all the experimental tests with a simple constitutive equation which only depends on one parameter. Evidently, the results can be improved by proposing more complex constitutive equations, that consequently would lead to a significant increase in the number of parameters. Nevertheless, the presented results allowed to demonstrate the efficiency of this new approach.

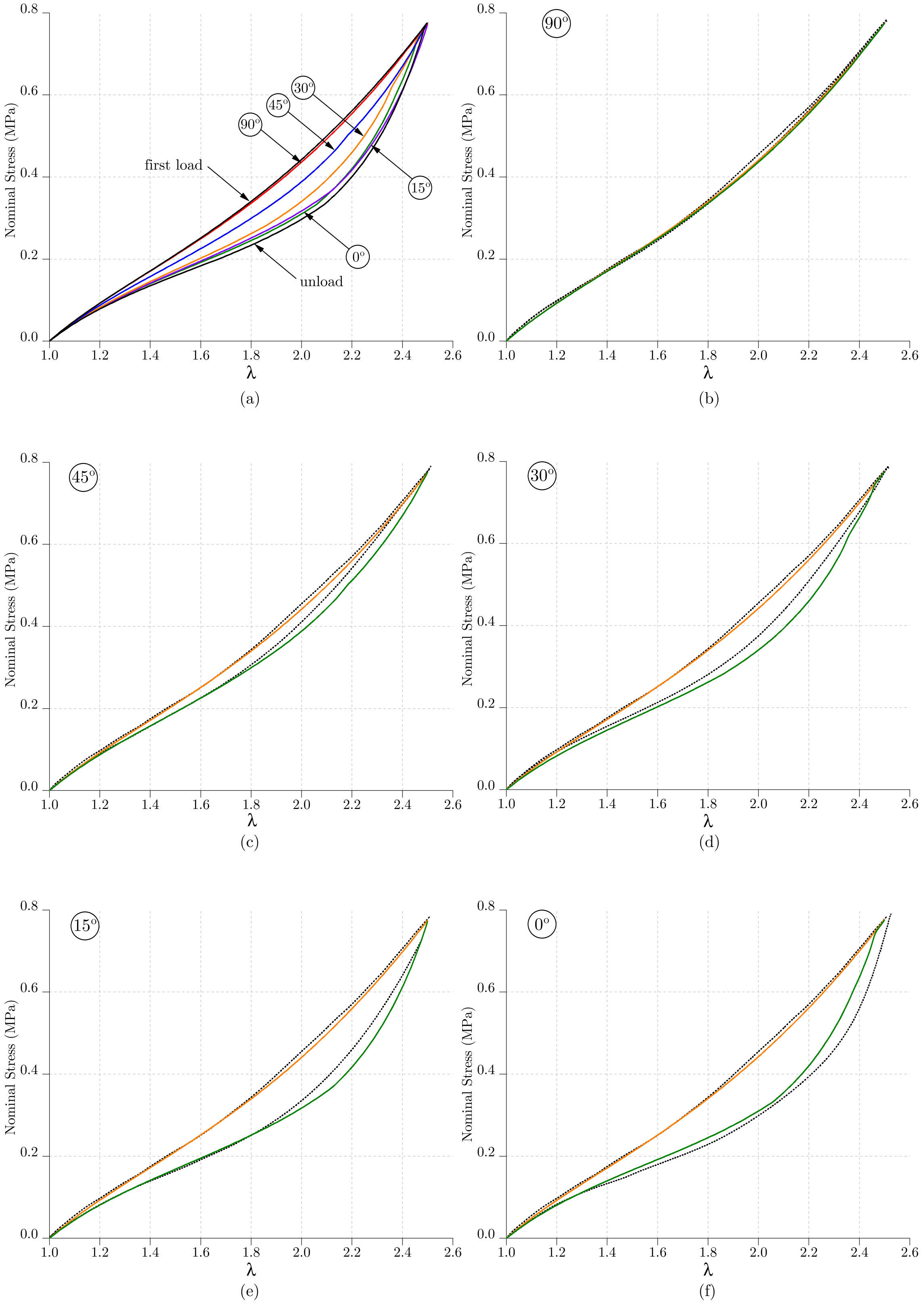

Figure 4.3: Comparison of the model (solid lines) with TT uniaxial pre-stretching experimental data (dotted lines). (a) simulation of the model for different orientations of the second load. Details of the experimental (dotted lines) and modeled (solid lines) first and second load curves with an angle between stretch direction of: (b) 90°, (c) 45°, (d) 30°, (e) 15° and (f) 0°.

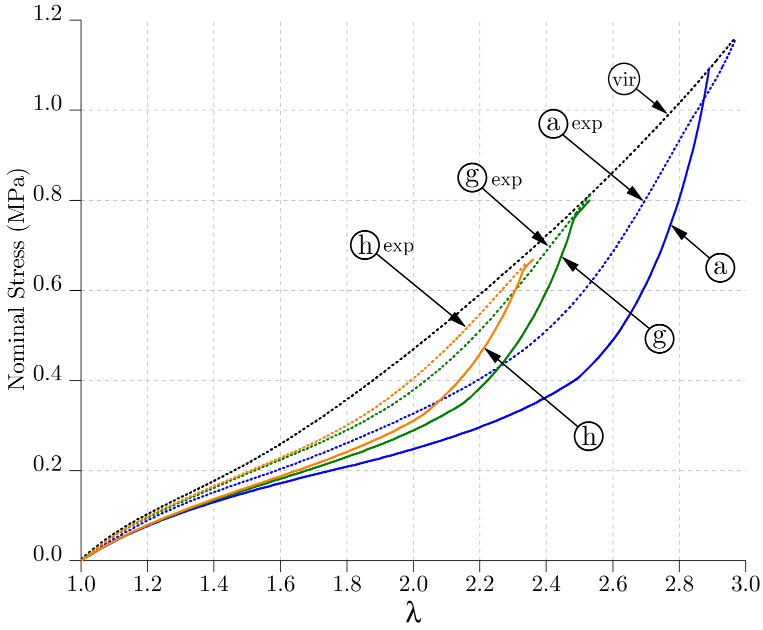

Figure 4.4: Comparison of the model (solid lines) with BT biaxial pre-stretching experimental data (dotted lines). Curve a simulation of the model for the second tensile load after an equibiaxial test; curve g simulation of the model for the second load after a biaxial test of biaxiality ratio $\mu = 0.7$; curve h simulation of the model for the second load after a biaxial test of biaxiality ratio $\mu = 0.5$

4.5 Conclusion

The present paper presents an original approach to model the stress induced anisotropy by the Mullins effect, by the definition of a tensor to measure the repartition of the elongational energy in space. The comparison of the elongational energy in different directions with the principal maximal elongational energy permits to create a new formulation for stress softening modeling. In this approach, the constitutive equation is written in function of the variation of elongational energy in each direction and the variation of elongational energy in the maximal principal direction. This new approach captures the principal characteristics of the Mullins effect underlined in literature. This new means to describe Mullins effect anisotropy can be a good starting point to elaborate new constitutive equations.

In this paper, a simple constitutive equation to describe the stress softening evolution was proposed, depending on only one parameter. It clearly appears that the results are quite encouraging for a model that can describe many different experimental tests, whit very different strain histories, with only one parameter. Of course, the agreement with the experimental data can be improved by using more sophisticated constitutive equation forms.

Chapter

5

Finite element numerical implementation

In a typical implicit finite element analysis of a nonlinear boundary-value problem, global Newton-type iterative schemes necessitate the computation of the tangent modulus being consistent with the numerical scheme used for the update of the internal variables. In this context the constitutive equations proposed in Chapter 4 were simplified to facilitate the implementation into a finite element code via a user-defined material subroutine. The Abaqus software was chosen for the proposed implementation.

Contents

5.1 Introduction

The next sections briefly outline the principal equations of nonlinear continuum mechanics that describe the fundamental geometric mappings and balance equations of a solid body undergoing finite deformations. Apart from the reiteration of some basic relations in continuum mechanics, it is also aimed to introduce the notation and terms used in the numerical implementation. The following is based on the books of Bonet and Wood (1997), Basar and Weichert (2000), De Souza Neto *et al.* (2008), and Holzapfel (2000).

5.2 Motion and deformation

Considering a general structural problem described by the initial configuration Ω_0 of the structure at time t_0. The material particle initially located at some position $\mathbf{X} \in \Omega_0$ in space moves to a new position $\mathbf{x} \in \Omega$ in the current configuration Ω at time t. Under the postulate of conservation of mass, there is a one-to-one (and hence invertible) correspondence between $\mathbf{X}$ and $\mathbf{x}$, so is possible to define the motion as

$$\mathbf{x} = \varphi(\mathbf{X}, t), \qquad \text{with } \mathbf{X} = \varphi^{-1}(\mathbf{x}, t) \tag{5.1}$$

Now consider two neighboring particles, located at $\mathbf{X}$ and at $\mathbf{X} + d\mathbf{X}$ in the initial configuration. In the current configuration, it follows that

$$\mathbf{x} + d\mathbf{x} = \varphi\left(\mathbf{X} + d\mathbf{X}, t\right). \tag{5.2}$$

Assuming that, for each time t, the mapping $\varphi(\bullet)$ is smooth, Eq. (5.2) can be expanded in a Taylor series as

$$\mathbf{x} + d\mathbf{x} = \varphi(\mathbf{X}, t) + \frac{\partial \varphi(\mathbf{X}, t)}{\partial \mathbf{X}} d\mathbf{X} + \mathcal{O}(d\mathbf{X}^2). \tag{5.3}$$

Subtracting 5.3 from 5.1, and neglecting the higher order terms ($\mathcal{O}$), one may write

$$d\mathbf{x} = \frac{\partial \varphi\left(\mathbf{X}, t\right)}{\partial \mathbf{X}} d\mathbf{X} = \mathbf{F}\left(\mathbf{X}, t\right)\, d\mathbf{X}. \tag{5.4}$$

with $\mathbf{F}$ denoting the gradient, on the reference configuration, of the deformation function φ, i.e., $\mathbf{F} = Grad(\mathbf{x})$.

5.3 The initial boundary-value problem

The finite element method requires the formulation of balance laws in the forms of variational principles in order to provide approximate solutions for the underlying initial boundary-value problem. Good approximate solutions are often related to the weak forms of field equations, which are consequences of the stationary condition of the functional.

5.3.1 Strong formulation

Considering only mechanical variables, given the body force, and the boundary and initial conditions, find the displacement $\mathbf{u}(\mathbf{X}, t) = \mathbf{x}(\mathbf{X}, t) - \mathbf{X}$, so that

$$\begin{aligned}
div(\boldsymbol{\sigma}) + \mathbf{q} &= \rho \ddot{\mathbf{u}} && (5.5)\\
\mathbf{u} &= \hat{\mathbf{u}} \quad \text{on } \Omega_u && (5.6)\\
\mathbf{t} &= \boldsymbol{\sigma}\mathbf{n} = \hat{\mathbf{t}} \quad \text{on } \Omega_t && (5.7)\\
\mathbf{u}(\mathbf{x}, 0) &= \mathbf{u}_0(\mathbf{X}) && (5.8)\\
\dot{\mathbf{u}}(\mathbf{x}, 0) &= \dot{\mathbf{u}}_0(\mathbf{X}) && (5.9)
\end{aligned}$$

where $\mathbf{q}$ and $\mathbf{t}$ are the volume forces per unit deformed volume and surface forces, acting upon the boundary surface, per unit deformed area. The body density in deformed configuration is given by $\rho = \rho(\mathbf{x}, t)$. The over-hat $(\hat{\bullet})$ symbol denotes prescribed functions on the boundaries $\partial\Omega_{(\bullet)}$. $\partial\Omega$ defines the boundary surface of a continuum body occupying region Ω. It is decomposed in disjoint parts so that

$$\partial\Omega_u \cap \partial\Omega_t = \emptyset \quad \text{and} \quad \partial\Omega_u \cup \partial\Omega_t = \partial\Omega. \tag{5.10}$$

The set of equations (5.5 to 5.9) defines the nonlinear initial boundary-value problem for the unknown displacement field $\mathbf{u}$, where Eq. (5.5) is the Cauchy's first equation of motion, governed by the symmetry condition $\boldsymbol{\sigma} = \boldsymbol{\sigma}^T$. This symmetry is a result of the balance of angular momentum. Nevertheless, as a consequence of the axiom of momentum balance, the dependence of the surface force $\mathbf{t}$ upon the normal vector $\mathbf{n}$ is linear. Finally, equations (5.5 to 5.9) are required in order to achieve compatibility of the boundary and initial conditions on $\partial\Omega_u$

5.3.2 Two-field Variational Principles

A numerical analysis of nearly incompressible and incompressible materials necessitates the so called multi-field variational principles in which additional variables are incorporated. Considering an elastic energy density given by the decomposition

$$\mathcal{W} = \bar{\mathcal{W}}(\bar{\mathbf{C}}) + \mathcal{U}(J) \tag{5.11}$$

where the function $\bar{\mathcal{W}}$ characterizes the isochoric elastic response of the hyperelastic material with corresponding modified right Cauchy-Green tensor $\bar{\mathbf{C}} = J^{-\frac{2}{3}}\mathbf{C}$, and $\mathcal{U}$ represents the volumetric energy in function of the volume ratio $J = (\det \mathbf{C})^{\frac{1}{2}}$. In the following, the over-bar $(\bar{\bullet})$ symbol denotes isochoric part of $(\bullet)$. Utilizing p as the Lagrange multiplier to enforce the incompressibility constraint $J = 1$, it is possible to formulate, in material description, a functional Π_L in the decoupled representation

$$\Pi_L(\mathbf{u}, p) = \Pi_{int}(\mathbf{u}, p) + \Pi_{ext}(\mathbf{u}) \tag{5.12}$$

with

$$\Pi_{int}(\mathbf{u}, p) = \int_{\Omega_0} \left[\bar{\mathcal{W}}(\bar{\mathbf{C}}(\mathbf{u})) + p(J(\mathbf{u}) - 1)\right] dV \tag{5.13}$$

where the term $p(J(\mathbf{u}) - 1)$ denotes the Lagrange multiplier term, and p is the physical hydrostatic pressure. For simplicity, the following development assumes that loads do not depend on the motion of the body, i.e., $\Pi_{ext}(\mathbf{u})$ is a linear function of $\mathbf{u}$, then one obtains

$$\Pi_{ext}(\mathbf{u}) = -\int_{\Omega_0} \mathbf{q}_0 \cdot \mathbf{u}\, dV - \int_{\Omega_0} \hat{\mathbf{t}}_0 \cdot \mathbf{u}\, dV. \tag{5.14}$$

In addiction to the virtual displacement field $\delta\mathbf{u}$, an arbitrary smooth scalar function $\delta p(\mathbf{x}) = \delta p(\varphi(\mathbf{X})) = \delta p(\mathbf{X})$ is needed, it is interpreted as the virtual pressure field. Using the Gâteaux derivate D, the stationary conditions with respect to $\mathbf{u}$ and p are given by

$$D_{\delta\mathbf{u}}\Pi_L(\mathbf{u}, p) = 0 \quad \text{and} \quad D_{\delta p}\Pi_L(\mathbf{u}, p) = 0 \tag{5.15}$$

for all $\delta\mathbf{u} = \mathbf{0}$ on the boundary surface $\partial\Omega_{0_u}$ and all δp. By means of straightforward tensor manipulations, one can easily establish that

$$D_{\delta\mathbf{u}}\Pi_L(\mathbf{u}, p) = \int_{\Omega_0} \left[2\frac{\partial\bar{\mathcal{W}}(\bar{\mathbf{C}}(\mathbf{u}))}{\partial\mathbf{C}} + p\,J(\mathbf{u})\,\mathbf{C}^{-1}(\mathbf{u}) \right] : \delta\mathbf{E}(\mathbf{u})\;dV + \Pi_{ext}(\mathbf{u}) = 0 \quad (5.16)$$

where

$$\bar{\mathbf{S}} = 2\frac{\partial\bar{\mathcal{W}}(\bar{\mathbf{C}}(\mathbf{u}))}{\partial\mathbf{C}} \quad (5.17)$$

$$\mathbf{S}^{vol} = p\,J(\mathbf{u})\,\mathbf{C}^{-1}(\mathbf{u}) \quad (5.18)$$

are respectively the isochoric and volumetric parts of the second Piola-Kirchhoff stress tensor $\mathbf{S}$. The Green-Lagrange strain tensor is denoted by $\mathbf{E} = \frac{1}{2}(\mathbf{C} - \mathbf{I})$.

On the other hand, the directional derivative in the direction of an arbitrary virtual pressure δp, is given by the weak form

$$D_{\delta p}\Pi_L(\mathbf{u}, p) = \int_{\Omega_0} (J(\mathbf{u}) - 1)\delta p\;dV = 0. \quad (5.19)$$

As can be seen, the pressure variable p maintains the incompressibility constraint and the associated equilibrium equations is find to be $J = 1$. The variational equations (5.16 and 5.19) provide the fundamental basis for a finite element implementation. They lead to mixed or hybrid methods on the interpolation functions for finite element method. The choice of these functions is a crucial task in order to alleviate volumetric locking. It was observed that discontinuous constant pressure and continuous displacement interpolation over a typical element domain is computationally more efficient than the choice of functions of the same order for $\mathbf{u}$ and p (Abaqus Manual, 2010).

5.3.3 Linearization of the Lagrange multiplier method

In theoretical continuum mechanics, the concept of linearization is essential in the derivation of linear approximations to general nonlinear theories. In computational mechanics, on the other hand, the interest in linearization stems mostly from the fact that numerical solutions to nonlinear problems are usually obtained by algorithms which require the solution of a sequence of linearized (or approximately linearized) problems. A typical example is the well-known Newton-Raphson iterative scheme, which is extensively exploited in the finite element framework.

In order to solve the nonlinear equations (5.16) and (5.19) for the two independent variables $\mathbf{u}$ and p using a interactive solution technique, essentially the second variation of Eq. (5.12) is required in the direction of the increments $\Delta\mathbf{u}$, Δp. Then, starting with the Δp direction, one obtains

$$D^2_{\delta u,\Delta p}\Pi_L(\mathbf{u}, p) = \int_{\Omega_0} J(\mathbf{u})\,\Delta p\,\mathbf{C}^{-1}(\mathbf{u})\colon \delta\mathbf{E}(\mathbf{u})\;dV = \int_{\Omega_0} J(\mathbf{u})\,\Delta p\,Div(\delta\mathbf{u})\;dV \quad (5.20)$$

$$D^2_{\delta p,\Delta p}\Pi_L(\mathbf{u}, p) = 0 \quad (5.21)$$

while the linearization in the $\Delta\mathbf{u}$ direction, leads to

$$D^2_{\delta u,\Delta\mathbf{u}}\Pi_L(\mathbf{u}, p) = \int_{\Omega_0} Grad(\delta\mathbf{u})\colon Grad(\Delta\mathbf{u})\,\mathbf{S} + \mathbf{F}^T Grad(\delta\mathbf{u})\colon \mathbb{C}^{\,L}\colon \mathbf{F}^T\,Grad(\Delta\mathbf{u})\;dV$$

(5.22)

$$D^2_{\delta p,\Delta\mathbf{u}}\Pi_L(\mathbf{u},p) = \int_{\Omega_0} J(\mathbf{u})\, Div(\Delta\mathbf{u})\, \delta p\; dV \tag{5.23}$$

The structure of Eqs. (5.20 to 5.23) is symmetric, hence a finite element implementation of this set of equations leads to a symmetric tangent stiffness matrix. Since Eq.(5.16) is based on the additive decomposition of the stresses $\mathbf{S}$ the decoupled representation of the Lagrangian elasticity tensor $\mathbb{C}^{\,L} = \bar{\mathbb{C}}^{\,L} + \mathbb{C}^{\,L}_{vol}$ is obtained, split into deviatoric $\bar{\mathbb{C}}^{\,L}$ and pressure components $\mathbb{C}^{\,L}_{vol}$, as

$$\bar{\mathbb{C}}^{\,L} = 2\frac{\partial\bar{\mathbf{S}}}{\partial\mathbf{C}} = 4\frac{\partial^2\bar{\mathcal{W}}}{\partial\mathbf{C}^2} \tag{5.24}$$

$$\mathbb{C}^{\,L}_{vol} = 2\frac{\partial\mathbf{S}^{vol}}{\partial\mathbf{C}} = J\frac{\partial\mathcal{U}}{\partial J}\left[\mathbf{C}^{-1}\otimes\mathbf{C}^{-1} + 2\frac{\partial\mathbf{C}^{-1}}{\partial\mathbf{C}}\right] + J^2\frac{\partial^2\mathcal{U}}{\partial J^2}\mathbf{C}^{-1}\otimes\mathbf{C}^{-1} \tag{5.25}$$

where the arguments have been omitted. Note that the pressure component $\mathbb{C}^{\,L}_{vol}$ does not depend on the particular material definition. The last term in Eq. (5.25) is usually called the volumetric tangent component.

5.4 Finite element implementation

5.4.1 The user-defined material subroutine

Several commercial finite element packages provide a facility for user-defined material models and the advantages of each software is not discussed in this work. The Abaqus software was used in this work as a matter of availability. It may, therefore, be useful to start with a brief outline of the way that Abaqus handles such models.

The equation of motion together with the constitutive law define a system consisting of an initial boundary problem and an ordinary differential equation. The equation of motion is solved with the help of a finite-element package (Abaqus–Standard), and the constitutive law by a solver for ordinary differential equations. The relevant constitutive information is passed to Abaqus by a subroutine UMAT which has to be supplied by the user. Considering a problem in large transformations with both, geometric and material nonlinearities, the problem must be time discretized and calculations performed using successive time steps in an implicit integration scheme. Abaqus–Standard (Abaqus Manual, 2010) uses an implicit integration method and the package operates by solving the following differential equation

$$\delta\boldsymbol{\tau} = J(\mathbb{C} : \delta\mathbf{D} + \delta\mathbf{W}\,\boldsymbol{\sigma} + \boldsymbol{\sigma}\,\delta\mathbf{W}^T) \tag{5.26}$$

where $\boldsymbol{\tau} = J\boldsymbol{\sigma}$ is the Kirchhoff stress tensor, $\mathbb{C}$ is the consistent tangent modulus (which Abaqus calls the Jacobian), $\delta\mathbf{D}$ is the virtual rate of deformation and $\delta\mathbf{W}$ is the virtual spin tensor.

Essentially, the UMAT must provide consistent tangent modulus, i.e., the tangent modulus of a discretized constitutive relation. With the knowledge of the consistent tangent modulus, it is possible to update the stresses and solution-dependent state variables to their values at the end of the increment for which it is called. The precise information on the tangent modulus is essential to achieve fast convergence in Newton-type iteration performed by Abaqus. Table 5.1 summarizes the UMAT/Abaqus data flow. The main interactions between Abaqus and the UMAT, are given by the following steps:

- Step 1: starting from an equilibrium at time t_n, Abaqus performs an incremental loading. At an equilibrium time t_n, Abaqus supplies the stress at the start of the increment $\boldsymbol{\sigma}^n$, the strain at the start of increment $\mathbf{F}^n$, the trail strain increment $\Delta\mathbf{F}^n_{trial}$ and the time period for the increment Δt;
- Step 2: the user subroutine UMAT has to supply Abaqus with new stress tensor $\boldsymbol{\sigma}^{n+1} = \boldsymbol{\sigma}^n + \Delta\boldsymbol{\sigma}^n$ updated according to the constitutive law as well as with the derivative of stress with respect to the strain increment;
- Step 3: strain update $\mathbf{F}(t_n + \Delta t) = \mathbf{F}(t_n) + \Delta\mathbf{F}(t_n)$ by Abaqus;
- Step 4: with the above information, a new guess for the strain increment is calculated $\Delta\mathbf{F}^{n+1}$ and the whole procedure is iterated until convergence.

Table 5.1: The UMAT/Abaqus data flow. (Sands, 2009)

The UMAT receives (for every integration point):

(1) the stress at the start of the increment $\boldsymbol{\sigma}^n$;
(2) the strain at the start of the increment $\mathbf{F}^n$
(3) the strain increment $\Delta\mathbf{F}$;
(4) the time period for the increment Δt;
(5) the material properties;
(6) and the state variables related to the start of the increment.

The UMAT must return the following to Abaqus:

(1) the stress at the end of the increment $\boldsymbol{\sigma}^{n+1} = \boldsymbol{\sigma}^n + \Delta\boldsymbol{\sigma}^n$;
(2) the consistent tangent modulus $\mathbb{C}$;
(3) and the updated state variables related to the end of the increment.

Since in Abaqus a rate–form formulation is adopted, where the problem is defined through the variation in Kirchhoff stress, the equations of Section 5.3.3 are modified to take into account the new reference configuration. The updated Lagrange elastic tensor (Martin Borret, 1998) after some manipulations it is given by

$$\mathbb{C}^{\,Lr} = [\boldsymbol{\sigma} \circ \mathbb{S} + \mathbb{S} \circ \boldsymbol{\sigma}] + \frac{1}{J}\mathbf{F} \circ \left[\frac{\partial \mathbf{S}}{\partial \mathbf{E}} : (\mathbf{F}^T \circ \mathbb{S} \circ \mathbf{F})\right] \circ \mathbf{F}^T. \tag{5.27}$$

The two terms in the last equation are respectively the convection term and the transport term of the initial configuration to the current configuration, and it can be rewritten as:

$$\mathbb{C}^{\,Lr} = [\boldsymbol{\sigma} \circ \mathbb{S} + \mathbb{S} \circ \boldsymbol{\sigma}] + \frac{1}{J}\,\Phi_*\left[\mathbb{C}^{\,L}\right] = [\boldsymbol{\sigma} \circ \mathbb{S} + \mathbb{S} \circ \boldsymbol{\sigma}] + \frac{1}{J}\,\mathbb{C}^{\,e} \tag{5.28}$$

where Φ_* is the push–forward operation. Note that the $(\circ)$ symbol represents the contracted product, defined with respect to an orthonormal basis as

$$[\mathbb{A} \circ \mathbf{B}]_{ijkl} = A_{ipkl} B_{pj} \tag{5.29}$$

$$[\mathbf{B} \circ \mathbb{A}]_{ijkl} = B_{iq} A_{qjkl} \tag{5.30}$$

where $\mathbb{A}$ and $\mathbf{B}$ are fourth and second order generic tensors, respectively.

The updated Lagrangian elasticity tensor is therefore deduced from the calculation of the Lagrangian elasticity tensor and Eulerian stress tensor by Eq.(5.28). Thus, the implementation of a constitutive relation in Abaqus requires the calculation of Eulerian stresses and updated Lagrangian elasticity.

5.5 The anisotropic potential energy definition

In Chapter 4, the decomposition of the strain energy into a part that represents the energy density of the chains linked to filler ($\bar{\mathcal{W}}_{cf}$) and other part representing the energy density of the chains linked to other chains ($\bar{\mathcal{W}}_{cc}$) was proposed. Using a simple power function to represent the stress softening evolution ($\mathcal{F}^{(i)}$) for each direction i, demonstrates to be very efficient to represent the experimental data from different pre-conditioning methods. For convenience, the global stored energy and the evolution equation are then rewritten, respectively, as

$$\bar{\mathcal{W}}(\bar{I}_1, \bar{I}_2, \bar{I}_4) = C_1(\bar{I}_1 - 3) + C_2(\bar{I}_2 - 3) + \sum_{i}^{n} K^{(i)}\,(w_{I_4}^{(i)})\,\mathcal{F}^{(i)}\,(\bar{I}_4^{(i)} - 1)^2 \tag{5.31}$$

$$\mathcal{F}^{(i)} = 1 - \eta\sqrt{\frac{\mathcal{G} - \mathcal{I}}{\mathcal{G}}}\sqrt{\frac{\mathcal{M}_{\max}^{(i)} - \mathcal{M}^{(i)}}{\mathcal{G}}}\left(\frac{\mathcal{M}_{\max}^{(i)}}{\mathcal{G}}\right)^2. \tag{5.32}$$

Note that the evolution function depends on the maximum elongational energy in the direction $\mathbf{a}_0^{(i)}$ ($\mathcal{M}_{\max}^{(i)}$); the maximum elongational energy in any direction at the current time ($\mathcal{I}$); and the maximum stored energy in any direction over the history ($\mathcal{G}$). Considering a finite element interactive scheme, the time integration of these energy quantities requires a supplementary effort in the user-material numerical implementation. In fact, the stress cannot be directly calculated thanks to the deformation state as Mullins effect is governed by the stored energy, i.e., the strain and the stress states. An interactive scheme should be implemented which leads to a additional interaction loop in the software with all the linearization problem. An adaptation of the constitutive equation can simplify the implementation problem.

5.5.1 Modified stress softening constitutive equation

In order to obtain a more suitable constitutive equation for the numerical implementation into finite element code, a derived form from Eq. (5.32) is proposed. As can be seen in Eq. (5.31), the function energy $\bar{\mathcal{W}}$ has a first order dependence of the first invariant (I_1) and a second order dependence from the fourth invariant (I_4). Consequently, the energy measure is dependent of (I_1) and $(I_4)^2$ in the constitutive equation. Based on these observations, the local directional energies $\mathcal{M}^{(i)}$ are replaced for the $(I_4^{(i)})^2$ measures and the global energy measure $\mathcal{G}$ is replaced for linear dependence of I_1 our I_4 measure, keeping same balance between the terms ratio of the multiplicative form from Eq. (5.32). Thus, the simplified evolution equation is obtained as the following form

$$\mathcal{F}^{(i)} = 1 - \eta \sqrt{\frac{\bar{I}_{1\,\mathrm{max}} - \bar{I}_1}{\bar{I}_{1\,\mathrm{max}} - 3}} \left(\frac{\bar{I}^{(i)}_{4\,\mathrm{max}} - \bar{I}^{(i)}_4}{\bar{I}^{(i)}_{4\,\mathrm{max}} - 1} \right) \left(\frac{\bar{I}^{(i)}_{4\,\mathrm{max}}}{\bar{I}_{4\,\mathrm{max}}} \right)^4 \tag{5.33}$$

The model is fitted on all the experimental data of Machado *et al.* (2010, 2011a), using the same procedure employed to complete energy model from Chapter 4. Table 5.2 presents the material parameters. Note that, the parameters of the hyperelastic constitutive equations, fitted on the different first loading curves, are the same as for the complete energy model. This is expected since the first loading curve is independent of the evolution functions. The parameter that describes the stress-softening is fitted on the second loading curves for all the tests, the value $\eta = 4.0$ is obtained.

Table 5.2: Constitutive parameters for the simplified model.

Parameter	Value
C_1	0.05 MPa
C_2	0.03 MPa
$\forall i \quad K^{(i)}$	0.10 MPa
η	4.0

The simulations of the cyclic uniaxial tensile, pure shear and equibiaxial tensile tests are presented in Fig. 5.1. It appears that the model describes well the stress softening for all these tests. The simplified model predicts well uniaxial and pure shear tests whereas equibiaxial tests are underestimated. This phenomenon, as for the original model (Chapter 4), is expected since first loading depends on the hyperelastic equation and not on the stress evolution function.

The simplified model is now compared with the experimental data of the two preconditioning methods presented in Machado *et al.* (2011a). First, in Fig. 5.2, for tensile tests with a change of loading direction between the first and second loads. Results from the simplified model does not superpose exactly experimental data, but all trends are quite well described for different directions. Second, the simplified model results are compared with biaxial pre-stretching tests results. The comparison of the second loading curves is presented in Fig. 5.3. It appears that the stress softening is slightly overestimated but the return point on the first loading curve is perfectly described.

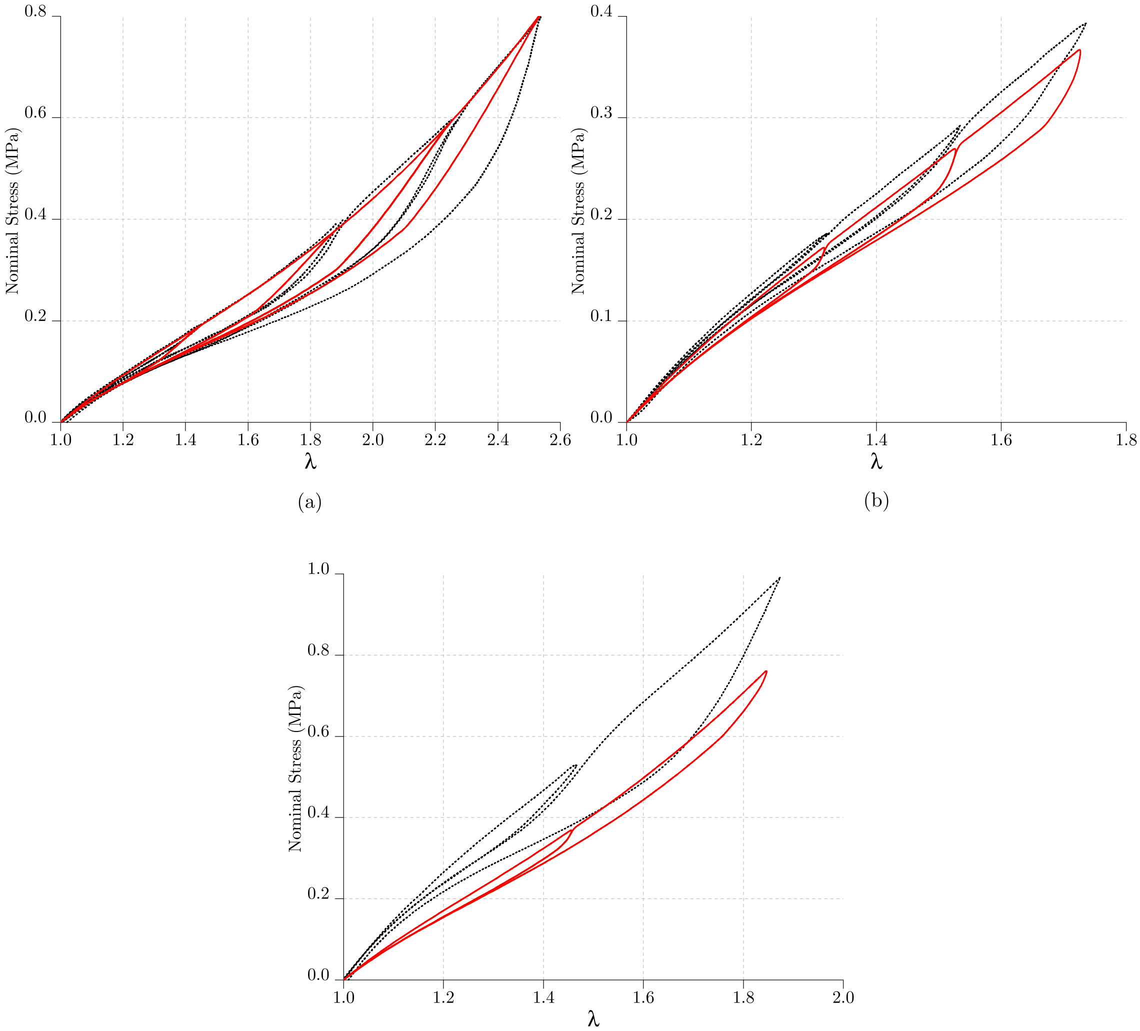

(a)

(b)

(c)

Figure 5.1: Comparison of the simplified model (solid lines) with experimental data (dotted lines) from Machado *et al.* (2011a) (a) cyclic uniaxial tensile test, (b) cyclic pure shear test (c) cyclic equibiaxial test.

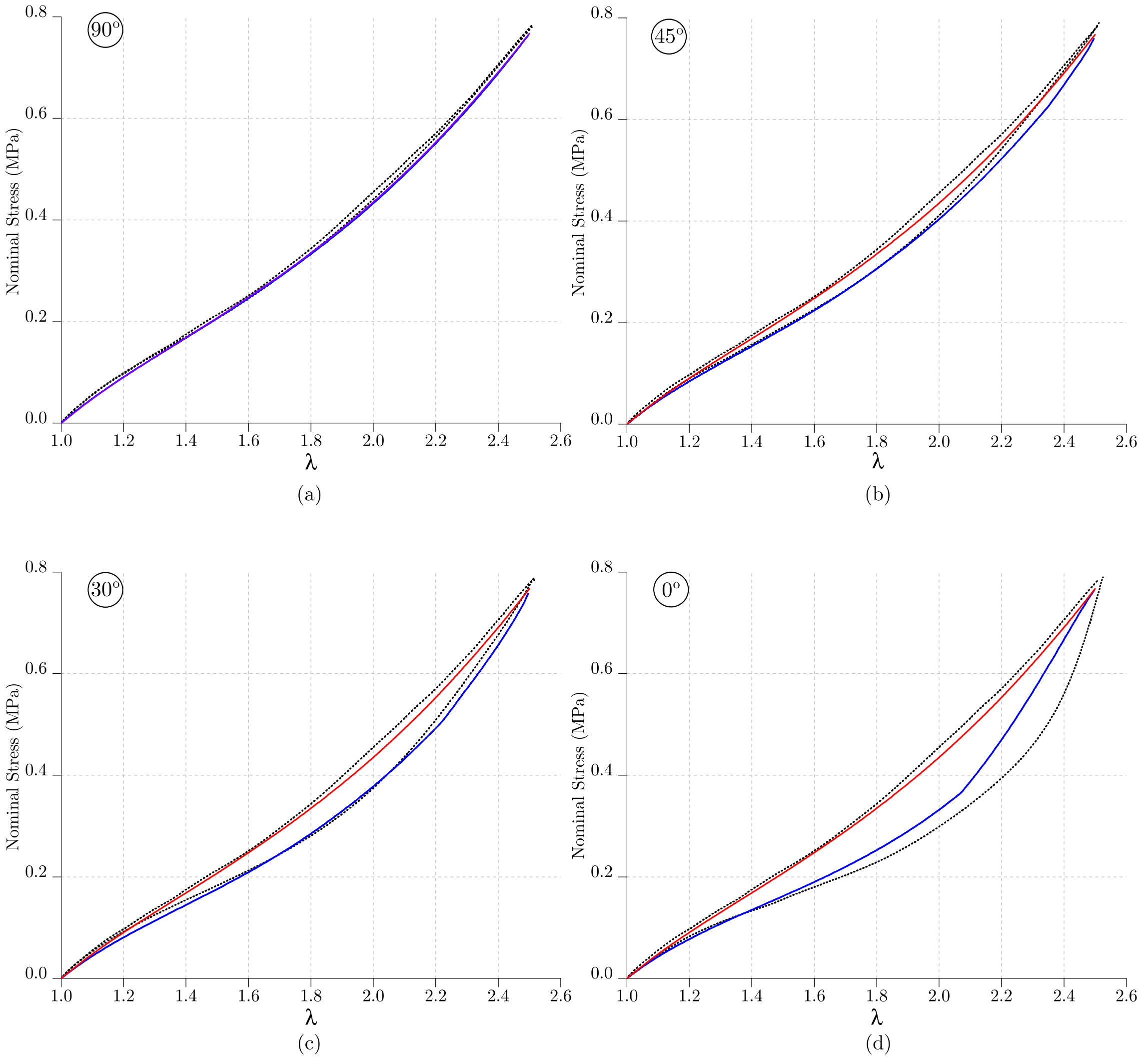

(a) (b)

(c) (d)

Figure 5.2: Comparison of the model with uniaxial pre-stretching experimental data (dotted lines). (a) Tensile test oriented at 0° (d) Tensile test oriented at 30° (e) Tensile test oriented at 45° (f) Tensile test oriented at 90°

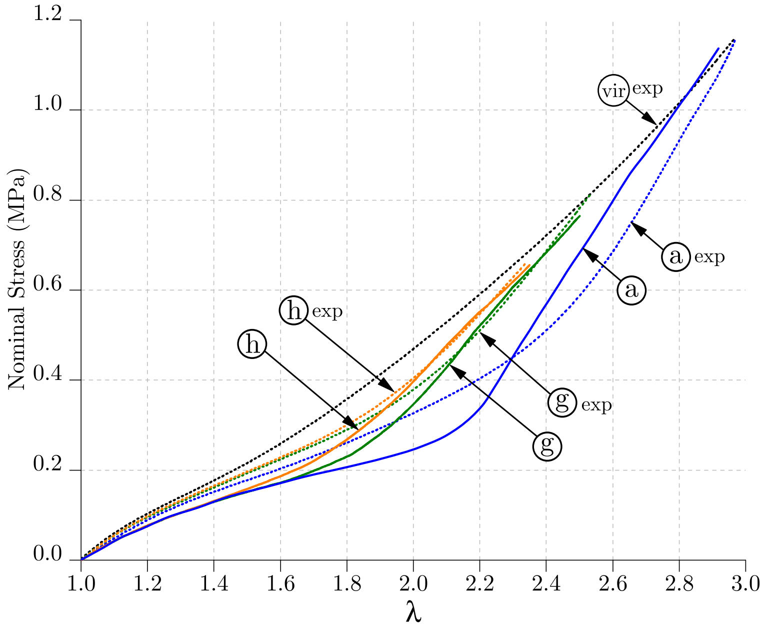

Figure 5.3: Comparison of the model (solid lines) with biaxial pre-stretching experimental data (dotted lines). Curve a simulation of the model for the second load after an equibiaxial test; curve g simulation of the model for the second load after a biaxial test of biaxiality rate $\mu = 0.7$; curve h simulation of the model for the second load after a biaxial test of biaxiality rate $\mu = 0.5$

5.5.2 Stress and tangent modulus calculation

Considering the simplified model proposed in the last section, the strain energy density depends on the first, second and fourth invariants, i.e., $\mathcal{W} = \mathcal{W}(I_1, I_2, I_4^{(i)})$. As aforementioned, the numerical implementation needs a quasi-incompressible formulation, thus the Eq. (5.11) is rewritten in terms of invariants as follows

$$\mathcal{W} = \bar{\mathcal{W}}(\bar{I}_1, \bar{I}_2, \bar{I}_4{}^{(i)}) + \mathcal{U}(J) \tag{5.34}$$

with $\bar{I}_1 = I_3^{-1/3} I_1$, $\bar{I}_2 = I_3^{-2/3} I_2$, $\bar{I}_3 = 1$ et $\bar{I}_4{}^{(i)} = I_3^{-1/3} I_4^{(i)}$. After the decomposition given in Eq. 5.34, the second Piola-Kirchhoff stress tensor is given by the strain energy derivation with respect to the right Cauchy-Green tensor, as

$$\mathbf{S} = \bar{\mathbf{S}} + \mathbf{S}^{vol} = 2\frac{\partial \bar{\mathcal{W}}}{\partial \mathbf{C}} + J\frac{\partial \mathcal{U}}{\partial J}\mathbf{C}^{-1}. \tag{5.35}$$

Developing the deviatoric stress term, one obtains

$$\bar{\mathbf{S}} = 2\left\{\frac{\partial \bar{\mathcal{W}}}{\partial \bar{I}_1}\frac{\partial \bar{I}_1}{\partial \mathbf{C}} + \frac{\partial \bar{\mathcal{W}}}{\partial \bar{I}_2}\frac{\partial \bar{I}_2}{\partial \mathbf{C}} + \sum_{i=1}^{n} \frac{\partial \bar{\mathcal{W}}}{\partial \bar{I}_4{}^{(i)}}\frac{\partial \bar{I}_4{}^{(i)}}{\partial \mathbf{C}}\right\} \tag{5.36}$$

and the Lagrangian deviatoric tangent modulus, is finally given by

$$\begin{aligned}
\bar{\mathbb{C}}^{\,L} &= 4\left\{\frac{\partial}{\partial \mathbf{C}}\left(\bar{\mathcal{W}}_{,1}\frac{\partial \bar{I}_1}{\partial \mathbf{C}}\right)+\frac{\partial}{\partial \mathbf{C}}\left(\bar{\mathcal{W}}_{,2}\frac{\partial \bar{I}_2}{\partial \mathbf{C}}\right)+\sum_{i=1}^{n}\frac{\partial}{\partial \mathbf{C}}\left(\bar{\mathcal{W}}_{,4}^{(i)}\frac{\partial \bar{I}_4{}^{(i)}}{\partial \mathbf{C}}\right)\right\} && \text{(5.37a)}\\
&= 4\left\{\mathbb{H}_{1}^{\,L}+\mathbb{H}_{2}^{\,L}+\sum_{i=1}^{n}\mathbb{H}_{4}^{\,(i)L}\right\} && \text{(5.37b)}
\end{aligned}$$

As aforementioned, the push–forward operation $\Phi_*\left[\bar{\mathbb{C}}^{\,L}+\mathbb{C}^{\,L}_{vol}\right]$ is necessary. Keeping in mind the push–forward relations Φ_*,

$$\begin{aligned}
\Phi_*(\mathbf{I}) &\longrightarrow \mathbf{B} && (5.38)\\
\Phi_*(\mathbf{C}^{-\mathbf{1}}) &\longrightarrow \mathbf{I} && (5.39)\\
\Phi_*(\mathbf{C}) &\longrightarrow \mathbf{B}^2 && (5.40)\\
\Phi_*\left(\frac{\partial \mathbf{C}^{-1}}{\partial \mathbf{C}}\right) &\longrightarrow -\mathbb{S}, \quad \text{where} \quad S_{ijkl}=\frac{1}{2}\left(\delta_{ik}\delta_{jl}+\delta_{il}\delta_{jk}\right)^{\dagger} && (5.41)\\
\Phi_*\left(\mathbf{a}_0\otimes\mathbf{a}_0\right) &\longrightarrow (\mathbf{a}\otimes\mathbf{a}) && (5.42)\\
\Phi_*\left(\mathbb{S}\right) &\longrightarrow \mathbb{S}^*, \quad \text{where} \quad S^*_{ijkl}=\frac{1}{2}\left(B_{ik}B_{jl}+B_{il}B_{jk}\right)^{\dagger} && (5.43)
\end{aligned}$$

one obtains, by means of straightforward tensor manipulations (see Appendix C for tensor derivatives relations), the Eulerian $\mathbb{H}^{\,e}$ terms that compose the deviatoric part of the tangent modulus, which are given by

$$\begin{aligned}
\mathbb{H}_{1}^{\,e} &= \frac{1}{J}\Phi_*(\mathbb{H}_{1}^{\,L}) && (5.44)\\
&= \bar{\mathcal{W}}_{,11}\frac{1}{J}\left[(\bar{\mathbf{B}}-\frac{1}{3}\bar{I}_1\mathbf{I})\otimes(\bar{\mathbf{B}}-\frac{1}{3}\bar{I}_1\mathbf{I})\right]\\
&\quad +\bar{\mathcal{W}}_{,1}\frac{1}{J}\left[-\frac{1}{3}\left(\mathbf{I}\otimes(\bar{\mathbf{B}}-\frac{1}{3}\bar{I}_1\mathbf{I})+\bar{\mathbf{B}}\otimes\mathbf{I}-\bar{I}_1\mathbb{S}\right)\right]
\end{aligned}$$

$$\begin{aligned}
\mathbb{H}_{2}^{\,e} &= \frac{1}{J}\Phi_*(\mathbb{H}_{2}^{\,L}) && (5.45)\\
&= \bar{\mathcal{W}}_{,22}\frac{1}{J}\left[(\bar{I}_1\bar{\mathbf{B}}-\bar{\mathbf{B}}^2-\frac{2}{3}\bar{I}_2\mathbf{I})\otimes(\bar{I}_1\bar{\mathbf{B}}-\bar{\mathbf{B}}^2-\frac{2}{3}\bar{I}_2\mathbf{I})\right]\\
&\quad +\bar{\mathcal{W}}_{,2}\frac{1}{J}\left\{-\frac{2}{3}\mathbf{I}\otimes(\bar{I}_1\bar{\mathbf{B}}-\bar{\mathbf{B}}^2-\frac{2}{3}\bar{I}_2\mathbf{I})+\left[\bar{\mathbf{B}}\otimes\bar{\mathbf{B}}-\mathbb{S}^*-\frac{2}{3}\left(\bar{I}_1\bar{\mathbf{B}}-\bar{\mathbf{B}}^2\right)\otimes\mathbf{I}+\frac{2}{3}\bar{I}_2\mathbb{S}\right]\right\}
\end{aligned}$$

$$\begin{aligned}
\mathbb{H}_{4}^{\,(i)e} &= \frac{1}{J}\Phi_*(\mathbb{H}_{4}^{\,(i)L}) && (5.46)\\
&= \bar{\mathcal{W}}_{,44}^{(i)}\left\{\left[(\bar{\mathbf{a}}\otimes\bar{\mathbf{a}})-\frac{1}{3}\bar{I}_4{}^{(i)}\mathbf{I}\right]\otimes\left[(\bar{\mathbf{a}}\otimes\bar{\mathbf{a}})-\frac{1}{3}\bar{I}_4{}^{(i)}\mathbf{I}\right]\right\}\\
&\quad +\bar{\mathcal{W}}_{,14}^{(i)}\left\{\left[(\bar{\mathbf{a}}\otimes\bar{\mathbf{a}})-\frac{1}{3}\bar{I}_4{}^{(i)}\mathbf{I}\right]\otimes(\bar{\mathbf{B}}-\frac{1}{3}\bar{I}_1\mathbf{I})\right\}\\
&\quad +\bar{\mathcal{W}}_{,4}^{(i)}\left(-\frac{1}{3}\right)\left[\mathbf{I}\otimes\left[(\bar{\mathbf{a}}\otimes\bar{\mathbf{a}})-\frac{1}{3}\bar{I}_4{}^{(i)}\mathbf{I}\right]+(\bar{\mathbf{a}}\otimes\bar{\mathbf{a}})\otimes\mathbf{I}-\bar{I}_4{}^{(i)}\mathbb{S}\right].
\end{aligned}$$

[†] with respect to an orthonormal basis.

The volumetric part of the tangent modulus in Eulerian form, given by

$$\mathbb{C}^{\,e}_{\,vol} \quad = \quad \left[\frac{\partial\mathcal{U}}{\partial J} + J\frac{\partial^2\mathcal{U}}{\partial J^2}\right](\mathbf{I}\otimes\mathbf{I}) - 2\frac{\partial\mathcal{U}}{\partial J}\mathbb{S} \tag{5.47}$$

will depend on the choice of the penality function. Using the same function used in Abaqus, the energy density that represents the volumetric part is given by

$$\mathcal{U} = \frac{1}{D_1}\,(J-1)^2 \tag{5.48}$$

where D_1 determines the compressibility of the material. If $D = 0$, the material is taken as fully incompressible. The volumetric strain energy function $\mathcal{U}$ satisfies the condition $\mathcal{U} = 0$ for $J = 1$. Note that, for a quasi-incompressible response, the form of Eq. (5.48) is not a key point. The most important is to keep an adequate ratio between the bulk and the shear moduli of the material. If one wants to describe volume variation, several other function forms have been proposed for the volumetric term, see for example in Doll and Schweizerhof (2000), Bischoff *et al.* (2001) and references herein. Thereby, it is possible to rewrite the Eq. (5.47), using the quadratic function from Eq. (5.48), as

$$\mathbb{C}^{\,e}_{\,vol} \quad = \quad \left[\frac{2}{D_1}\,(2J-1)\right](\mathbf{I}\otimes\mathbf{I}) - \left(2J\frac{\partial\mathcal{U}}{\partial J}\right)\mathbb{S} \tag{5.49}$$

The convection term can be written using the Cauchy stress tensor $\boldsymbol{\sigma}$ and the fourth order symmetric tensor $\mathbb{S}$ as

$$(\boldsymbol{\sigma}\circ\mathbb{S} + \mathbb{S}\circ\boldsymbol{\sigma})_{ijkl} = \frac{1}{2}(\sigma_{ik}\delta_{jl} + \sigma_{il}\delta_{jk} + \sigma_{jl}\delta_{ik} + \sigma_{jk}\delta_{il}). \tag{5.50}$$

Finally, the tangent modulus that the UMAT must return to Abaqus is given by

$$\mathbb{C}^{\,Lr} \quad = \quad [\boldsymbol{\sigma}\circ\mathbb{S} + \mathbb{S}\circ\boldsymbol{\sigma}] + 4[\mathbb{H}^{\,e}_{\,1} + \mathbb{H}^{\,e}_{\,2} + \mathbb{H}^{\,e}_{\,4}] + \left[\frac{2}{D}\,(2J-1)\right](\mathbf{I}\otimes\mathbf{I}) \tag{5.51}$$

The stress and the tangent modulus are given by the first and second derivates of the strain energy function with respect to the first, second and fourth invariants. Thus, the above formulation is relevant for any energy form that depends on these invariants. Considering now the simplified model proposed in Section 5.5, the energy derivates with respect to the fourth invariant in Eq. (5.46) are given by

$$\bar{\mathcal{W}}_{,4}^{(i)} \quad = \quad 2k\,(w^{(i)}_{I_4})\,\mathcal{F}^{(i)}\,(\bar{I}^{(i)}_4 - 1) \tag{5.52}$$

$$\bar{\mathcal{W}}_{,44}^{(i)} \quad = \quad 2k\,(w^{(i)}_{I_4})\left\{\frac{\partial\mathcal{F}^{(i)}}{\partial\bar{I}^{(i)}_4}\,(\bar{I}^{(i)}_4 - 1) + \mathcal{F}^{(i)}\right\} \tag{5.53}$$

$$\bar{\mathcal{W}}_{,14}^{(i)} \quad = \quad \frac{\partial}{\partial\bar{I}_1}\left[2k\,(w^{(i)}_{I_4})\,\mathcal{F}^{(i)}\,(\bar{I}^{(i)}_4 - 1)\right] = 2k\,(w^{(i)}_{I_4})\,\frac{\partial\mathcal{F}^{(i)}}{\partial\bar{I}_1}(\bar{I}^{(i)}_4 - 1) \tag{5.54}$$

with the following conditions

$$\frac{\partial\mathcal{F}^{(i)}}{\partial\bar{I}_1} = 0 \quad \text{if} \quad \bar{I}_{1\max} = I_1 \tag{5.55a}$$

$$\frac{\partial\mathcal{F}^{(i)}}{\partial\bar{I}_1} = \eta\frac{1}{2}\left(\frac{\bar{I}_{1\max} - \bar{I}_1}{\bar{I}_{1\max} - 3}\right)^{-\frac{1}{2}}\left(\frac{1}{\bar{I}_{1\max} - 3}\right)\left(\frac{\bar{I}^{(i)}_{4\max} - \bar{I}^{(i)}_4}{\bar{I}^{(i)}_{4\max} - 1}\right)\left(\frac{\bar{I}^{(i)}_{4\max}}{\bar{I}_{4\max}}\right)^4 \quad \text{elseif} \tag{5.55b}$$

$$\frac{\partial \mathcal{F}^{(i)}}{\partial \bar{I}_4^{(i)}} = 0 \quad \text{if} \quad \bar{I}_{4\,\max}^{(i)} = \bar{I}_4^{(i)} \tag{5.56a}$$

$$\frac{\partial \mathcal{F}^{(i)}}{\partial \bar{I}_4^{(i)}} = \eta \sqrt{\frac{\bar{I}_{1\,\max} - \bar{I}_1}{\bar{I}_{1\,\max} - 3}} \left(\frac{1}{\bar{I}_{4\,\max}^{(i)} - 1} \right) \left(\frac{\bar{I}_{4\,\max}^{(i)}}{\bar{I}_{4\,\max}} \right)^4 \quad \text{elseif.} \tag{5.56b}$$

5.5.3 UMAT validation

The main idea is to validate numerical implementation of the simplified model into Abaqus FEA code. In this way, the TT experiments of Chapter 3 were simulated. A wide plate was designed and the subsamples are previously orientated on the plate, forming a set of four different directions, as shown in Fig. 5.4(a). The element choice was the three-dimensional 8–node linear element (C3D8H) with hybrid constant pressure interpolation. The constant pressure and continuous displacement interpolation is fundamental in order to alleviate volumetric locking.

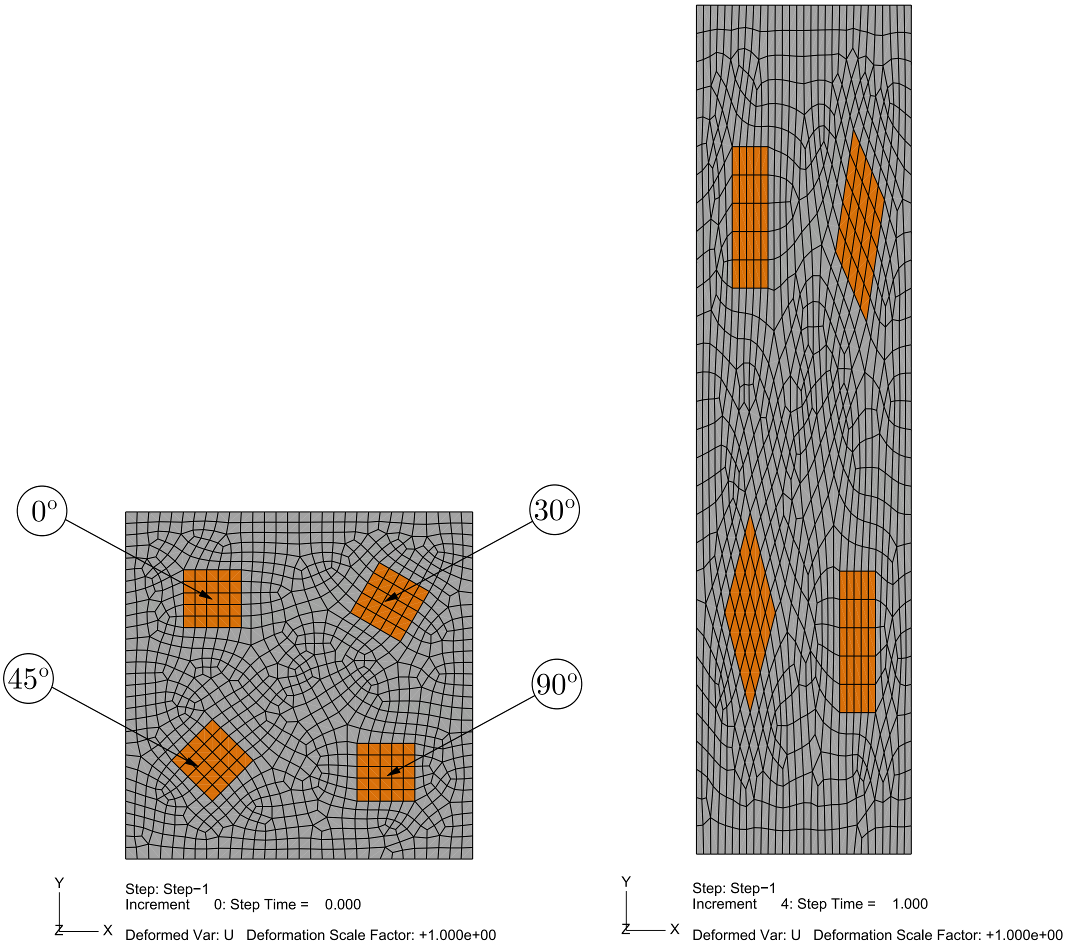

(a) (b)

Figure 5.4: Three-dimensional finite element model from a RTV3428 plate. (a) Undeformed configuration. (b) Deformed configuration (first load).

An uniaxial tensile loading cycle (load–unload) was performed on the plate and Fig. 5.4(b) shows the deformed configuration at the end of the load step. After unloading of the plate, the command line *MODEL CHANGE is used to remove undesirable elements during an analysis, therefore, the effect of the removed region on the rest of the model is completely absent and no further element calculations are performed for elements that being removed. See Abaqus Manual (2010) for details. This feature permits to simulate the experimental subsamples, cut in different directions on the pre-stretched plate, as shown in Fig. 5.5(a). Finally, a second uniaxial tensile loading cycle is performed on each subsample, respecting their orientations. Fig. 5.5(b) shows the end of the load step on each subsample.

The FEA results were first confronted with the analytical solutions, and a perfect agreement was observed, as shown in Fig. 5.6. This permits to validate the implementation of the model in Abaqus. Finally, Fig. 5.7 presents the FEA results, the original model from Chapter 4 and the uniaxial pre-conditioning experimental data.

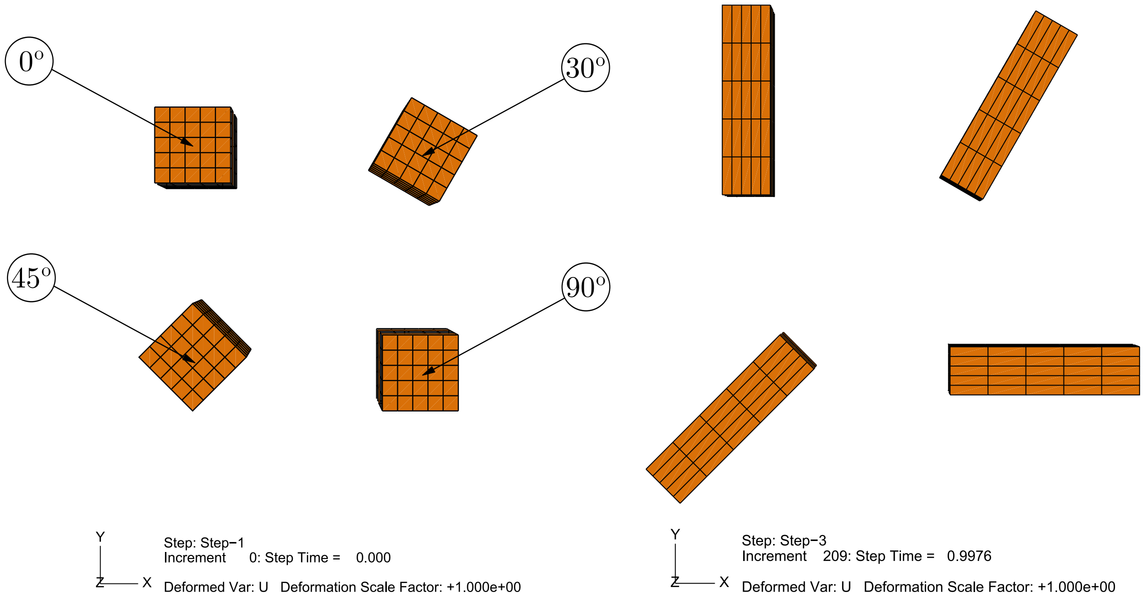

(a) (b)

Figure 5.5: The directional subsamples cut details. (a) After pre-stretching. (b) Deformed configuration (second loading).

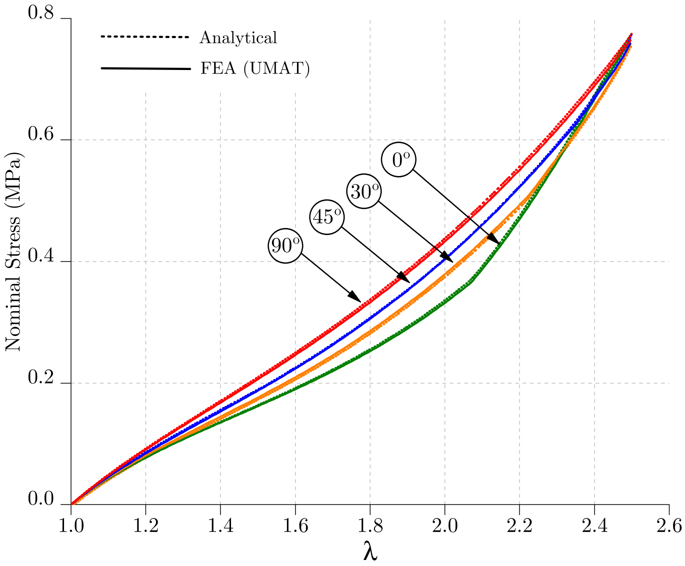

Figure 5.6: FEA results validation by comparing FEA simulations and analytical results.

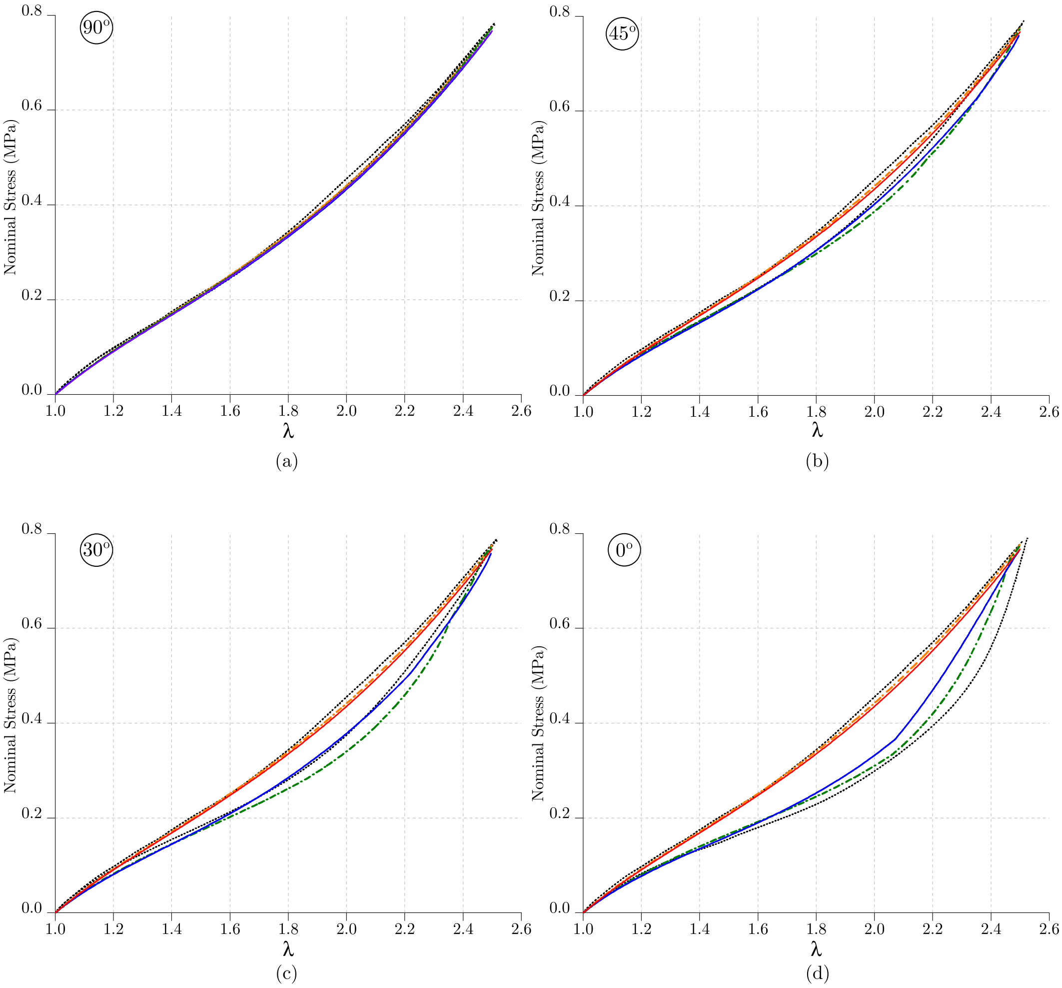

(a) (b)

(c) (d)

Figure 5.7: FEA results (solid lines) using the simplified model version, the original analytical model from Chapter 4 (dash-dotted lines) and the uniaxial pre-conditioning experimental data (dotted lines).

5.6 Conclusion

The constitutive modeling of the stress softening of a particle filled elastomer is a complicated problem. In this Chapter a simplified version of the proposed constitutive model for induced anisotropy by Mullins effect was proposed. The simplified model captured all the experimental data trends.

The simplified model, with a modified evolution function, was implemented into Abaqus Standard via an user-defined material subroutine, UMAT. Finite element analysis was performed to simulate the anisotropic response of a filled silicone-rubber regarding stress softening in four different directions. The FEA results exhibit relatively good agreement with the experimental data. In future work, the softening evolution function expressed in terms of energies ($\mathcal{M}$) may be also implemented in an UMAT.

Comparison between the FEA results and experimental data as well the validation using analytical forms showed that the constitutive model and its finite element implementation in a commercial finite element code provide an useful and dependable numerical tool for modelling three-dimensional structures, more precisely, in the context of this work, the RAAMO ell-robot skin.

General Conclusion and Outlook

An essential aspect of the present work is the construction of an unprecedented experimental data dealing with the study of the induced anisotropy by Mullins effect. A considerable effort was made to develop a protocol to manufacture silicone samples under controlled conditions. This step was fundamental to propose an experimental methodology for mechanical tests. Reproducibility and accuracy of measurements were evaluated through successive mechanical tests frequently performed on rubbers. Results showed that our protocol to manufacture the silicone specimens and our experimental methodology work well and provide a precise experimental characterization of silicone rubber.

Using the proposed methodology, experimental results that illustrate stress softening in particle-reinforced silicone rubber were obtained. These results allowed to analyze the stress softening for three different loading cases: uniaxial, planar and equibiaxial tensile tests. In this last loading case, the conventional application of the bulge test was used to determine the equibiaxiality of the stress and strain obtained at the top of the sample. A representative selection of the existent isotropic models of Mullins effect was investigated. Under the light of the three different loading cases results, the limitations of these models were evaluated. Nevertheless, the analysis of these experimental data proved that proportionality between second loading curves is not a good way to model the strain-stress curves. Thus, two main ways to well describe the Mullins effect could be noticed. The first one, by using a non-constant multiplicative function on second loading curves, the second one by using different non-proportional functions. These two ways, correspond to double-network and physical approaches, respectively. However, the above results are not sufficient to characterize the anisotropic nature of Mullins effect.

Considering the large strain level in rubbery mechanical analysis, a special attention in this study was given to the use of non-contact full field strain measures, notably the three-dimensional digital image correlation method. In this thesis, a method which enriches greatly the analysis of usual bulge tests by using the 3D-DIC technique was proposed. The determination of the curvature tensor fields from 3D-DIC data allowed to determine the planar stress-strain fields associated with the membrane inflation problem without any constitutive equation assumption. Finally, the bulge test can be used as one very rich heterogeneous mechanical test which allows obtaining valuable information for testing different types of materials for a wide range of stress-strain states ranging from equibiaxial to planar tensile stress state. This feature was exploited to produce an original preconditioning method to study the anisotropy induced by the Mullins effect.

The use of the bulge test, as a biaxial preconditioning test, was originally proposed to find an evidence for an even more complex memory behavior of the material. The measurements made along the meridian of the inflated membrane provide unprecedented information about the history of principal stress and principal strain directions and results clearly showed that the induced anisotropy is dependent on the pre-stretch biaxiality ratio. The analysis of these data permits to highlight that the maximum elongational energy in the maximum principal direction is the governing parameter that defines the return–point on the virgin tensile loading curve.

Based on the experimental observations, a new network model for finite elasticity of rubber-like materials was proposed. This model can be seen as a cornerstone for all the subsequent developments concerning the induced anisotropy by Mullins effect applied to the finite inelasticity of rubbery. The form of modeling is built by superposing a classical isotropic hyperelastic model and a stress-softening part based on the double network theory. The core of the proposed model is a new measure for the amount of stress-softening. An energetically motivated tensor measure was introduced to represent the repartition of the elongational energy in space. With this new measure, it becomes possible to establish a relation between the strain energy in each direction in the polymer network and the maximum global energy, defining the three-dimensional overall response of the material. The overall model contains one effective material parameter to describe the evolution of the Mullins effect, which was fitted on the second tensile loading curves for all the tests. Finally, the developed model was tested against experimental data for homogeneous and inhomogeneous deformations. In the last case, the model was confronted with the results obtained from very different strain histories, owing to the different preconditioning methods experimentally employed. This new approach captures the principal characteristics of the Mullins effect underlined in literature using a simple constitutive form, that only depends on one parameter.

In the final part of the thesis, a simplified constitutive model for a fast implementation into a commercial finite element code was developed. The formulation makes use of the intrinsic features of the original model. The obtained results indicate the predictive performance of the proposed model and its high suitability for the finite element analysis of boundary-value problems. Comparison between the finite element analysis results and experimental data as well as the validation using analytical forms showed that the constitutive model and its finite element implementation in a commercial finite element code provide an useful and dependable numerical tool.

The proposed constitutive equation can now be used to calculate real engineering structural parts. Future comparisons between finite element simulations and 3D-DIC data from experimental tests will permit to validate the model for even more complex deformation paths. In this case, special attention needs to be given on the convergence analysis. Nevertheless, the model can be improved by working on the choice of functions used in the constitutive equations for improving the agreement with experimental data. Due to the simplicity of the model, future studies should also include viscoelastic, hysteresis and thermal effects.

Bibliography

Abaqus Manual (2010). *Abaqus Theory Manual V6.10.* Dassault Systèmes Simulia Corp., Providence, RI, USA.

Adkins, J. E. and Rivlin, R. S. (1952). Large elastic deformation of isotropic materials. IX. The deformation ofthin shells. *Phil. Trans. R. Soc.*, **A**244, 505–532.

Arruda, E. M. and Boyce, M. C. (1993). A three dimensional constitutive model for the large stretch behavior of rubber elastic materials. *J. Mech. Phys. Solids*, **4**1(2), 389–412.

Avril, S., Bonnet, M., Bretelle, A., Grediac, M., Hild, F., Ienny, P., Latourte, F., Lemosse, D., Pagano, S., Pagnacco, E., *et al.* (2008). Overview of identification methods of mechanical parameters based on full-field measurements. *Exp. Mech.*, **4**8(4), 381–402.

Basar, Y. and Weichert, D. (2000). *Nonlinear continuum mechanics of solids.* Springer Verlag, Berlin.

Bazant, Z. P. and Oh, B. H. (1986). Efficient numerical integration on the surface of a sphere. *Z. Anegw. Math. Mech.*, **6**6, 37–49.

Beatty, M. F. and Krishnaswamy, S. (2000). A theory of stress-softening in incompressible isotropic materials. *J. Mech. Phys. Solids*, **4**8, 1931–1965.

Becker, T., Splitthof, K., Siebert, T., and Kletting, P. (2006). Error estimations of 3d digital image correlation measurements. volume 6341, page 63410F. SPIE.

Bergstrom, J. S. and Boyce, M. C. (2000). Large strain time-dependant behavior of filled elastomers. *Mech. Mater.*, **3**2, 627–644.

Besdo, D., Ihlemann, J., Kingston, J., and Muhr, A. (2003). Modelling inelastic stress-strain phenomena and a scheme for efficient experimental characterization. *In: Busfield, Muhr (eds) Constitutive models for Rubber III. Swets & Zeitlinger, Lisse.*, pages 309–317.

Bischoff, J. E., Arruda, E. M., and Grosh, K. (2001). A new constitutive equation for the compressibility of elastomers at finitedeformations. *Rubber Chem. Technol.*, **7**4, 541–559.

Bonet, J. and Wood, R. D. (1997). *Nonlinear continuum mechanics for finite element analysis.* Cambridge University Press.

Boyce, M. C. and Arruda, E. M. (2000). Constitutive models of rubber elasticity: A review. *Rubber Chem. Technol.*, **7**3, 504–523.

Boyer, F., Porez, M., and Khalil, W. (2006a). Macro-continuous computed torque algorithm for a three-dimensional eel-like robot. *Robotics, IEEE Transactions on*, **2**2(4), 763 –775.

Boyer, F., Alamir, M., Chablat, D., Khalil, W., Leroyer, A., and Lemoine, P. (2006b). Robot anguille sous-marin en 3D. *Techniques de l'Ingénieur*, **S** 7 856, 1–16.

Boyer, F., Porez, M., Leroyer, A., and Visonneau, M. (2008). Fast dynamics of an eel-like robot - Comparisons with Navier-Stokes simulations. *Robotics, IEEE Transactions on*, **2**4(6), 1274 –1288.

Boyer, F., Porez, M., and Leroyer, A. (2010). Poincaré-Cosserat Equations for the Lighthill Three-dimensional Large Amplitude Elongated Body Theory: Application to Robotics. *Journal of Nonlinear Science*, **2**0, 47–79. 10.1007/s00332-009-9050-5.

Briand, D. (2004). Etude de la peau dún robot anguille. Master's thesis, Ecole Centrale de Nantes - Institut de Recherche en Communications et en Cybernétique de Nantes - IRCcYN.

Brown, W. F. and Thompson, F. (1949). Strength and failure characteristics of metal membranes in circular bulging. *Trans. Am. Soc. of Mech. Engrs.*, **7**1, 575–585.

Carmo, M. P. (1976). *Differential geometry of curves and surfaces.* Prentice-Hall lnc., Englewood Cliffs, New Jersey.

Chablat, D. (2008). Kinematic analysis of the vertebra of an eel like robot. In *ASME 2008 International Design Engineering Technical Conferences & Computers and Information in Engineering Conference IDETC/CIE.*

Chagnon, G., Verron, E., Gornet, L., Marckmann, G., and Charrier, P. (2004). On the relevance of Continuum Damage Mechanics as applied to the Mullins effect in elastomers. *J. Mech. Phys. Solids*, **5**2, 1627–1650.

Chagnon, G., Verron, E., Marckmann, G., and Gornet, L. (2006). Development of new constitutive equations for Mullins effect in rubber using the network alteration theory. *Int. J. Solids Struct.*, **4**3, 6817–6831.

Ciarlet, P. (2005). *An Introduction to Differential Geometry with Applications to Elasticity.* Springer.

Dargazany, R. and Itskov, M. (2009). A network evolution model for the anisotropic Mullins effect in carbon black filled rubbers. *International Journal of Solids and Structures*, **4**6(16), 2967 – 2977.

De Souza Neto, E., Perić, D., and Owen, D. (1994). A phenomenological three dimensional rate independent continuum damage model for highly filled polymers: formulation and computational aspects. *J. Mech. Phys. Solids.*, **4**2(10), 1533–1550.

De Souza Neto, E., Perić, D., and Owen, D. (2008). *Computational Methods for Plasticity: Theory and Applications.* John Wiley & Sons, United Kingdom.

Diani, J., Brieu, M., Vacherand, J. M., and Rezgui, A. (2004). Directional model isotropic and anisotropic hyperelastic rubber-like materials. *Mech. Mater.*, **3**6, 313–321.

Diani, J., Brieu, M., and Vacherand, J. M. (2006a). A damage directional constitutive model for the Mullins effect with permanent set and induced anisotropy. *Eur. J. Mech. A/Solids*, **2**5, 483–496.

Diani, J., Brieu, M., and Gilormini, P. (2006b). Observation and modeling of the anisotropic visco-hyperelastic behavior of a rubberlike material. *Int. J. Solids Struct.*, **4**3, 3044–3056.

Diani, J., Fayolle, B., and Gilormini, P. (2009). A review on the Mullins effect. *Eur. Polym. Journal*, **4**5, 601–612.

Doll, S. and Schweizerhof, K. (2000). On the development of volumetric strain energy functions. *J. Appl. Mech.*, **6**7, 17–21.

Dorfmann, A. and Ogden, R. W. (2003). A pseudo-elastic model for loading, partial unloading and reloading of particle-reinforced rubbers. *Int. J. Solids Struct.*, **4**0, 2699–2714.

Dorfmann, A. and Ogden, R. W. (2004). A constitutive model for the Mullins effect with permanent set in particule-reinforced rubber. *Int. J. Solids Struct.*, **4**1, 1855–1878.

Dudderar, T., Koch, F., and Doerries, E. (1977). Measurement of the shapes of foil bulge-test samples. *Exp. Mech.*, **1**7, 133–140. 10.1007/BF02324211.

Ehret, A. E. and Itskov, M. (2009). Modeling of anisotropic softening phenomena: Aplication to soft biological tissues. *Int. J. Plast.*, **2**5, 901–919.

Ehret, A. E., Itskov, M., and Schmid, H. (2010). Numerical integration on the sphere and its effect on the material symmetry of constitutive equations - A comparative study. *International Journal for Numerical Methods in Engineering*, **8**1(2), 189–206.

Feng, W. (1992). Viscoelastic behavior of elastomeric membranes. *J. Appl. Mech.*, **59**, 29–34.

Garcia, D. (2010). Robust smoothing of gridded data in one and higher dimensions with missing values. *Comput. Statist. Data Anal.*, **5**4(4), 1167 – 1178.

Göktepe, S. and Miehe, C. (2005). A micro-macro approach to rubber-like materials. Part III: The micro-sphere model of anisotropic Mullins-type damage. *J. Mech. Phys. Solids*, **5**3, 2259–2283.

Govindjee, S. and Simo, J. C. (1991). A micro-mechanically continuum damage model for carbon black filled rubbers in corporating Mullins's effect. *J. Mech. Phys. Solids*, **3**9(1), 87–112.

Govindjee, S. and Simo, J. C. (1992). Mullins' effect and the strain amplitude dependence of the storage modulus. *Int. J. Solids. Structures*, **2**9(14-15), 1737–1751.

Green, A. and Adkins, J. (1970). *Large Elastic Deformation.* Clarendon Press - Oxford, 2nd edition.

Green, M. S. and Tobolsky, A. V. (1946). A new approach for the theory of relaxing polymeric media. *J. Chem. Phys.*, **1**4, 87–112.

Grolleau, V., Gary, G., and Mohr, D. (2008). Biaxial testing of sheet materials at high strain rates using viscoelastic bars. *Exp. Mech.*, **4**8, 293–306. 10.1007/s11340-007-9073-5.

Grolleau, V., Louche, H., Delobelle, V., Penin, A., Rio, G., Liu, Y., and Favier, D. (2011). Assessment of tension-compression asymmetry of niti using circular bulge testing of thin plates. *Scripta Materialia*, **I**n Press, Corrected Proof, –.

Guélon, T., Toussaint, E., Cam, J.-B. L., Promma, N., and Grédiac, M. (2009). A new characterisation method for rubber. *Polym. Test.*, **2**8(7), 715 – 723.

Gurtin, M. E. and Francis, E. C. (1981). Simple rate-independent model for damage. *J. Spacecraft*, **1**8(3), 285–286.

Hanson, D. E., Hawley, M., Houlton, R., Chitanvis, K., Rae, P., Orler, E. B., and Wrobleski, D. A. (2005). Stress softening experiments in silica-filled polydimethylsiloxane provide insight into a mechanism for the Mullins effect. *Polymer*, **4**6(24), 10989 – 10995.

Hill, R. (1950). A theory of the plastic bulging of a metal diaphragm by lateral pressure. *Phil. Mag.*, **4**1, 1133–1142.

Holzapfel, G. A. (2000). *Nonlinear solid mechanics - A continuum approach for engineering.* John Wiley and Sons, LTD.

Horgan, C. O., Ogden, R. W., and Saccomandi, G. (2004). A theory of stress softening of elastomers based on finite chain extensibility. *Proc. R. Soc. London A*, **4**60, 1737–1754.

Hsu, F., Liu, A., Downs, J., Rigamonti, D., and Humphrey, J. (1995). A triplane video-based experimental system for studying axisymmetrically inflated biomembranes. *IEEE T. Bio-Med. Eng.*, **4**2, 442–450.

Humphrey, J. D. (1998). Computer methods in membrane biomechanics. *Comput. Methods Biomech. Biomed. Eng.*, **1**, 171– 210.

Itskov, M., Haberstroh, E., Ehret, A. E., and Vohringer, M. C. (2006). Experimental observation of the deformation induced anisotropy of the Mullins effect in rubber. *KGK-Kautschuk Gummi Kunststoffe*, **5**9(3), 93–96.

Itskov, M., Ehret, A., Kazakeviciute-Makovska, R., and Weinhold, G. (2010). A thermodynamically consistent phenomenological model of the anisotropic Mullins effect. *ZAMM - Journal of Applied Mathematics and Mechanics / Zeitschrift für Angewandte Mathematik und Mechanik*, **90**(5), 370–386.

Johnson, M. A. and Beatty, M. F. (1993). The Mullins effect in uniaxial extension and its influence on transverse vibration of rubber string. *Continuum Mech. Thermodyn.*, **5**, 83–115.

Kazakeviciute-Makovska, R. (2007). Experimentally determined properties of softening functions in pseudo-elastic models of the Mullins effect. *Int. J. Solids Struct.*, **4**4, 4145–4157.

Klingbeil, W. and Shield, R. (1964). Some numerical investigations on empirical strain energy functions in the large axisymmetric extensions of rubber membranes. *Z. Angew. Math. Phys.*, **1**5, 608–629.

Kriewall, T., Akkas, N., Bylski, D., Melvin, J., and Work, B. (1983). Mechanical-behavior of fetal dura mater under large axisymmetric inflation. *J. Biomech. Eng. - T. ASME*, **1**05(23), 71–76.

Krishnaswamy, S. and Beatty, M. F. (2000). The Mullins effet in compressible solids. *Int. J. Eng. Sci.*, **3**8, 1397–1414.

Kyriacou, S. K., Shah, A. D., and Humphrey, J. D. (1997). Inverse finite element characterization of nonlinear hyperelastic membranes. *J. Appl. Mech.*, **6**5, 257–262.

Laiarinandrasana, L., Piques, R., and Robisson, A. (2003). Visco-hyperelastic model with internal state variable coupled with discontinuous damage concept under total lagrangian formulation. *Int. J. Plast.*, **1**9, 977–1000.

Laraba-Abbes, F., Ienny, P., and Piques, R. (2003). A new tailor-made methodology for the mechanical behaviour analysis of rubber-like materials: II. Application to the hyperelastic behaviour characterization of a carbon-black filled natural rubber vulcanizate. *Polymer*, **4**4(3), 821 – 840.

Lemaitre, J. and Chaboche, J. L. (1990). *Mechanics of solid materials.* Cambridge University Press.

Lion, A. (1996). A constitutive model for carbon black filled rubber: Experimental investigations and mathematical representation. *Continuum Mech. Thermodyn.*, **8**, 153–169.

Luo, P., Chao, Y., Sutton, M., and Peters, W. (1993). Accurate measurement of three-dimensional deformations in deformable and rigid bodies using computer vision. *Exp. Mech.*, **3**3, 123–132.

Machado, G., Chagnon, G., and Favier, D. (2010). Analysis of the isotropic models of the Mullins effect based on filled silicone rubber experimental results. *Mech. Mater.*, **42**(9), 841 – 851.

Machado, G., Chagnon, G., and Favier, D. (2011a). Induced anisotropy by the Mullins effect in filled silicone rubber. *Submited to Mech. Mater.*

Machado, G., Favier, D., and Chagnon, G. (2011b). Membrane curvatures and stress-strain full fields of bulge tests from 3D-DIC measurements. Theory, validation and experimental results on a silicone elastomer. *Submitted to Exp. Mech.*

Marckmann, G. and Verron, E. (2006). Comparison of hyperelastic models for rubberlike materials. *Rubber Chem. Technol.*, **7**9(5), 835–858.

Marckmann, G., Verron, E., Gornet, L., Chagnon, G., and Fort, P. C. P. (2002). A theory of network alteration for the Mullins effect. *J. Mech. Phys. Solids.*, **5**0, 2011–2028.

Martin Borret, G. (1998). *Sur la propagation de fissures dans les élastomères.* Ph.D. thesis, Ecole Polytechnique.

Mellott, S. A. (2009). Design of an actuation mechanism for compliant-body biomimetic robots. Master's thesis, Massachusetts Institute of Technology. Dept. of Mechanical Engineering.

Meunier, L., Chagnon, G., Favier, D., Orgéas, L., and Vacher, P. (2008). Mechanical experimental characterisation and numerical modelling of an unfilled silicone rubber. *Polym. Test.*, **2**7, 765–777.

Miehe, C. (1995). Discontinuous and continuous damage evolution in Ogden type large strain elastic materials. *Eur. J. Mech., A/Solids*, **1**4(5), 697–720.

Miehe, C. and Göktepe, S. (2005). A micro-macro approach to rubber-like materials. Part III: The micro-sphere model anisotropic Mullins-type damage. *J. Mech. Phys. Solids*, **5**3, 2259–2283.

Miehe, C. and Keck, J. (2000). Superimposed finite elastic-viscoelastic-plastoelastic stress response with damage in filled rubbery polymers. Experiments, modelling and algorithmic implementation. *J. Mech. Phys. Solids*, **4**8, 323–365.

Miller, C. E. (1979). Determination of elastic parameters for human fetal membranes. *J. Rheol.*, **2**3, 57–78.

Mitchell, J. S., Zorman, C. A., Kicher, T., Roy, S., and Mehregany, M. (2003). Examination of bulge test for determining residual stress, Young's modulus, and Poisson's ratio of 3C-SiC thin films. *J. Aerospace Eng.*, **1**6(2), 46–54.

Mooney, M. (1940). A theory of large elastic deformation. *J. Appl. Phys.*, **1**1, 582–592.

Muhr, A. H., Gough, J., and Gregory, I. H. (1999). Experimental determination of model for liquid silicone rubber: Hyperelasticity and Mullins effect. In *Proceedings of the First European Conference on Constitutive Models forRubber*, pages 181–187. Dorfmann A. Muhr A.

Mullins, L. (1947). Effect of stretching on the properties of rubber. *J. Rubber Res.*, **1**6, 275–289.

Mullins, L. (1969). Softening of rubber by deformation. *Rubber Chem. Technol.*, **42**, 339–362.

Ogden, R. W. and Roxburgh, D. G. (1999). A pseudo-elastic model for the Mullins effect in filled rubber. *Proc. R. Soc. Lond. A*, **4**55, 2861–2877.

Orteu, J. J. (2009). 3-D computer vision in experimental mechanics. *Opt. Laser Eng.*, **47**(3-4), 282–291.

Orteu, J.-J., Bugarin, F., Harvent, J., Robert, L., and Velay, V. (2010). Multiple-camera instrumentation of a single point incremental forming process pilot for shape and 3D displacement measurements: Methodology and results. *Exp. Mech.*, pages 1–15. 10.1007/s11340-010-9436-1.

Papkov, V. S., Godovskii, Y. K., Bulkin, A. F., Zhdanov, A. A., Slonimskii, G. L., and Andrianov, K. A. (1975). Energy investigation of the softening of siloxane rubbers during deformation. *Mechanics of Composite Materials*, **11**(3), 329–333.

Park, B. H. and Hamed, G. R. (2000). Anisotropy in gum and black filled sbr and nr vulcanizates due to large deformation. *Korea Polymer Journal*, **8**, 268–275.

Pawelski, H. (2001). Softening behaviour of elastomeric media after loading in changing directions. *Constitutive models for rubber, Besdo, Schuster & Ihleman (eds)*, pages 27–34.

Qi, H. J. and Boyce, M. C. (2004). Constitutive model for stretch-induced softening of the stress-stretch behaviorof elastomeric materials. *J. Mech. Phys. Solids*, **52**, 2187–2205.

Ross, E. and Prager, W. (1954). On the theory of the bulge test. *Q Appl. Math.*, **12**, 86–91.

Sands, C. (2009). Rapid implementation of material models within finite element analysis. *Computational Materials Science*, **47**(1), 286 – 296.

Sasso, M., Palmieri, G., Chiappini, G., and Amodio, D. (2008). Characterization of hyperelastic rubber-like materials by biaxial and uniaxial stretching tests based on optical methods. *Polym. Test.*, **27**, 995–1004.

Schreier, H. and Sutton, M. (2002). Systematic errors in digital image correlation due to undermatched subset shape functions. *Exp. Mech.*, **42**, 303–310. 10.1007/BF02410987.

Selby, J. C. and Shannon, M. A. (2007). Apparatus for measuring the finite load-deformation behavior of a sheet of epithelial cells cultured on a mesoscopic freestanding elastomer membrane. *Rev. Sci. Instrum.*, **7**8(9), 094301.

Septanika, E. G. and Ernst, L. J. (1998). Application of the network alteration theory for modeling the time dependent constitutive behavior of rubber. Part I - General theory. *Mech. Mater.*, **3**0, 253–263.

Seshaiyer, P., Hsu, F. P. K., Shah, A. D., Kyriacou, S. K., and Humphrey, J. D. (2001). Multiaxial mechanical behavior of human saccular aneurysms. *Comput. Methods Biomech. Biomed. Eng.*, **4**(3), 281–289.

Sfakiotakis, M., Lane, D., and et J.B.C. Davies (1999). Review of fish swimming modes for aquatic locomotion. *IEEE Journal of oceanic engineering*, **2**4, 237–252.

Shariff, M. H. B. M. (2006). An anisotropic model of the Mullins effect. *J. Eng. Math.*, **56**(4), 415–435.

Simo, J. C. (1987). On a fully three-dimensional finite-strain viscoelastic damage model: formulation and computational aspects. *Comp. Meth. Appl. Mech. Engng*, **6**0, 153–173.

Sutton, M. A. (2008). Digital image correlation for shape and deformation measurements. *Springer Handbook of Experimental Solid Mechanics - PartC*, pages 565–600.

Sutton, M. A., Orteu, J.-J., and Schreier, H. W. (2009). *Image Correlation for Shape, Motion and Deformation Measurements: Basic Concepts,Theory and Applications.* Springer.

Toponogov, V. A. (2006). *Differential Geometry of Curves and Surfaces: A Concise Guide*. Boston, MA.

Treloar, L. R. G. (1943). The elasticity of a network of long chain molecules (I and II). *Trans. Faraday Soc.*, **3**9, 36–64 ; 241–246.

Treloar, L. R. G. (1944). Strains in an inflated rubber sheet and the mechanism of bursting. *Trans. of the Institution of Rubber Industry*, **1**9, 201–212.

Triantafyllou, M., Yue, D., and Techet, A. (2010). Pike-robot. MIT Towing Tank website. `http://web.mit.edu/towtank`.

Triantafyllou, M. S. and Triantafyllou, G. S. (1995). An efficient swimming machine. *Scientific American*, **2**72, 40–48.

Tsakalakos, T. (1981). The bulge test - A comparison of theory and experiment for isotropic and anisotropic films. *Thin Solid Films*, **7**5, 293–305.

Wineman, A. S. (1976). Large axisymmetric inflation of a nonlinear viscoelastic membrane by lateral pressure. *Trans. Soc. Rheo.*, **2**0(23), 203 1976.

Wineman, A. S. (1978). On axisymmetric deformations of nonlinear viscoelastic membranes. *J. Non-Newtonian Fluid Mech.*, **4**(23), 249–260.

Yang, W. and Feng, W. (1970). On axisymmetrical deformations of nonlinear membranes. *J. Appl. Mech.*, **37**, 1002–1011.

Zuñiga, A. E. (2005). A phenomenological energy-based model to characterize stress-softening effectin elastomers. *Polymer*, **4**6, 3496–3506.

Zuñiga, A. E. and Beatty, M. F. (2002). A new phenomenological model for stress-softening in elastomers. *Z. Angew. Math. Phys.*, **5**3, 794–814.

Appendices

APPENDIX

A

Surface curvatures code

The MatLab routine used to evaluate the surface curvatures.

```
function [K,H,Ki,Kii] = scurvature(X,Y,Z,gs)
% scurvature - compute gaussian, mean and
%              principal curvatures of a surface
%
% [K,H,Ki,Kii] = scurvature(X,Y,Z,gs), where:
%   - X,Y,Z are matrix of points on the surface.
%   - gs spacing between points in every direction. (Default gs=1)
%   - K the gaussian curvature.
%   - H the mean curvatures.
%   - Ki and Kii are minimum and maximum curvatures at each point.

% First Derivatives
[Xu,Xv]=gradient(X,gs);
[Yu,Yv]=gradient(Y,gs);
[Zu,Zv]=gradient(Z,gs);

% Second Derivatives
[Xuu,Xuv]=gradient(Xu,gs);
[Yuu,Yuv]=gradient(Yu,gs);
[Zuu,Zuv]=gradient(Zu,gs);

[Xuv,Xvv]=gradient(Xv,gs);
[Yuv,Yvv]=gradient(Yv,gs);
[Zuv,Zvv]=gradient(Zv,gs);

% Reshape 2D Arrays into vectors
Xu=Xu(:);   Yu=Yu(:);   Zu=Zu(:);
Xv=Xv(:);   Yv=Yv(:);   Zv=Zv(:);
Xuu=Xuu(:); Yuu=Yuu(:); Zuu=Zuu(:);
Xuv=Xuv(:); Yuv=Yuv(:); Zuv=Zuv(:);
Xvv=Xvv(:); Yvv=Yvv(:); Zvv=Zvv(:);

```

```
Xu=[Xu Yu Zu];
Xv=[Xv Yv Zv];
Xuu=[Xuu Yuu Zuu];
Xuv=[Xuv Yuv Zuv];
Xvv=[Xvv Yvv Zvv];

% First fundamental form coeffecients (g11,g12,g22)
g11=dot(Xu,Xu,2);
g12=dot(Xu,Xv,2);
g22=dot(Xv,Xv,2);

% Normal vector (g3)
m=cross(Xu,Xv,2);
p=sqrt(dot(m,m,2));
g3=m./[p p p];

% Second fundamental Coeffecients of the surface (b11,b12,b22)
b11=dot(Xuu,g3,2);
b12=dot(Xuv,g3,2);
b22=dot(Xvv,g3,2);

[s,t] = size(Z);

% Gaussian Curvature (K)
K=(b11.*b22 - b12.^2)./(g11.*g22 - g12.^2);
K=reshape(K,s,t);

% Mean Curvature (H)
H=(g11.*b22 + g22.*b11 - 2.*g12.*b12)./(2*(g11.*g22 - g12.^2));
H=reshape(H,s,t);

%% Principal Curvatures.
Ki=H+sqrt(H.^2 - K);
Kii=H-sqrt(H.^2 - K);

%end scurvature
```

APPENDIX

B

The material directions construction

The proposed model uses $n = 2 \times 21$ integration points with cartesian coordinates defined in Table B.1. Only the 21^{st} direction are summarized, the 21 others are their opposite. The directions are represented on the unit sphere by the end point of each vector, the origin being the point O for each vector. Some points are represented for a eighth of space in Fig. B.1. The other directions are obtained by a symmetry with respect to the plan (O, X_1, X_2); (O, X_2, X_3) et (O, X_1, X_3).

Table B.1: Direction cosines and weights for 2×21 points (orthonormal symmetries) of each vector $\mathbf{a}_0^{(i)}$.

i direction	X_1	X_2	X_3	w
1	0	0	1	0.0265214244093
2	0	1	0	0.0265214244093
3	1	0	0	0.0265214244093
4	0	0.707106781187	0.707106781187	0.0199301476312
5	0	-0.707106781187	0.707106781187	0.0199301476312
6	0.707106781187	0	0.707106781187	0.0199301476312
7	-0.707106781187	0	0.707106781187	0.0199301476312
8	0.707106781187	0.707106781187	0	0.0199301476312
9	-0.707106781187	0.707106781187	0	0.0199301476312
10	0.836095596749	0.387907304067	0.387907304067	0.0250712367487
11	-0.836095596749	0.387907304067	0.387907304067	0.0250712367487
12	0.836095596749	-0.387907304067	0.387907304067	0.0250712367487
13	-0.836095596749	-0.387907304067	0.387907304067	0.0250712367487
14	0.387907304067	0.836095596749	0.387907304067	0.0250712367487
15	-0.387907304067	0.836095596749	0.387907304067	0.0250712367487
16	0.387907304067	-0.836095596749	0.387907304067	0.0250712367487
17	-0.387907304067	-0.836095596749	0.387907304067	0.0250712367487
18	0.387907304067	0.387907304067	0.836095596749	0.0250712367487
19	-0.387907304067	0.387907304067	0.836095596749	0.0250712367487
20	0.387907304067	-0.387907304067	0.836095596749	0.0250712367487
21	-0.387907304067	-0.387907304067	0.836095596749	0.0250712367487

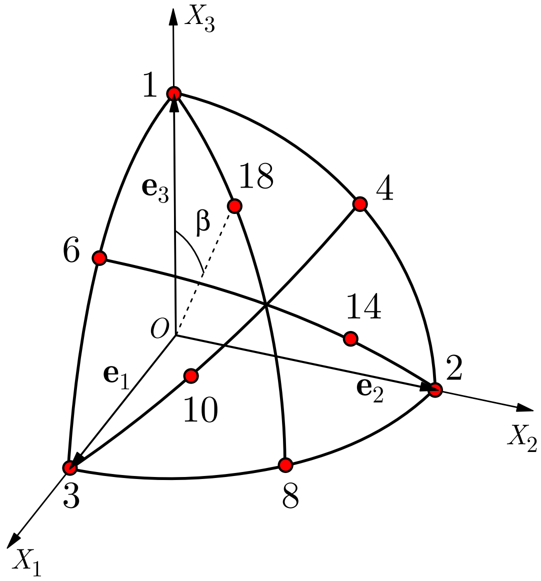

Figure B.1: The material directions construction. The set of direction $\mathbf{a}_0^{(i)}$ is defined by the polyhedron vertices.

APPENDIX

C Tensor derivatives relations

C.1 Derivative of a tensor with respect to itself

Let **A** be a second order tensor. Then

$$\frac{\partial \mathbf{A}}{\partial \mathbf{A}} : \mathbf{T} = \left[\frac{\partial}{\partial \alpha}(\mathbf{A} + \alpha \mathbf{T})\right]_{\alpha=0} = \mathbf{T} = \mathbb{I} : \mathbf{T}$$

Therefore,

$$\frac{\partial \mathbf{A}}{\partial \mathbf{A}} = \mathbb{I}$$

Here $\mathbb{I}$ is the fourth order identity tensor. In index notation with respect to an orthonormal basis

$$\mathbb{I} = \delta_{ik}\delta_{jl}\ \mathbf{e}_i \otimes \mathbf{e}_j \otimes \mathbf{e}_k \otimes \mathbf{e}_l$$

This result implies that

$$\frac{\partial \mathbf{A}^T}{\partial \mathbf{A}} : \mathbf{T} = \mathbb{I}^T : \mathbf{T} = \mathbf{T}^T$$

where

$$\mathbb{I}^T = \delta_{jk}\delta_{il}\ \mathbf{e}_i \otimes \mathbf{e}_j \otimes \mathbf{e}_k \otimes \mathbf{e}_l$$

Therefore, if the tensor **A** is symmetric, then the derivative is also symmetric and we get

$$\frac{\partial \mathbf{A}}{\partial \mathbf{A}} = \mathbb{S} = \frac{1}{2}(\mathbb{I} + \mathbb{I}^T)$$

where the symmetric fourth order identity tensor is

$$\mathbb{S} = \frac{1}{2}(\delta_{ik}\delta_{jl} + \delta_{il}\delta_{jk})\ \mathbf{e}_i \otimes \mathbf{e}_j \otimes \mathbf{e}_k \otimes \mathbf{e}_l$$

C.2 Derivatives of the principal invariants of a tensor

The principal invariants of a second order tensor are

$$I_1(\mathbf{A}) = tr\mathbf{A} \tag{C.1}$$

$$I_2(\mathbf{A}) = \frac{1}{2}\left[(tr\mathbf{A})^2 - tr\mathbf{A}^2\right] \tag{C.2}$$

$$I_3(\mathbf{A}) = \det(\mathbf{A}) \tag{C.3}$$

The derivatives of these three invariants with respect to **A** are (index notation with respect to an orthonormal basis)

$$\frac{\partial I_1}{\partial \mathbf{A}} = \mathbf{I} \qquad \text{where} \quad \mathbf{I} = \delta_{ij}\mathbf{e}_i \otimes \mathbf{e}_j \tag{C.4}$$

$$\frac{\partial I_2}{\partial \mathbf{A}} = I_1\mathbf{I} - \mathbf{A}^T \tag{C.5}$$

$$\frac{\partial I_3}{\partial \mathbf{A}} = \det(\mathbf{A})[\mathbf{A}^{-1}]^T = I_2\mathbf{I} - \mathbf{A}^T(I_1\mathbf{I} - \mathbf{A}^T) = (\mathbf{A}^2 - I_1\mathbf{A} + I_2\mathbf{I})^T \tag{C.6}$$

C.3 Derivative of the determinant of a tensor

The derivative of the determinant of a second order tensor **A** is given by

$$\frac{\partial}{\partial \mathbf{A}} \det(\mathbf{A}) = \det(\mathbf{A})[\mathbf{A}^{-1}]^T$$

In an orthonormal basis the components of **A** can be written as a matrix **A**. In that case, the right hand side corresponds the cofactors of the matrix.

C.4 Derivative of J with respect to the deformation gradient

We often need to compute the derivative of $J = \det \mathbf{F}$ with respect the the deformation gradient **F**. From tensor calculus we have, for any second order tensor **A**

$$\frac{\partial}{\partial \mathbf{A}}(\det \mathbf{A}) = \det \mathbf{A}\ \mathbf{A}^{-T}$$

Therefore,

$$\frac{\partial J}{\partial \mathbf{F}} = J\ \mathbf{F}^{-T}$$

C.5 Derivative of J with respect to the right Cauchy-Green deformation tensor

The derivative of J with respect to the right Cauchy-Green deformation tensor (**C**) is also often encountered in continuum mechanics. To calculate the derivative of $J = \det \mathbf{F}$ with respect to **C**, we recall that (for any second order tensor **T**)

$$\frac{\partial \mathbf{C}}{\partial \mathbf{F}} : \mathbf{T} = \frac{\partial}{\partial \mathbf{F}}(\mathbf{F}^T \cdot \mathbf{F}) : \mathbf{T} = (\mathbb{I}^T : \mathbf{T}) \cdot \mathbf{F} + \mathbf{F}^T \cdot (\mathbb{I} : \mathbf{T}) = \mathbf{T}^T \cdot \mathbf{F} + \mathbf{F}^T \cdot \mathbf{T}$$

Also,

$$\frac{\partial J}{\partial \mathbf{F}} : \mathbf{T} = \frac{\partial J}{\partial \mathbf{C}} : (\frac{\partial \mathbf{C}}{\partial \mathbf{F}} : \mathbf{T}) = \frac{\partial J}{\partial \mathbf{C}} : (\mathbf{T}^T \cdot \mathbf{F} + \mathbf{F}^T \cdot \mathbf{T}) = \left[\mathbf{F} \cdot \frac{\partial J}{\partial \mathbf{C}}\right] : \mathbf{T} + \left[\mathbf{F} \cdot \left(\frac{\partial J}{\partial \mathbf{C}}\right)^T\right] : \mathbf{T}$$

From the symmetry of $\mathbf{C}$ we have

$$\frac{\partial J}{\partial \mathbf{C}} = \left(\frac{\partial J}{\partial \mathbf{C}}\right)^T$$

Therefore, involving the arbitrariness of $\mathbf{T}$, we have

$$\frac{\partial J}{\partial \mathbf{F}} = 2\ \mathbf{F} \cdot \frac{\partial J}{\partial \mathbf{C}}$$

Hence,

$$\frac{\partial J}{\partial \mathbf{C}} = \frac{1}{2}\ \mathbf{F}^{-1} \cdot \frac{\partial J}{\partial \mathbf{F}}\ .$$

Also recall that

$$\frac{\partial J}{\partial \mathbf{F}} = J\ \mathbf{F}^{-T}$$

Therefore,

$$\frac{\partial J}{\partial \mathbf{C}} = \frac{1}{2}\ J\ \mathbf{F}^{-1} \cdot \mathbf{F}^{-T} = \frac{J}{2}\ \mathbf{C}^{-1}$$

In index notation,

$$\frac{\partial J}{\partial C_{IJ}} = \frac{J}{2}\ C^{-1}_{IJ}$$

C.6 Derivative of the inverse of the right Cauchy-Green tensor

Another result that is often useful is that for the derivative of the inverse of the right Cauchy-Green tensor ($\mathbf{C}$). Recall that, for a second order tensor $\mathbf{A}$,

$$\frac{\partial \mathbf{A}^{-1}}{\partial \mathbf{A}} : \mathbf{T} = -\mathbf{A}^{-1} \cdot \mathbf{T} \cdot \mathbf{A}^{-1}$$

In index notation

$$\frac{\partial A^{-1}_{ij}}{\partial A_{kl}}\ T_{kl} = B_{ijkl}\ T_{kl} = -A^{-1}_{ik}\ T_{kl}\ A^{-1}_{lj}$$

or,

$$\frac{\partial A^{-1}_{ij}}{\partial A_{kl}} = B_{ijkl} = -A^{-1}_{ik}\ A^{-1}_{lj}$$

Using this formula and noting that since $\mathbf{C}$ is a symmetric second order tensor, the derivative of its inverse is a symmetric fourth order tensor we have

$$\frac{\partial C^{-1}_{IJ}}{\partial C_{KL}} = -\frac{1}{2}\ (C^{-1}_{IK}\ C^{-1}_{JL} + C^{-1}_{JK}\ C^{-1}_{IL})$$